

## Sequentially linear analysis for simulating brittle failure

van de Graaf, Anne

**DOI**

[10.4233/uuid:dd9ea945-136c-4b74-bae2-f1a8cf9a6ed9](https://doi.org/10.4233/uuid:dd9ea945-136c-4b74-bae2-f1a8cf9a6ed9)

**Publication date**

2017

**Document Version**

Final published version

**Citation (APA)**

van de Graaf, A. (2017). *Sequentially linear analysis for simulating brittle failure*. [Dissertation (TU Delft), Delft University of Technology]. <https://doi.org/10.4233/uuid:dd9ea945-136c-4b74-bae2-f1a8cf9a6ed9>

**Important note**

To cite this publication, please use the final published version (if applicable). Please check the document version above.

**Copyright**

Other than for strictly personal use, it is not permitted to download, forward or distribute the text or part of it, without the consent of the author(s) and/or copyright holder(s), unless the work is under an open content license such as Creative Commons.

**Takedown policy**

Please contact us and provide details if you believe this document breaches copyrights. We will remove access to the work immediately and investigate your claim.

# **Sequentially linear analysis for simulating brittle failure**



# Sequentially linear analysis for simulating brittle failure

Proefschrift

ter verkrijging van de graad doctor  
aan de Technische Universiteit Delft,  
op gezag van de Rector Magnificus prof. ir. K.C.A.M. Luyben;  
voorzitter van het College voor Promoties,  
in het openbaar te verdedigen op  
dinsdag 2 mei 2017 om 10.00 uur

door

Anne Vincent VAN DE GRAAF  
civiel ingenieur  
geboren te Spijkenisse



Dit proefschrift is goedgekeurd door de promotoren:

Prof. dr. ir. J.G. Rots  
Prof. dr. ir. M.A.N. Hendriks

Samenstelling promotiecommissie bestaat uit:

Rector magnificus,	voorzitter
Prof. dr. ir. J.G. Rots	promotor
Prof. dr. ir. M.A.N. Hendriks	promotor

onafhankelijke leden:

Prof. dr. ir. L.J. Sluys	Technische Universiteit Delft
Prof. dr. ir. J.C. Walraven	Technische Universiteit Delft ( <i>emeritus</i> )
Prof. dr. ir. A.H. van den Boogaard	Universiteit Twente
Dr. J. Alfaiate	Instituto Superior Técnico
Dr. M.J. DeJong	University of Cambridge
Prof. dr. ir. H.E.J.G. Schlangen	Technische Universiteit Delft, reservelid

The financial support by Delft Cluster and the Centre for Underground Construction (COB) is gratefully acknowledged.

Copyright © 2017 by A.V. van de Graaf

All rights reserved. No part of the material protected by this copyright notice may be reproduced or utilized in any form or by any means, electronic or mechanical, including photocopying, recording or by any information storage and retrieval system, without the prior permission of the author.

ISBN 978-94-6186-799-5

Cover design by: Evelien Jagtman - <http://evelienjagtman.com>

Printed by: Gildeprint - <https://www.gildeprint.nl>

An electronic version of this thesis is available at <http://repository.tudelft.nl>

# Summary

The numerical simulation of brittle failure at structural level with nonlinear finite element analysis (NLFEA) remains a challenge due to robustness issues. We attribute these problems to the dimensions of real-world structures combined with softening behavior and negative tangent stiffness at local level which may lead to non-convergence, i.e. the applied external loads are not in equilibrium with the internal forces. Also multiple cracks that compete to “survive” and the possibility of bifurcations, i.e. the existence of multiple equilibrium paths, contribute to these problems. However, in engineering practice robust numerical methods become increasingly important. For example, NLFEA may be used to determine the actual load bearing capacity of existing concrete bridges in order to assess whether these meet the current regulations. Also for the prediction of building damage due to underground construction or seismic action NLFEA may be employed.

To address the numerical robustness issues, sequentially linear analysis (SLA) was developed which exploits the fact that a linear analysis is inherently stable. By assuming a stepwise material degradation (frequently referred to as a saw-tooth law which corresponds to a series of damage increments) the nonlinear response of the structure can be approximated by a series of linear analyses. Although the effectiveness of this approach was demonstrated for several case studies, a number of limitations had to be overcome to broaden its application area.

The aim of the present work is to extend the original SLA proposal such that it can be used to model failure of quasi-brittle structures in a robust and objective way. To this end, we have developed the following three contributions:

1. An improved concept to set up saw-tooth softening laws that meet two requirements. The first one demands that the area enclosed by the saw-tooth law (a measure for the energy dissipation upon fracture) equals the area enclosed by the base material law. The second requirement is invariance with respect to the ultimate crack width or crack strain. In addition, saw-tooth models for bond–slip relations and for stress–total strain laws that exhibit a linear snap-back at constitutive level have been developed.
2. An approach to include Coulomb friction in our numerical simulations. Contrary to conventional saw-tooth laws which are determined *a priori*, the instantaneous stiffness changes as a result of progressive damage is determined while the analysis advances. This has been worked out for two models. The first one is based on an uncoupled formulation (i.e. excluding dilatancy) and

the damage increments are determined by taking a specified relative sliding displacement increment into account. The second model uses a coupled formulation (i.e. dilatancy is included), but it does not include cohesion softening. In essence, it determines the next secant stiffness from the actual tangent stiffness and two specified relative displacement increments.

3. A novel strategy for non-proportional loading based on a constrained optimization. For each integration point one or more constraints are formulated in terms of a load multiplier to enforce a stress state that obeys the material law. This enables us to identify load multiplier sets that result in constitutively admissible stresses. Subsequently, the load multiplier is maximized by considering the load multiplier sets of all integration points simultaneously. At times conflicting load multiplier sets may be obtained in which case the last “successful” load combination was scaled in a proportional way.

Through extensive examination of two case studies, we have validated the effectiveness of the developed concepts and strategies. The first case study concerned a masonry shear wall that features a discrete crack model combined with an uncoupled Coulomb friction model for all mortar joints and that is loaded in a non-proportional way. The obtained SLA results resemble the experimentally observed failure mechanism and the predicted ultimate load agrees to the experimental value. The second case study involved a 1/10<sup>th</sup> scaled masonry façade subjected to deadweight and non-uniform tunneling-induced settlements. The obtained crack pattern is in agreement with experimental observations. However, since the current SLA implementation does not include a proper crack closure algorithm the simulation had to be aborted prematurely due to load reversal at one of the cracks. Both case studies underlined the robustness of the SLA approach and the effectiveness of the developed non-proportional loading strategy.

We have also carried out verification and objectivity studies for the proposed saw-tooth models. For the discrete and smeared crack models the improved concept to set up saw-tooth laws was shown to be virtually objective with respect to mesh refinement and damage increment refinement. The analyses that combined the smeared crack model with bond–slip behavior demonstrated that SLA does not require any measures (e.g. local imperfections) to achieve strain localization. Moreover, the SLA-based analyses automatically captured structural snap-backs without requiring special techniques like arc-length control. In addition, the scaling procedure does not suffer from bifurcations.

As a result of the performed numerical analyses we suggest the following topics to be addressed by future research:

- Extend SLA such that it can account for compressive failure. It is expected that this can be done in a similar way as for tensile failure.
- Include a strategy for stress reversal. The point here is that the current approach transfers damage due to tensile failure one-to-one to the compressive regime. As a consequence, improper crack closure behavior has been

observed. We suggest to develop an approach that in case of an imminent stress reversal first returns the stress to the origin and subsequently adapts the material properties.

- Improve the performance by employing (iterative) solvers that can reuse the previous solution in a smart way. Keep in mind that per analysis step only a few entries of the system stiffness matrix are updated. Another way to reduce computer time would be to apply multiple damage increments per analysis step.



# Samenvatting

De numerieke simulatie van brossen breuk op constructieniveau met niet-lineaire eindige elementenanalyses blijft een uitdaging door problemen met de robuustheid van de berekening. We wijten deze problemen aan de combinatie van de afmetingen van werkelijke constructies en het brossen materiaalgedrag dat op puntniveau gedefinieerd is, wat kan leiden tot het niet-convergeren van de analyse. Dat wil zeggen dat de aanwezige externe belasting op dat moment niet in evenwicht is met de inwendige krachten. Deze problemen worden versterkt doordat verschillende scheuren ten koste van elkaar proberen door te groeien en door het ontstaan van vertakkingen in het evenwichtspad wat betekent dat er meerdere evenwichtstoestanden mogelijk zijn. Echter, voor praktische toepassingen worden robuustere numerieke simulatiemethoden steeds belangrijker. Denk hierbij bijvoorbeeld aan het bepalen van het werkelijke draagvermogen van bestaande betonnen bruggen en viaducten om vast te stellen of deze aan vervanging toe zijn. Ook bij het voorspellen van gebouwschade als gevolg van ondergronds bouwen of aardbevingen worden niet-lineaire eindige elementenanalyses ingezet.

Om de convergentieproblemen het hoofd te bieden werd sequentieel lineaire analyse (SLA) ontwikkeld dat gebruik maakt van het feit dat een lineaire analyse numeriek stabiel is. Door het aannemen van een stapsgewijze degradatie van het materiaal, de zogenaamde zaagtandrelatie, zijn we in staat het niet-lineaire gedrag van de constructie te benaderen. Hoewel de effectiviteit van deze aanpak voor verschillende case studies was aangetoond, moesten er nog een aantal beperkingen overwonnen worden om SLA breder toepasbaar te maken.

Het doel van dit werk is om SLA zodanig uit te breiden dat het gebruikt kan worden om het brossen bezwijkgedrag van constructies op een robuuste en objectieve manier te kunnen simuleren. Om dit doel te bereiken hebben we op een drietal punten een bijdrage geleverd aan de bestaande SLA aanpak:

1. Een verbeterde manier om zaagtandrelaties te definiëren die voldoen aan de volgende twee eisen. Ten eerste moet het door de zaagtandrelatie omsloten oppervlak (een maat voor de energiedissipatie als gevolg van het ontstaan van een breuk) gelijk zijn aan het oppervlak omsloten door de oorspronkelijke constitutieve relatie. De tweede eis is dat de uiterste scheurwijdte of scheurrek onafhankelijk moet zijn van de gekozen discretisaties. Daarnaast hebben we zaagtandrelaties ontwikkeld voor aanhechting–sliprelaties en spanning–totale rekrelaties met een lineaire *snap-back* op materiaalniveau.

2. Een manier om Coulombse wrijving mee te kunnen nemen in onze numerieke simulaties. Anders dan bij traditionele zaagtandrelaties—die vooraf bepaald worden—worden hier de instantane stijfheidsveranderingen gaandeweg bepaald. Dat hebben we voor twee modellen uitgewerkt. De eerste is gebaseerd op een ongekoppelde formulering (d.w.z. dilatantie wordt niet meegenomen), waarbij de schadeincrementen bepaald worden door een verondersteld increment in de afschuifvervorming. Het tweede model maakt gebruik van een gekoppelde formulering (d.w.z. dilatantie wordt wel meegenomen), maar cohesiesoftening blijft hierbij buiten beschouwing. De gereduceerde stijfheden worden bij dit model bepaald uit de huidige tangentstijfheid en twee veronderstelde incrementen in de relatieve verplaatsingen.
3. Een nieuwe strategie voor niet-proportionele belastingen die gebaseerd is op *constrained optimization*. Hierbij is het uitgangspunt dat we voor elk integratiepunt één of meerdere ongelijkheden opstellen in termen van een schaalfactor om een constitutief toelaatbare spanningstoestand af te dwingen. Dit stelt ons in staat om verzamelingen van schaalfactoren te bepalen die resulteren in spanningen die daadwerkelijk kunnen optreden. Vervolgens maximaliseren we de schaalfactor door de verzamelingen van alle integratiepunten gelijktijdig te beschouwen. Het kan voorkomen dat er conflicterende verzamelingen worden gevonden. In dat geval schalen we de laatste “succesvolle” belastingcombinatie op een proportionele manier.

Door middel van twee case studies hebben we op een integrale manier de effectiviteit van de ontwikkelde methodes en strategieën gevalideerd. De eerste case study betrof de analyse van een op afschuiving belaste metselwerkwand waarbij alle mortelvoegen op zowel trek als afschuiving konden bezwijken. Daarnaast hadden we te maken met niet-proportionele belasting. We hebben aangetoond dat we in staat zijn om het experimenteel waargenomen gedrag, in termen van de maximale belasting en het optredende bezwijkmechanisme, goed te voorspellen. In de tweede case study hebben we het gedrag onderzocht van een schaalmodel van een metselwerkgevel die onderworpen werd aan ongelijkmatige zettingen als gevolg van de bouw van een tunnel. Daaruit is gebleken dat we in staat zijn om de experimenteel waargenomen scheurpatronen te reproduceren. Echter, omdat de gebruikte SLA implementatie het gedrag van gesloten scheuren niet goed modelleert waren we genooddaakt de berekening voortijdig te beëindigen, vanwege een gesloten scheur die onder druk kwam te staan. Beide case studies onderstreepten dat de SLA aanpak robuust is en dat de ontwikkelde strategie voor niet-proportionele belasting effectief is.

Verder hebben we de voorgestelde zaagtandmodellen geverifieerd en de objectiviteit van deze modellen onderzocht. Voor discrete en uitgesmeerde scheurmodellen hebben we vastgesteld dat de voorgestelde verbeteringen leiden tot zaagtandrelaties die nagenoeg objectief zijn ten aanzien van mesh- en zaagtandverfijningen. De analyses die het uitgesmeerde scheurmodel combineerden met aanhecht-slipgedrag lieten zien dat SLA geen maatregelen vereist—zoals het aanbrenge-

van lokale imperfecties—om scheuren te laten lokaliseren. Bovendien hebben we aangetoond dat SLA geen speciale technieken—zoals booglengtemethodes—nodig heeft om *snap-backs* op constructieniveau te reproduceren. Verder is de schalingsprocedure niet gevoelig gebleken voor vertakkingen in het evenwichtspad.

Voortvloeiend uit de resultaten van onze numerieke analyses stellen we voor om de volgende punten bij toekomstig onderzoek nader te beschouwen:

- Breid SLA uit zodat bezwijken onder druk kan worden meegenomen. We verwachten dat dit op een vergelijkbare manier kan worden gedaan als voor bezwijken onder trek.
- Ontwikkel een strategie om spanningswisselingen mee te kunnen nemen. Het punt is dat met de huidige aanpak de schade die ontstaan is door bezwijken onder trek één-op-één wordt overgenomen voor de bepaling van het gedrag onder druk, met als gevolg een onjuiste modellering van gesloten scheuren. Wij stellen voor om een aanpak te ontwikkelen waarbij de spanning bij een op handen zijnde spanningswisseling eerst terugkeert naar de oorsprong om vervolgens de materiaaleigenschappen aan te passen.
- Verkort de benodigde rekentijd door het toepassen van (iteratieve) *solvers* die de oplossing van de vorige stap op een slimme manier kunnen hergebruiken. Bedenk hierbij dat tussen twee opeenvolgende stappen er slechts enkele elementen van de systeemstijfheidsmatrix veranderen. Een andere manier om de rekentijd te beperken zou zijn door meerdere schadeincrementen per stap toe te passen.





# Notation

Throughout the present work we will use generally accepted symbols to denote quantities. Although all symbols will be explained in the running text, the following list of symbols serves as a reference. Some symbols are accompanied by one or more indices. Superscript indices that should not be interpreted as “raise to the power” are enclosed in parenthesis. In general, we use subscript  $i$  to denote the integration point index, superscript  $j$  for the analysis step number, and subscript  $k$  for the saw-tooth index. Normal components of an entity have the subscript  $n$  whereas tangential components are labeled with the subscript  $t$ . Subscripts that represent abbreviations of actual words have been typeset using an upright font, e.g.  $t$  in  $f_t$  stands for “tensile”. Another convention that we have adopted here is to write vectors and matrices in bold.

## Roman symbols

Symbol	Description
$A$	(Element) area.
$c, c_0$	Actual and initial cohesion.
$c_1, c_2$	Coefficients.
$\mathbf{D}_{\text{sec}}$	Secant stiffness matrix
$\mathbf{D}_{\text{tan}}$	Consistent tangent stiffness matrix.
$d$	Isotropic damage parameter.
$d_n, d_t$	Orthotropic damage parameters in $n$ and $t$ directions.
$E, E_0$	Actual and initial isotropic Young’s moduli.
$E_n, E_t$	Orthotropic Young’s moduli in $n$ and $t$ directions.
$E_{\text{min}}$	Minimum Young’s modulus.
$F$	Force.
$f$	Material strength.
$f_t, f_{t,0}$	Actual and initial uniaxial tensile strength.
$f_y$	Yield stress.
$G, G_0$	Actual and initial isotropic shear stiffness.
$G_f^I, G_f^{II}$	Fracture energy corresponding to modes I and II.
$h$	Crack band width.
$k_n, k_{n,0}$	Actual and initial interface normal stiffness.

Symbol	Description
$k_t, k_{t,0}$	Actual and initial interface shear stiffness.
$\ell$	Characteristic (element) length.
$N$	Number of saw-teeth
$p, p_1, p_2$	Ripple band width parameters
$s$	Crack sliding displacement.
$t_n, t_t$	Interface normal and shear tractions.
$t_{t,u}$	Ultimate interface shear traction.
$u$	Displacement.
$\Delta u_n, \Delta u_t$	Relative displacements in $n$ and $t$ directions.
$\Delta u_n^{\text{pl}}, \Delta u_t^{\text{pl}}$	Plastic relative normal and shear displacements.
$w, w_u$	Actual and ultimate crack widths.

## Greek symbols

Symbol	Description
$\beta$	Shear retention factor.
$\varepsilon$	Total strain.
$\varepsilon_{xx}, \varepsilon_{yy}, \varepsilon_{nn}, \varepsilon_{tt}$	Normal strain components in $x, y, n,$ and $t$ directions.
$\varepsilon^{\text{cr}}, \varepsilon_u^{\text{cr}}$	Actual and ultimate crack extensional strains.
$\varepsilon^{\text{el}}$	Elastic extensional strain.
$\varepsilon_p$	Total strain at peak stress.
$\gamma_{xy}, \gamma_{nt}$	Shear strain components.
$\gamma^{\text{cr}}$	Crack shear strain.
$\kappa$	Plasticity parameter.
$\lambda_{\text{crit}}$	Critical load multiplier.
$\sigma$	Total stress.
$\sigma_{xx}, \sigma_{yy}, \sigma_{nn}, \sigma_{tt}$	Normal stress components in $x, y, n,$ and $t$ directions.
$\sigma_{xy}$	Shear stress components.
$\sigma_1, \sigma_2$	Maximum and minimum principal stresses.
$\sigma_{\text{gov}}$	Governing stress component.
$\phi$	Friction angle.
$\psi$	Dilatancy angle.
$\nu_0$	Initial isotropic Poisson's ratio.
$\nu_{nt}, \nu_{tn}$	Orthotropic Poisson's ratios.
$\nu_{\text{min}}$	Minimum Poisson's ratio.

# Contents

<b>Summary</b>	<b>v</b>
<b>Samenvatting</b>	<b>ix</b>
<b>Notation</b>	<b>xiii</b>
<b>1 Introduction</b>	<b>1</b>
1.1 Background and motivation . . . . .	1
1.2 Research question and scope . . . . .	6
1.3 Outline . . . . .	7
<b>2 Background theory</b>	<b>11</b>
2.1 Nonlinear constitutive models in finite element analysis . . . . .	11
2.2 Towards a non-iterative approach . . . . .	23
2.3 Introduction to stepwise secant material laws . . . . .	25
2.4 Event-by-event strategy . . . . .	27
2.5 Limitations . . . . .	31
2.6 Summary . . . . .	32
<b>3 Stepwise secant material laws</b>	<b>33</b>
3.1 Literature review and discussion . . . . .	33
3.2 Improved band width ripple concept . . . . .	40
3.3 Snap-back at constitutive level . . . . .	43
3.4 Conclusions . . . . .	47
<b>4 Stepwise secant Coulomb friction laws</b>	<b>49</b>
4.1 Critical load multiplier . . . . .	49
4.2 An uncoupled formulation . . . . .	50
4.3 A coupled formulation . . . . .	53
4.4 Tension–shear failure criterion . . . . .	58
4.5 Conclusions . . . . .	59

<b>5</b>	<b>Non-proportional loading strategies</b>	<b>61</b>
5.1	Introduction . . . . .	61
5.2	Literature review and discussion . . . . .	62
5.3	Constrained maximization analogy . . . . .	67
5.4	Double load multiplier strategies . . . . .	71
5.5	Conclusions . . . . .	73
<b>6</b>	<b>Verification and objectivity studies</b>	<b>75</b>
6.1	Notched beam specimen with discrete cracking . . . . .	75
6.2	Notched beam specimen with smeared cracking . . . . .	85
6.3	Tension–pull specimen with smeared cracking and bond–slip . . . . .	96
6.4	Masonry specimen with Coulomb friction and non-proportional loading . . . . .	102
6.5	Conclusions . . . . .	110
<b>7</b>	<b>Validation and application</b>	<b>113</b>
7.1	Pre-compressed masonry shear wall . . . . .	113
7.2	Scaled masonry façade . . . . .	121
7.3	Reinforced glass beam and RC slab . . . . .	131
7.4	Conclusions . . . . .	133
<b>8</b>	<b>Discussion and conclusions</b>	<b>137</b>
8.1	New developments . . . . .	137
8.2	Conclusions . . . . .	138
8.3	Recommendations . . . . .	140
<b>A</b>	<b>Series development for Coulomb friction</b>	<b>143</b>
	<b>References</b>	<b>145</b>
	<b>Acknowledgements</b>	<b>151</b>
	<b>Curriculum Vitae</b>	<b>153</b>
	<b>List of publications</b>	<b>155</b>

# Chapter 1 Introduction

## 1.1 Background and motivation

Differential settlements of the soil in urban areas due to underground construction may result in severe building damage. When buildings are unable to follow tunneling-induced soil deformations this may result in aesthetic and structural damage. Particularly in case of soft soil conditions and unreinforced masonry structures, this poses a serious threat. In the past years, building damage due to underground construction has received a lot of attention in Dutch cities like Amsterdam and Delft where railway tunnels are constructed under their historical centers. Not only local residents but for instance also insurance companies would like to have a clear idea of the risks involved and what damage might be expected. Figure 1.1a shows an example of a masonry façade that has been investigated numerically [22]. For the structural analysis, a computational model of the façade was subjected to an anticipated settlement scenario. The crack pattern computed with the nonlinear finite element method (Figure 1.1b) gives an impression of the damage to be expected.

To assess the risk of building damage due to underground construction, reliable numerical predictions are important. These numerical predictions are not only used to inform the parties involved but also to design mitigating measures in case of severe or even unacceptable damage. In this way, inconvenience may be limited or even avoided and money may be saved.

However, the numerical prediction of building damage is a challenging task for at least two reasons. In the first place, the historical buildings under consideration are made of unreinforced masonry which behaves in a rather brittle manner. This means that cracks may arise suddenly and they may propagate and grow wider rapidly. We have found that it is rather difficult to reproduce this kind of brittle behavior with existing numerical models. Secondly, the size of buildings is several orders of magnitude larger than the scale of usual fracture mechanics tests in laboratories. This implies that the ratio between the stored elastic energy and the energy that is dissipated upon fracture of the material is relatively large. The up-scaling to large structural dimensions involves sudden brittleness and jumps in the load–displacement response and may have a negative impact on the robustness of the numerical analysis.

Another example where numerical modeling of brittle fracture plays an impor-

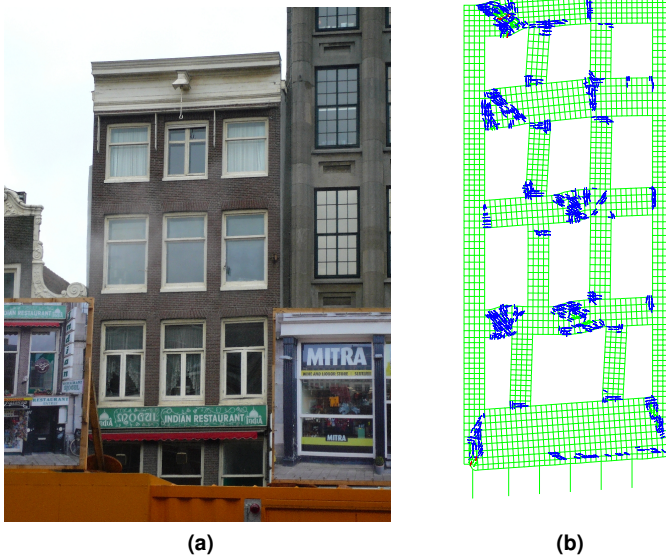


**Figure 1.1** (a) Masonry building in the vicinity of a building pit. (b) Numerically predicted deformation and crack pattern of the façade subjected to a settlement scenario obtained with a 2D simulation [22].

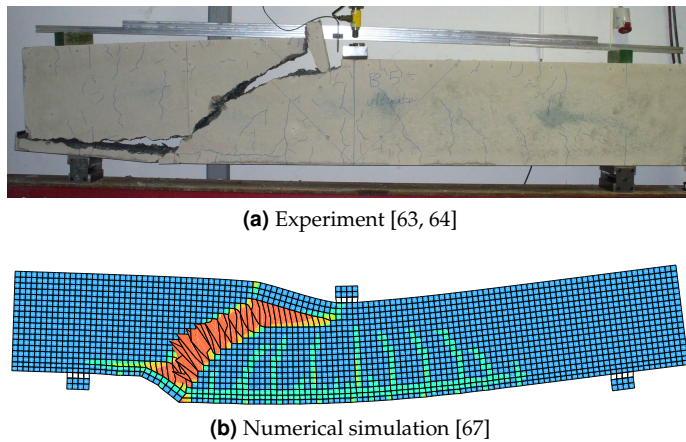


**Figure 1.2** Failure of a shear-critical RC beam.

tant role is the reevaluation of existing concrete structures. Many concrete bridges and viaducts in the Netherlands built before 1975 may not comply with the current standards due to heavier vehicles and stricter requirements [1, 73]. During the design of these structures the large increase in traffic as well as the maximum load per wheel was not foreseen. Furthermore, over the past decades research has shown that the design rules used in those days were not always on the conservative (safe) side, especially regarding shear failure. Consequently, the current standards are stricter than those used during the design. Figure 1.2 shows a shear-critical reinforced concrete (RC) beam which may represent a part of a concrete bridge that was studied in order to determine its actual load-bearing capacity.

Whenever an existing structure does not comply with the current design codes there are basically three options. These are:

1. Replace the existing structure.
2. Strengthen the existing structure.
3. Perform a more refined assessment of the structure, exploiting any “hidden reserves”.

For the first two options not only the costs of the construction work itself have to be taken into account but also any additional costs, such as economic losses due to traffic diversions and congestions, need to be considered. Therefore, the first two options are relatively expensive and they should be selected with care. However, if a quick assessment shows that the structure is close to being qualified as safe then the third option may pay off well, as exemplified by the brief *Delft Integraal* article in Figure 1.3. Optionally, material testing supports the refined assessment, by taking into account the actual mechanical properties. In that way, it can be shown





Goed nieuws voor de schatkist: bruggen en andere civieltechnische constructies hebben een verborgen capaciteit. Ze kunnen de toegenomen verkeersbelasting beter dragen en hoeven daardoor minder snel te worden vervangen of versterkt. Die conclusie trekt prof.dr.ir. Joost Walraven, hoogleraar betonconstructies bij CiTG. Met zijn medewerkers combineerde hij proeven met geavanceerde mechanica-analyses. De bevinding van Walraven betekent een meevaller van rond de 300 miljoen euro in de komende vijf jaar.

**Figure 1.3** According to this *Delft Integraal* article (2011, nr. 1, in Dutch), research has shown that bridges possess “hidden load-carrying reserves” which means that fewer structures need replacement or strengthening in the near future. As a result, approximately 300 million euro is saved in the next five years.

that the material strength is more than what was assumed during the design stage. The basis of the assessment procedures are usually twofold: laboratory tests on freshly cast specimens or samples taken from existing structures, and more advanced structural analysis, for example by performing a nonlinear finite element analysis (NLFEA). In case the refined analysis is carried out numerically, robustness of the adopted method is of crucial importance since methods that are not robust may produce unreliable results.

Besides assessment studies as illustrated by the previous building and bridge examples, robust NLFEA is also required for other fields of structural mechanics. A recent example in the Netherlands is the seismic analysis of buildings in the Groningen area. Also research on how to improve existing standards or to provide a basis for new regulations makes use of NLFEA. For ‘forensic’ analysis—to reconstruct the collapse of a structure—or performance-based design a robust NLFEA tool is indispensable.

As stated, for all mentioned application areas robustness of the adopted nu-

merical technique is an important aspect. Robustness issues may arise when masonry and/or concrete structures are analyzed with NLFEA software. To get a better understanding of these problems we first explore how a typical NLFEA tool works. Most computer codes apply the total load in a finite number of steps, i.e. by increasing the applied load stepwise. After each so-called load increment, the program tries to re-establish global equilibrium, since the increased external loads are no longer balanced by the internal forces. Through an iterative procedure it attempts to predict the additional deformations due to the applied load increment. Since the internal forces are determined by the deformations and the material behavior, they change from one iteration to the next. If all goes well, the unbalance between external loads and internal forces diminishes throughout the iterative procedure. A solution is said to be converged as soon as the unbalance has become sufficiently small. The outlined solution procedure generally works quite well as long as no strong variations in deformations occur within a load increment. However, brittle fracture, which characterizes concrete and masonry structures, may arise suddenly and then propagate rapidly. The use of smaller load increments or so-called arc-length stabilization procedures may sometimes remedy these problems, although no universal solution exists. The difficulty that the program faces, is that it has to decide where new cracks will arise and which existing ones will propagate or close. Especially when multiple cracks are developing simultaneously, this task may become quite difficult. Consequently, the iterative procedure may not be able to find a converged solution. That is, the unbalance between external loads and internal forces is greater than what is considered to be acceptable. Hence, when a numerical simulation fails to converge after some load increment, it is difficult to judge the value and reliability of the considered analysis step. The same holds for subsequent analysis steps that did not start from an equilibrium state.

The discussed non-convergence issues are affected by several aspects. Apart from large structural dimensions combined with brittle material behavior, non-convergence may also be caused by multiple cracks competing to “survive” and/or bifurcations [60]. With bifurcations we mean that more than one equilibrium state may be possible.

The outlined problems are not limited to concrete and masonry structures, but more generally apply to structures made of quasi-brittle materials. These are materials that seem to behave perfectly brittle, i.e. all load-carrying capacity is lost after attaining the tensile strength, yet they do possess some post-peak capacity due to material softening. From the viewpoint of a material model, it means that the stress which is transmitted across the crack gradually decreases upon increasing crack width. As soon as a certain crack width is exceeded, the material has fully softened and a stress-free crack remains. Other examples of quasi-brittle materials include glass and rock.

To address the problems presented here, Rots [57] proposed a robust finite element analysis (FEA) technique, called SLA, to simulate nonlinear structural behavior. The starting point of this technique is to assume that the material degrades

in a stepwise fashion, i.e. stiffness and strength properties are reduced in a discretized instead of a continuous way. We will call such a discrete reduction in mechanical properties a damage increment. By applying only one damage increment per analysis step at only one point of the computational model, the simulation is damage-controlled. Thus, a major difference with common analysis procedures is that instead of considering a load, displacement or arc-length increment, a damage increment is taken. To locate the next point in the model where the material degrades, a selection procedure is adopted that takes into account the actual strength distribution and the stress field based on a linear analysis. The load that leads to progressive damage is recomputed by scaling the linear analysis results such that at one point the strength limit is attained. Hence, tracing the structural behavior involves a series of scaled linear analyses and subsequently applied damage increments. The use of scaled linear analyses ensures global equilibrium in each analysis step. The primary advantage of the SLA approach is that it does not require an iterative procedure to establish global equilibrium, making it inherently stable.

However, for SLA to cover a wider range of applications, a number of limitations had to be overcome. For instance, the original concept was used for materials that can be described by uniaxial stress–strain relations, neglecting any biaxial effects. Also, its application was limited to proportional loading. This means for instance that the combined action of self-weight and live loads cannot be taken into account. Consequently, there was a need to extend the SLA method such that these relevant aspects could be included.

## 1.2 Research question and scope

The main question that is addressed in this thesis is as follows:

*How can sequentially linear analysis (SLA) be extended such that it can be used to model failure of quasi-brittle structures in a robust and objective way?*

In this thesis, the words ‘robust’ and ‘objective’ are understood to mean the following. A finite element analysis technique is said to be robust if it does not suffer from convergence problems. In other words, for every step in the numerical analysis the equilibrium conditions should be met. A finite element analysis technique is understood to be objective if its results are insensitive with respect to the chosen mesh layout and the adopted damage increment size.

To answer the main question we will address the following sub questions:

- How can SLA be extended to make a wider range of material models available, including smeared and discrete crack models, bond–slip models and frictional models?
- Which strategies are available to deal with non-proportional loading for SLA? Which difficulties may arise and how to deal with them?

- Show that the developed extensions lead to objective results in terms of mesh refinement and damage increment refinement?

The originality of this work lies in the critical evaluation of SLA, improvements of the original formulation and broadening its application field. Original improvements include enhanced and new secant models to approximate nonlinear material laws for discrete and smeared cracking, and bond–slip models. We also explore a novel strategy for non-proportional loading. The application field of SLA is broadened by the development of two approximations of the Coulomb friction model.

The work presented here is aimed at quasi-static loading and applied to two-dimensional models only. Quasi-static loading means that we assume that at any moment of the simulation a static equilibrium exists between the internal forces and external loads. In other words, we assume the inertia term in the equation of motion to be much smaller than the stiffness term, which effectively results in static equilibrium. Since it is logical to first demonstrate the effectiveness of the new developments for models that are well understood, the case studies in this work are two-dimensional only. At the end of this thesis we will show that this does not mean that the use of SLA is limited to two-dimensional models.

## 1.3 Outline

Figure 1.4 illustrates the outline of the thesis which follows the trivial yet logical order of introduction, new developments, verification and validation, and discussion and conclusions. The remainder of this section gives more information on the contents of each chapter.

Chapter 2 revisits the nonlinear constitutive models that are adopted throughout this thesis and it describes the fundamental concepts of SLA. It explains why SLA was developed in the first place and which concepts and techniques inspired its development. Subsequently, we introduce the fundamental assumption of approximating nonlinear constitutive relations by stepwise secant material laws. Then we will stipulate how these stepwise secant material laws can be employed in an event-by-event strategy to obtain the global behavior of the structure. The chapter ends by listing the limitations of the original SLA work that are addressed in the present work.

The next two chapters elaborate on how to set up stepwise secant material laws. A distinction is made between materials that are based on uniaxial stress–strain relations and the Coulomb friction model. Regarding the former, Chapter 3 reviews and discusses models from literature to set up stepwise secant approximations. Here we also present an improved generic concept and a model that can handle a linear snap-back at constitutive level. Chapter 4 deals with the Coulomb friction model and it presents two secant formulations that are tailored for the SLA scheme: an uncoupled and a coupled one.

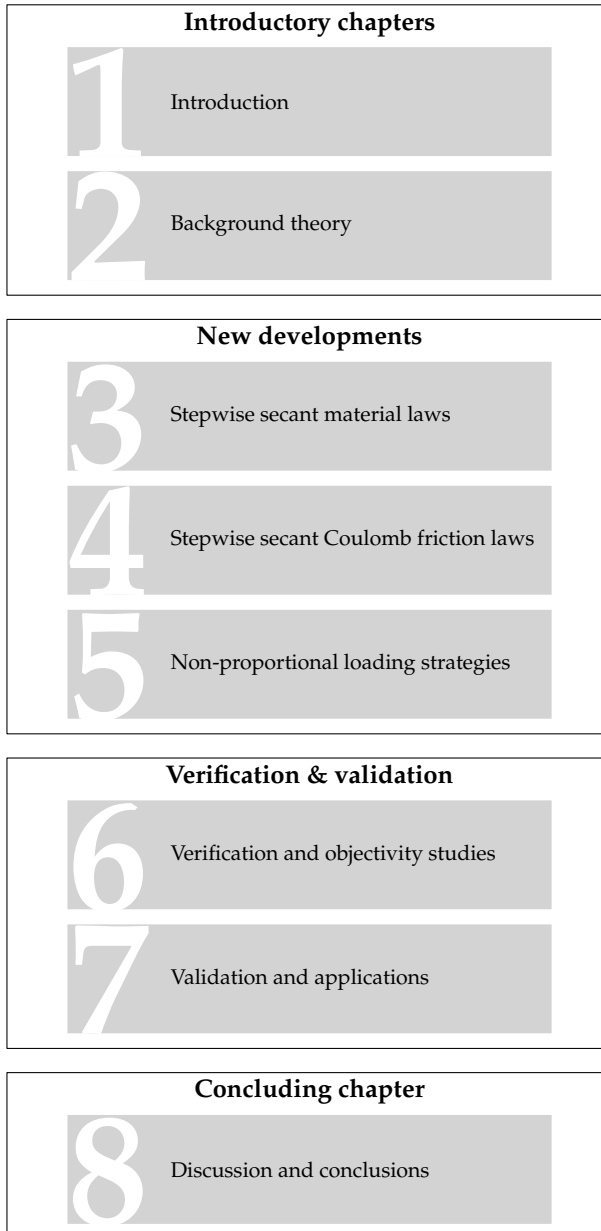


**Figure 1.4** Thesis outline.

Chapter 5 addresses the issue of non-proportional loading. The chapter starts by reviewing and discussing methods from literature. Subsequently, we propose a novel strategy based on constrained optimization.

Next, we validate the new developments to ensure that robust results are obtained. First, the objectivity of the stepwise secant material laws is verified through numerical analyses of several case studies (Chapter 6). Here, we show the effect of mesh refinement as well as the effect of the adopted stepwise secant approximation (damage increment refinement) on the results. In Chapter 7 we use the new extensions to analyze a masonry shear wall and a scaled masonry façade and we compare the obtained numerical results with available experimental data.

Finally, Chapter 8 discusses the results of the present work in an integral way and conclusions are drawn. Here we will also indicate which topics need to be addressed by future research.



## Chapter 2 Background theory

The previous chapter stated the objective of this thesis as extending sequentially linear analysis (SLA) such that it can be used to model quasi-brittle failure in a robust and objective way.

The present chapter consists of two parts. The first part (Section 2.1) introduces five material models from literature that will be used throughout this work. The second part of the chapter, which has been split up in four sections, reviews and discusses the basic concepts of SLA. First, Section 2.2 presents the motivation and inspiration for the development of SLA. Subsequently, Section 2.3 introduces the stepwise secant material law, in the literature also referred to as saw-tooth law, which is fundamental to SLA. Then, Section 2.4 explains how these stepwise secant material laws can be employed in an event-by-event strategy to capture the global nonlinear response of the finite element model. It also lists a few other similar approaches. Finally, Section 2.5 lists three major limitations of the original SLA proposal.

Each of the next three chapters addresses one of the limitations presented in the final section.

### 2.1 Nonlinear constitutive models in finite element analysis

The present section revisits five nonlinear constitutive models from literature that are used throughout this thesis. The models that will be presented include discrete and smeared crack models, a bond-slip model, a Coulomb friction model and finally a uniaxial elastic-perfectly plastic model. For all material models presented here, we assume secant unloading. This section is meant to serve as a reference for further discussion in later sections and chapters.

#### 2.1.1 Discrete crack model

The local deformation within discrete cracks which characterizes fracture of quasi-brittle materials inspired researchers (e.g. Ngo and Scordelis [52], Hillerborg [36], Ingraffea and Saouma [38]) to develop the discrete crack model. The key idea of the model is to mimic the arising geometrical discontinuities (cracks) by including interface elements in the finite element discretization. To preserve mesh topology,



we insert these elements *a priori* in the mesh at locations where we expect cracks to arise. Note that the alignment of the interface elements implicitly defines the crack direction. In the present work, we limit the use of the discrete crack approach to two-dimensional models.

For the elastic stage we assume the interface normal traction  $t_n$  and shear traction  $t_t$  to depend on the relative normal displacement  $\Delta u_n$  and relative shear displacement  $\Delta u_t$  as follows

$$\begin{bmatrix} t_n \\ t_t \end{bmatrix} = \begin{bmatrix} k_{n,0} & 0 \\ 0 & k_{t,0} \end{bmatrix} \begin{bmatrix} \Delta u_n \\ \Delta u_t \end{bmatrix} \quad (2.1)$$

with  $k_{n,0}$  and  $k_{t,0}$  the initial normal and shear stiffness, respectively. Throughout this work the indices  $n$  and  $t$  denote the normal and tangential direction with respect to the crack face. To suppress spurious displacements in the uncracked stage, we assign relatively high dummy values to  $k_{n,0}$  and  $k_{t,0}$ . As a rule of thumb, we will use an initial normal stiffness  $k_{n,0}$  which is three orders of magnitude larger than the equivalent normal stiffness of the adjacent continuum elements and apply the same value to the initial shear stiffness  $k_{t,0}$ .

For crack initiation, we adopt the following criterion

$$t_n = f_t \quad (2.2)$$

with  $t_n$  the normal traction computed from Equation (2.1) and  $f_t$  the uniaxial tensile strength. At crack initiation, we replace the constitutive relation of Equation (2.1) by

$$\begin{bmatrix} t_n \\ t_t \end{bmatrix} = \begin{bmatrix} k_n & 0 \\ 0 & k_t \end{bmatrix} \begin{bmatrix} \Delta u_n \\ \Delta u_t \end{bmatrix} \quad (2.3)$$

with  $k_n$  and  $k_t$  the *secant* normal and shear stiffness, respectively. Since the initial stiffnesses  $k_{n,0}$  and  $k_{t,0}$  have been chosen such that the elastic deformations of the interface element are small compared to the actual crack width  $w$ , for the cracked stage we assume  $\Delta u_n = w$  and  $\Delta u_t = s$  with  $w$  and  $s$  the crack opening and sliding displacement, respectively (see Figure 2.1a). By adopting a damage formulation, we can express the secant normal stiffness as

$$k_n = (1 - d_n)k_{n,0} \quad (2.4)$$

with  $d_n$  a damage parameter which equals 0 at crack initiation and 1 as soon as the ultimate crack width  $w_u$  has been attained. We can set up a similar relation for the secant shear stiffness

$$k_t = (1 - d_t)k_{t,0} \quad (2.5)$$

For convenience sake, we assume isotropic damage

$$d_n = d_t = d \quad (2.6)$$

In other words, the normal and shear stiffness decrease at the same rate.

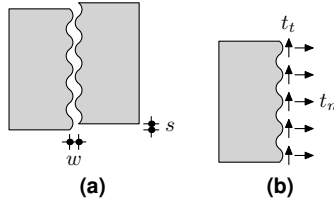


**Figure 2.1** Opening ( $\Delta u_n = w$ ) and sliding ( $\Delta u_t = s$ ) displacements (a) and the corresponding normal ( $t_n$ ) and shear ( $t_t$ ) tractions (b) of the discrete crack model.

The initiation of a crack does not mean that the present tractions (see Figure 2.1b) vanish instantly. In fact, for small crack widths  $w$  still a normal traction can be transmitted across the crack, although  $t_n$  diminishes upon increasing  $w$ . This phenomenon is called *tension softening* and we take it into account by adopting a cohesive law. In general, cohesive laws include at least two parameters: the uniaxial tensile strength  $f_t$  and the fracture energy  $G_f^I$ . Optionally, additional parameters are used to further define the relation between  $t_n$  and  $w$ . In our work, we assume  $G_f^I$  to be a material property that is to be interpreted as the amount of energy required to create a crack face of a unit area and which is equal to the area enclosed by the  $t_n$ - $w$  curve [36].

The literature provides a wide range of formulations for the cohesive law (also known as tension softening relation). In our work we employ three different descriptions: linear and exponential tension softening, and a tension softening law proposed by Hordijk [37]. Figure 2.2a shows a schematic representation of the linear softening relation which reads

$$t_n(w) = \begin{cases} f_t \left(1 - \frac{w}{w_u}\right) & \text{if } w \leq w_u \\ 0 & \text{if } w > w_u \end{cases} \quad (2.7)$$

with  $w_u = 2 \frac{G_f^I}{f_t}$  the ultimate crack width. The exponential tension softening law used in this work is shown in Figure 2.2b and it reads

$$t_n(w) = f_t \exp\left(-\frac{f_t}{G_f^I} w\right) \quad (2.8)$$

Note that due to its exponential character no ultimate crack width  $w_u$  exists. For practical reasons, we assume full tension softening after 98% of the fracture energy has been released, which results in  $w_u \approx 3.91 \frac{G_f^I}{f_t}$ . The nonlinear softening relation

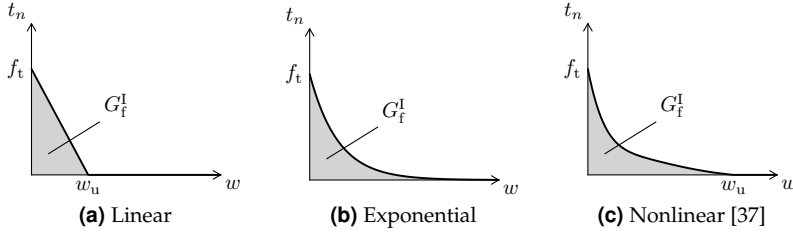


**Figure 2.2** Three tension softening relations for discrete crack models that are used throughout this work.

proposed by Hordijk [37, 11] is shown in Figure 2.2c and it can be written as

$$t_n(w) = \begin{cases} f_t \left[ \left( 1 + \left( c_1 \frac{w}{w_u} \right)^3 \right) \exp \left( -c_2 \frac{w}{w_u} \right) - \frac{w}{w_u} (1 + c_1^3) \exp(-c_2) \right] & \text{if } w \leq w_u \\ 0 & \text{if } w > w_u \end{cases} \quad (2.9)$$

with  $c_1 = 3$ ,  $c_2 = 6.93$ , and  $w_u = 5.14 \frac{G_f^I}{f_t}$ .

## 2.1.2 Smearing crack model

Contrary to the discrete crack model, the smeared crack model distributes the geometrical discontinuities that arise in the fracture zone over the continuum as shown in Figure 2.3. Consequently, the use of interface elements is no longer needed which means that the analyst does not need to indicate in which parts of the model cracking is expected. Moreover, due to the absence of interface elements the crack orientation is not predefined which allows cracks to initiate and propagate in any direction. Like for the discrete crack model, we limit the use of the smeared crack concept in the present work to two-dimensional models.

Assuming plane stress conditions, we adopt the following isotropic constitutive relation for the elastic stage

$$\begin{bmatrix} \sigma_{xx} \\ \sigma_{yy} \\ \sigma_{xy} \end{bmatrix} = \frac{E_0}{1 - \nu_0^2} \begin{bmatrix} 1 & \nu_0 & 0 \\ \nu_0 & 1 & 0 \\ 0 & 0 & \frac{1 - \nu_0}{2} \end{bmatrix} \begin{bmatrix} \varepsilon_{xx} \\ \varepsilon_{yy} \\ \gamma_{xy} \end{bmatrix} \quad (2.10)$$

with  $E_0$  and  $\nu_0$  the initial Young's modulus and Poisson's ratio, respectively.

For crack initiation we employ the following stress-based criterion

$$\sigma_1 = f_t \quad (2.11)$$

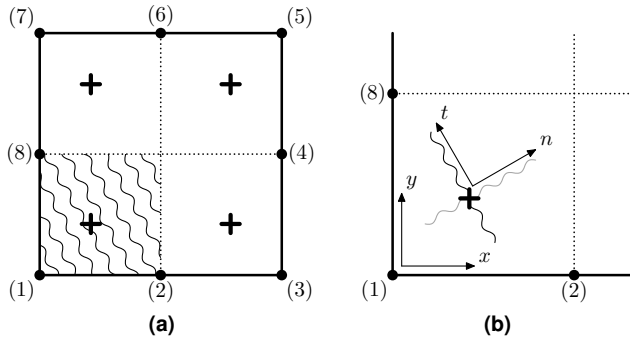


**Figure 2.3** (a) A partially cracked eight-noded plane stress element. The cracks are smeared out over the tributary area of an integration point (+). (b) Upon primary crack initiation the crack axes system is fixed with the  $n$ -axis perpendicular to the primary crack. Optionally, a secondary crack—perpendicular to the primary crack—may arise.

with  $\sigma_1$  the maximum principal stress and  $f_t$  the uniaxial tensile strength. The corresponding principal direction determines the crack orientation. To denote the crack strains and stresses, we introduce crack axes  $n$  and  $t$  that are aligned accordingly. By definition, the  $n$ -axis is chosen normal to the crack face, whereas the  $t$ -axis points in tangential direction as shown in Figure 2.3b. We fix the crack orientation once the crack has initiated to avoid that the crack direction will also become a status variable. Thus we adopt a *fixed* crack approach as opposed to the rotating crack approach.

Upon crack initiation, we replace the isotropic constitutive relation of Equation (2.10) by the following orthotropic formulation [15]

$$\begin{bmatrix} \sigma_{nn} \\ \sigma_{tt} \\ \sigma_{nt} \end{bmatrix} = \frac{1}{1 - \nu_{tn}\nu_{nt}} \begin{bmatrix} E_n & \nu_{nt}E_n & 0 \\ \nu_{tn}E_t & E_t & 0 \\ 0 & 0 & (1 - \nu_{tn}\nu_{nt})G \end{bmatrix} \begin{bmatrix} \varepsilon_{nn} \\ \varepsilon_{tt} \\ \gamma_{nt} \end{bmatrix} \quad (2.12)$$

with  $E_n$  and  $E_t$  the apparent stiffness in normal and tangential direction, respectively, and  $G$  the shear modulus. Poisson's ratio of transverse extensional strain in the  $t$ -direction to axial extensional strain in  $n$ -direction is denoted by  $\nu_{nt}$ . A similar definition applies to Poisson's ratio  $\nu_{tn}$ . When the first crack occurs, we adopt a secant stiffness for  $E_n$  whereas we retain the initial stiffness  $E_0$  for  $E_t$ . In this way, compressive struts may develop parallel to diagonal cracks which is relevant for reinforced concrete (RC) analysis. Optionally, a second crack may develop perpendicular to the first one as shown in Figure 2.3. In that case, we replace  $E_t$  by a secant stiffness as well, which is independent of  $E_n$ . As a crack develops, the strain  $\varepsilon_{nn}$  may grow large, resulting in a large transversal strain  $\varepsilon_{tt}$  through the Poisson effect. To limit spurious cracking in transversal direction, we reduce the orthogonal Poisson's ratios at the same rate as the corresponding secant stiffness,

i.e.

$$\nu_{tn} = \nu_0 \frac{E_n}{E_0} \quad (2.13)$$

$$\nu_{nt} = \nu_0 \frac{E_t}{E_0} \quad (2.14)$$

Since we adopt a fixed crack model, we need to define a shear retention relation. The reason is that as a crack develops, the principal directions may start to deviate from the crack orientation which implies that shear stresses acting at the crack face are built up. A shear retention relation describes the development of the shear modulus  $G$ . In its simplest form,  $G$  is reduced by a constant factor  $\beta$ :

$$G = \beta G_0 = \beta \frac{E_0}{2(1 + \nu_0)} \quad (2.15)$$

with  $G_0$  the initial shear modulus. However, adopting this relation may result in excessive stress-locking, even for small values of  $\beta$ . Another undesired side effect of using a small  $\beta$  is a large decrease in shear stiffness at crack initiation. In the present work, we adopt the physically more appealing formulation proposed by DeJong, Hendriks, and Rots [16]

$$G = \frac{E_{\min}}{2(1 + \nu_{\min})} \quad (2.16)$$

with  $E_{\min}$  the smallest (secant) stiffness

$$E_{\min} = \min(E_n, E_t) \quad (2.17)$$

and  $\nu_{\min}$  the smallest Poisson's ratio

$$\nu_{\min} = \min(\nu_{tn}, \nu_{nt}) \quad (2.18)$$

For the smeared crack model, the tension softening behavior can be described in a similar way as we did for the discrete crack model. However, since the crack is smeared out over the continuum, a characteristic length  $\ell$  needs to be introduced. In this thesis, we have used the defaults offered by the DIANA finite element package. That is, for linear two-dimensional elements we use  $\ell = \sqrt{2A}$  and for higher-order two-dimensional elements we adopt  $\ell = \sqrt{A}$ , with  $A$  the element area. In literature,  $\ell$  is referred to as *crack band width* and it is frequently denoted by  $h$ . By adopting this convention (which we will continue to use in the remainder of this work) we can represent the crack opening displacement  $w$  by an equivalent crack extensional strain  $\varepsilon^{\text{cr}}$

$$\varepsilon^{\text{cr}} = \frac{w}{h} \quad (2.19)$$

Along the same lines, we can define a crack shear strain  $\gamma^{\text{cr}}$  which corresponds to the crack sliding displacement  $s$  of the discrete crack model.

As pointed out by Bažant and Oh [3], the adopted tension softening relation should take  $h$  into account in order to avoid mesh size dependency. Consequently, the area enclosed by a softening curve for the smeared crack model equals  $\frac{G_f^I}{h}$ . The softening relations introduced for the discrete crack model can now be formulated in terms of  $\varepsilon^{cr}$ . The linear tension softening law of Equation (2.7) reads in a continuum formulation

$$\sigma(\varepsilon^{cr}) = \begin{cases} f_t \left(1 - \frac{\varepsilon^{cr}}{\varepsilon_u^{cr}}\right) & \text{if } \varepsilon^{cr} \leq \varepsilon_u^{cr} \\ 0 & \text{if } \varepsilon^{cr} > \varepsilon_u^{cr} \end{cases} \quad (2.20)$$

with  $\varepsilon_u^{cr} = \frac{2G_f^I}{hf_t}$  the ultimate crack strain. Similarly, the exponential softening relation of Equation (2.8) can be expressed as

$$\sigma(\varepsilon^{cr}) = f_t \exp\left(-\frac{hf_t}{G_f^I} \varepsilon^{cr}\right) \quad (2.21)$$

And finally, the nonlinear softening function proposed by Hordijk [37] reads in a smeared crack formulation [51]

$$\sigma(\varepsilon^{cr}) = \begin{cases} f_t \left[ \left(1 + \left(c_1 \frac{\varepsilon^{cr}}{\varepsilon_u^{cr}}\right)^3\right) \exp\left(-c_2 \frac{\varepsilon^{cr}}{\varepsilon_u^{cr}}\right) - \frac{\varepsilon^{cr}}{\varepsilon_u^{cr}} (1 + c_1^3) \exp(-c_2) \right] & \text{if } \varepsilon^{cr} \leq \varepsilon_u^{cr} \\ 0 & \text{if } \varepsilon^{cr} > \varepsilon_u^{cr} \end{cases} \quad (2.22)$$

In this thesis we will work with smeared crack models formulated in terms of total strain  $\varepsilon$ . Here we assume the total strain to be the sum of the elastic strain  $\varepsilon^{el}$  and the crack strain  $\varepsilon^{cr}$

$$\varepsilon = \varepsilon^{el} + \varepsilon^{cr} \quad (2.23)$$

Figure 2.4 illustrates this relationship. Before cracking occurs, i.e. before the peak strain  $\varepsilon_p$  is attained, the response is fully elastic. Upon increasing  $\varepsilon$  beyond  $\varepsilon_p$  a crack is introduced and the stress that is transmitted across the crack starts to decrease. Consequently, the contribution of  $\varepsilon^{el}$  to  $\varepsilon$  decreases as well since it depends linearly on the stress  $\sigma$

$$\varepsilon^{el} = \frac{\sigma}{E_0} \quad (2.24)$$

As soon as  $\varepsilon$  grows larger than the ultimate crack strain  $\varepsilon_u$  the elastic strain component has reduced to zero, which means that total strain values exceeding  $\varepsilon_u$  are fully determined by  $\varepsilon^{cr}$ . Note that the softening tail in a total strain formulation cannot be described with the expression in terms of  $\varepsilon^{cr}$  (e.g. Equation (2.22)). In fact, it may not even be possible to find an explicit analytical expression for  $\sigma$  in terms of  $\varepsilon$ , whereas an explicit relation between  $\sigma$  and  $\varepsilon^{cr}$  does exist. Figure 2.5 shows the three earlier introduced tension softening relations in terms of  $\varepsilon$ .

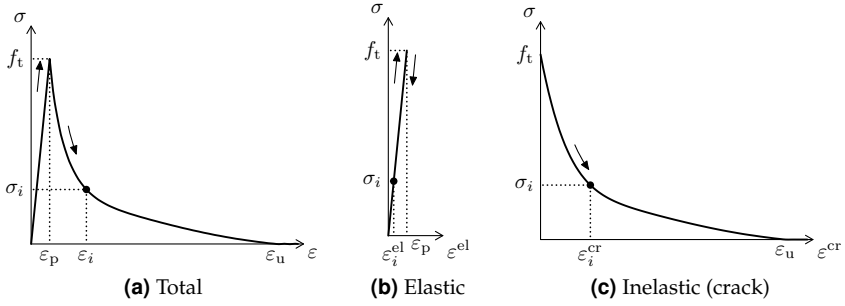


**Figure 2.4** Relation between a total strain formulation and its components.

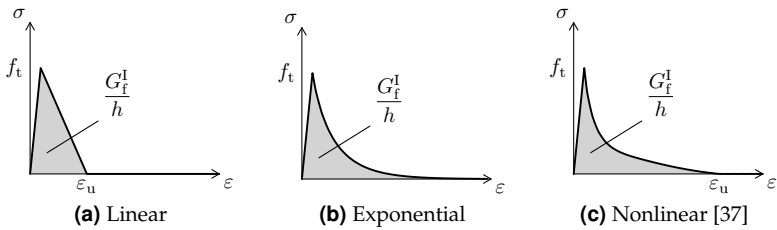


**Figure 2.5** Three tension softening relations for smeared crack models using a total strain formulation that are used throughout this work.

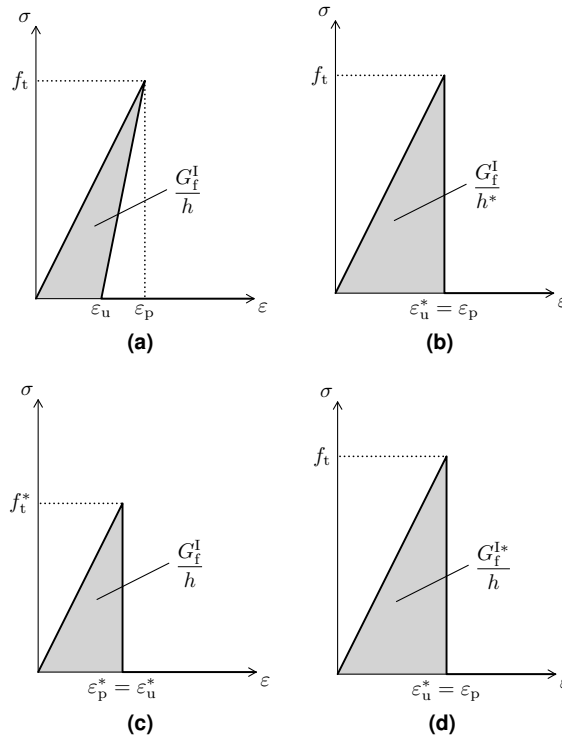


**Figure 2.6** Ways to resolve a snap-back at constitutive level (a) include refining the mesh (i.e. decreasing crack band width  $h$ ) (b), lowering uniaxial tensile strength  $f_t$  (c), or increasing fracture energy  $G_f^I$  (d).

In case of relatively large elements and/or materials with extremely brittle properties, a snap-back at constitutive level may occur for the total strain formulation as shown by Figure 2.6a. A typical example is the numerical simulation of large-scale glass structures. However, conventional nonlinear finite element analysis (NLFEA) techniques cannot cope with a snap-back at constitutive level. One way to resolve the snap-back is to refine the mesh (i.e. decrease  $h$  to  $h^*$ ) such that a perfectly brittle behavior is obtained (Figure 2.6b). However, from a computational viewpoint this approach is expensive. Another way to deal with the snap-back would be to resort to perfectly brittle behavior by either lowering  $f_t$  to  $f_t^*$  such that  $G_f^I$  is maintained (Figure 2.6c) or by accepting an increase in  $G_f^I$  to  $G_f^{I*}$  (Figure 2.6d). Note that the latter two options adjust the experimentally obtained material properties to perform the numerical analysis. In Section 3.3 we will show that such adjustments are not required for an SLA-based simulation.



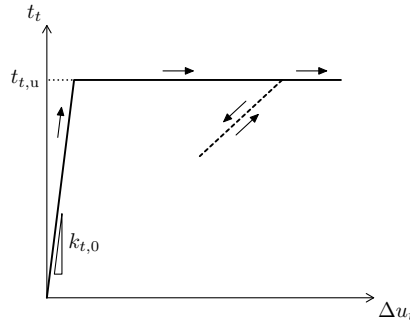


**Figure 2.7** Bilinear relation between bond stress  $t_t$  and slip  $\Delta u_t$  to model the interaction between concrete and steel reinforcement bars.

### 2.1.3 Bond–slip model

To consider the interaction between concrete and steel reinforcement bars a bond–slip relation can be employed. This is essential for the evaluation of crack spacing and maximum crack widths in RC structures. The following components are generally conceived to contribute to the bond between concrete and reinforcement [31]:

- chemical adhesion;
- friction;
- mechanical interlock, i.e. the pushing action of the bar’s lugs against the concrete.

In common practice (at meso- and macro-scale) these effects are not taken into account individually, but lumped in a single bond–slip relation. The literature provides a wide range of sophisticated formulations to describe bond–slip behavior (e.g. Bigaj [6]). In the present work we will limit ourselves to a simple bilinear relation between slip  $\Delta u_t$  and bond stress  $t_t$  as shown in Figure 2.7. The reason is that our aim is to demonstrate that bond–slip behavior can be effectively accounted for in SLA-based simulations. We assign the bond–slip relation in our analyses to zero-thickness interface elements which are located between the concrete and steel elements [48]. Note from Figure 2.7 that we do not take into account the effect of the normal traction  $t_n$  on the shear traction  $t_t$ .

In the elastic stage, the response of the interface elements is described by

$$\begin{bmatrix} t_n \\ t_t \end{bmatrix} = \begin{bmatrix} k_{n,0} & 0 \\ 0 & k_{t,0} \end{bmatrix} \begin{bmatrix} \Delta u_n \\ \Delta u_t \end{bmatrix} \quad (2.25)$$

with  $k_{n,0}$  and  $k_{t,0}$  the initial normal and shear stiffness, respectively.

Debonding starts when the following condition is met

$$t_t = t_{t,u} \quad (2.26)$$

with  $t_{t,u}$  the ultimate bond stress. Then we replace the constitutive relation of Equation (2.25) by

$$\begin{bmatrix} t_n \\ t_t \end{bmatrix} = \begin{bmatrix} k_{n,0} & 0 \\ 0 & k_t \end{bmatrix} \begin{bmatrix} \Delta u_n \\ \Delta u_t \end{bmatrix} \quad (2.27)$$

with  $k_t$  the secant shear stiffness. Note that we retain the initial normal stiffness  $k_{n,0}$  throughout the analysis.

### 2.1.4 Coulomb friction model

To describe problems that involve sliding failure we will adopt the Coulomb friction model which we assign to interface elements. In the same way as the previously described material models, also here we limit ourselves to the two-dimensional case. As a result the variables involved are the relative normal and sliding displacements,  $u_n$  and  $u_t$ , respectively. Note that we have omitted the ‘ $\Delta$ ’ symbol here which is commonly used to denote that the displacement is relative. The reason is that in Section 4.3 we will consider variations of the relative displacement and we will introduce the ‘ $\Delta$ ’ there to denote this variation. The corresponding normal and shear tractions are denoted by  $t_n$  and  $t_t$ , respectively, and for the elastic stage they are related to the relative displacements in the following way

$$\begin{bmatrix} t_n \\ t_t \end{bmatrix} = \begin{bmatrix} k_{n,0} & 0 \\ 0 & k_{t,0} \end{bmatrix} \begin{bmatrix} u_n \\ u_t \end{bmatrix} \quad (2.28)$$

with  $k_{n,0}$  and  $k_{t,0}$  the initial normal and shear stiffness, respectively.

The essence of the Coulomb friction model is that the sliding resistance along a plane depends on the normal traction  $t_n$  and the mobilized cohesion  $c$ . The corresponding failure criterion can be denoted as

$$|t_t| = -t_n \tan \phi + c \quad (2.29)$$

with  $|t_t|$  the maximum shear traction (in absolute sense) along the sliding plane and  $\tan \phi$  the mobilized friction coefficient. Figure 2.8a shows a graphical representation of the failure criterion. The filled area indicates all possible combinations of normal and shear traction, and the bold black line represents the failure contour.

For non-smooth sliding planes, a phenomenon called *dilatancy* may come into play. That means a body may be uplifted upon shearing over another body due to protrusions as shown in Figure 2.9. This effect is quantified by a dilatancy angle  $\psi$  which relates the plastic relative normal displacement  $u_n^{\text{pl}}$  to the plastic relative shear displacement  $u_t^{\text{pl}}$

$$u_n^{\text{pl}} = |u_t^{\text{pl}}| \tan \psi \quad (2.30)$$

In case the shearing bodies are confined, the uplift displacement is restrained resulting in additional compressive stresses.

Different kinds of hardening and softening phenomena, including cohesion softening, frictional softening and dilatancy softening, may affect the shearing behavior. In the present work we will only consider cohesion softening. We assume

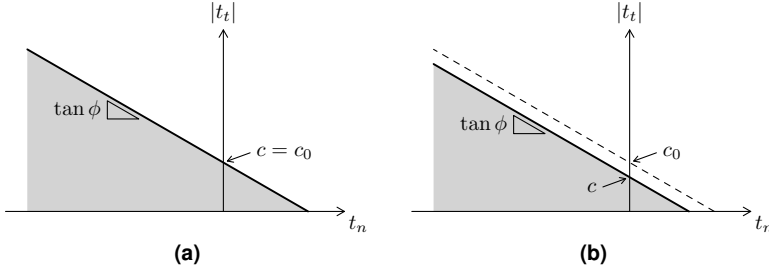


**Figure 2.8** (a) Coulomb friction failure contour and (b) the effect of cohesion softening on this contour.

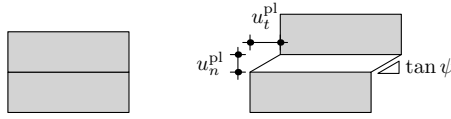


**Figure 2.9** The angle of dilatancy  $\psi$  relates the amount of uplift  $u_n^{\text{pl}}$  to the amount of plastic shear deformation  $u_t^{\text{pl}}$  across a joint [14].

the cohesion to decrease exponentially as a function of the so-called plasticity parameter  $\kappa$  [45]

$$c(\kappa) = c_0 \exp\left(-\frac{c_0}{G_f^{\text{II}}} \kappa\right) \quad (2.31)$$

with  $c_0$  the initial cohesion and  $G_f^{\text{II}}$  the mode II fracture energy. Here we assume the plasticity parameter  $\kappa$  to be equal to the largest plastic relative shear displacement (in absolute sense) [45]

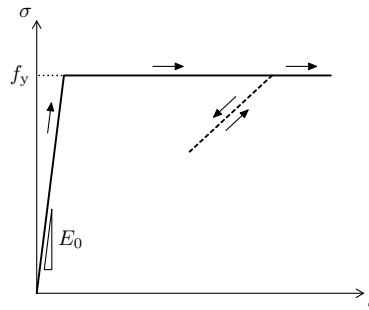
$$\kappa = \max |u_t^{\text{pl}}| \quad (2.32)$$

Figure 2.8b shows that the effect of cohesion softening is a uniform vertical shift of the yield contour.

Throughout this work we will assume the following consistent tangent stiffness matrix to compute traction increments from relative displacement increments for the inelastic stage

$$\mathbf{D}_{\text{tan}} = \frac{1}{k_{n,0} \tan \phi \tan \psi + k_{t,0}} \begin{bmatrix} k_{n,0} k_{t,0} & -k_{n,0} k_{t,0} \tan \psi \frac{t_t}{|t_t|} \\ -k_{n,0} k_{t,0} \tan \phi \frac{t_t}{|t_t|} & k_{n,0} k_{t,0} \tan \phi \tan \psi \end{bmatrix} \quad (2.33)$$

This matrix has been derived from the one used by Lourenço [45]. The difference here is that we have set the cohesion softening term to zero. In this way, we make the discretization of the constitutive relation, which is required for SLA (see Section 2.3), slightly less complicated since it eliminates a state parameter.



**Figure 2.10** Stress–total strain relation assumed for (steel) reinforcement bars.

### 2.1.5 Uniaxial elastic–perfectly plastic model

To describe the structural behavior of (steel) reinforcement bars we will adopt the uniaxial elastic–perfectly plastic material model shown in Figure 2.10. As for the smeared crack model of Subsection 2.1.2, we use a total strain based formulation. The Young’s modulus  $E_0$  determines the elastic branch and the total stress  $\sigma$  cannot exceed the yield limit  $f_y$ . Since SLA inherently models unloading in a secant way (see Section 2.4), we abandon the elastic unloading concept which is commonly used for this kind of material model. This limits the ability to apply cyclic loading or load reversal.

## 2.2 Towards a non-iterative approach

This section discusses the reasons for the development of SLA and which ideas from other methods inspired its development.

**Motivation** Most nonlinear finite element codes in use today are based on some incremental-iterative scheme. The basic idea of this technique is to apply the loads (being nodal forces and/or imposed displacements) in increments. After each increment an iterative procedure—typically a Newton-Raphson scheme—is started to solve the resulting system of nonlinear equations. A properly converged solution of this system of equations represents a state of global equilibrium. In this context “properly converged” means that the unbalance between the internal and external forces should not exceed a preset tolerance. For a detailed description of the incremental-iterative technique and its many solution procedures the reader is referred to standard textbooks, e.g. Crisfield [13].

Over the past decades numerous approaches have been proposed to improve the performance and numerical stability of the incremental-iterative procedure. These include the pioneering work by Riks [55] and the alternative formulation by Crisfield [12]. Also advanced approaches such as indirect displacement control [9]

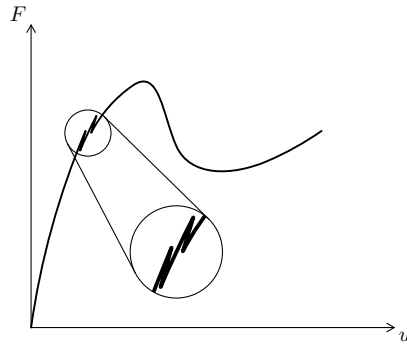


**Figure 2.11** Non-smooth load–displacement curve for a single degree of freedom system.

and more recently a dissipation-based arc-length method [32] are worth mentioning. Nevertheless, it remains a challenge to devise a method that is unconditionally stable.

Despite successful results have been reported, the usability of incremental-iterative schemes for failure analysis of RC and masonry structures remains a challenge. We do not argue that the developers of improved solution procedures are not able to obtain reliable results with their work. Structural engineers on the other hand are generally less familiar with the concepts of NLFEA and its accompanying pitfalls. In other words, the quality and reliability of obtained analysis results heavily depend on the analyst’s skills and experience. The overwhelming number of options that are offered by modern software packages requires considerable expertise from the end-user. Furthermore, the success of incremental-iterative approaches is usually demonstrated for relatively small models and laboratory benchmarks. Evaluation of these approaches for real-world large-scale structures made of softening materials have received less attention.

Convergence problems may occur frequently in the analysis of quasi-brittle structures using incremental-iterative schemes. These problems may be attributed to the generally non-smooth response of quasi-brittle structures. Figure 2.11 demonstrates this for a single degree of freedom system. It is this irregularly-shaped equilibrium path that makes it difficult for path-following techniques to trace it.

**Inspiration** To address the mentioned convergence problems, Rots [57] proposed a new method which was partially inspired by engineering practice. In the structural concrete community, it is common practice to reduce the stiffness in areas where cracking is expected. In this way, the stress redistribution due to cracking can be taken into account with a simple linear-elastic analysis. The concept of SLA is based on this idea. However, instead of assigning some reduced stiffness to elements that are expected to crack, the selection procedure is automated.

Another source of inspiration for the development of SLA was the lattice models. These models—which have emerged from the study of disordered media—

approximate a continuum by a network of elastic truss or beam elements. Each truss or beam element represents the material on a mesoscopic level and it will break as soon as the governing stress in the element exceeds a certain threshold value. In the original formulation by Herrmann, Hansen, and Roux [35], such a broken element is permanently removed from the model. Per cycle—which simply is a linear-elastic analysis of the current configuration—only one element can be broken. Due to the unbalance arising from the element removal, stresses will be redistributed in the next cycle. Hence, the order in which the elements will be broken is unknown in advance and can only be found sequentially. The mechanical properties of the elements can be assigned either by using a random distribution or by projecting a particle distribution on top of the lattice. The last option is well-suited for the modeling of inhomogeneous materials like concrete at a micro- or mesoscopic level. In that case the stiffness and strength properties of an element depend on its location within the particle distribution (e.g. inside an aggregate, the matrix or the interfacial zone between aggregate and matrix). Schlangen and Van Mier [65] have successfully simulated small scale laboratory tests using their two-dimensional lattice model and Lilliu [43] has extended their model to three dimensions. Nevertheless, lattice models have also been successfully applied at a macroscopic level—where the material inhomogeneities are smeared out over the continuum resulting in a homogeneous material model—see for instance the work by Bolander, Hong, and Yoshitake [8].

The approach proposed by Beranek and Hobbelman [5], which also makes use of lattices, inspired the development of SLA as well. Their model, which follows a physical rather than a phenomenological approach, is to be used for modeling concrete at macro level. It uses a regular assemblage of equal spheres in their most dense configuration to describe the structure of the material. The spheres are assumed fully rigid and all stiffness and strength is attributed to a contact layer around the contact points of the spheres. A tensile failure criterion based on Mohr's circles is applied to the contact layer. For the numerical analysis they replace the assemblage of spheres by an equivalent regular two- or three-dimensional lattice along the system lines of the spherical model. The mechanical behavior of the members connecting the centers of the spheres is assumed to be linear-elastic. They introduce nonlinear effects by stepwise degradation of the mechanical properties of the most affected members. The selection procedure for the next critical member is identical to the approach outlined for lattice models.

## 2.3 Introduction to stepwise secant material laws

A fundamental assumption of SLA is to adopt a stepwise secant material law which approximates the underlying nonlinear constitutive relation. Figure 2.12a shows an example of such a stepwise secant material law for a linear strain-softening relation. In the literature, a stepwise secant material law is often referred to as saw-tooth law due to its appearance. In essence, the base material law is approxi-

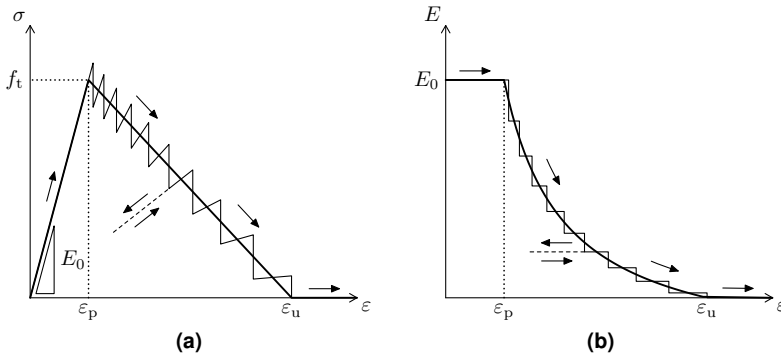


**Figure 2.12** (a) Example of a stepwise secant material law (saw-tooth law). (b) Reduction of Young's modulus  $E$  upon increasing strain for a softening material.

mated by a series of linear relations, starting from the elastic branch (in the figure denoted by  $E_0$ ). As soon as the stress limit is attained, the next secant relation (with reduced stiffness and strength properties) is assumed. This process of reducing the stiffness upon attaining a stress limit is repeated until all stiffness has vanished which corresponds to a state of complete damage. Chapter 3 elaborates on ways to set up a stepwise secant material law.

Figure 2.12b shows another representation of the same key assumption. Initially, the material behaves linear-elastically which means that the stiffness  $E_0$  is maintained. However, as soon as the total strain  $\varepsilon$  exceeds the strain corresponding to the peak stress (in the figure denoted by  $\varepsilon_p$ ), the material starts to degrade progressively. For the base material law, the Young's modulus  $E$  reduces in a continuous way, whereas for the saw-tooth law the stiffness reduces in a stepwise manner.

From a damage mechanics viewpoint, the effect of the assumed stepwise secant material law may also be considered as a series of damage increments. Note that the apparent secant stiffness  $E$  can be expressed as a fraction of the initial stiffness  $E_0$  by introducing a damage parameter  $d$

$$E = (1 - d)E_0 \quad (2.34)$$

For the base material law, the secant stiffness reduces in a continuous way as demonstrated earlier by Figure 2.12b. Hence, the damage parameter  $d$  grows continuously from 0 at crack initiation to 1 when the total strain exceeds the ultimate strain  $\varepsilon_u$ . However, for a saw-tooth law, the stiffness is reduced stepwise. Consequently, the damage parameter  $d$  increases in a discrete fashion and the number of damage parameter values  $d_k$  is finite. Thus a jump from one secant branch to the next implies a damage increment.

A feature of the saw-tooth law is that unloading inherently follows a secant path as outlined in Figure 2.12a. This suggests that a stepwise secant material

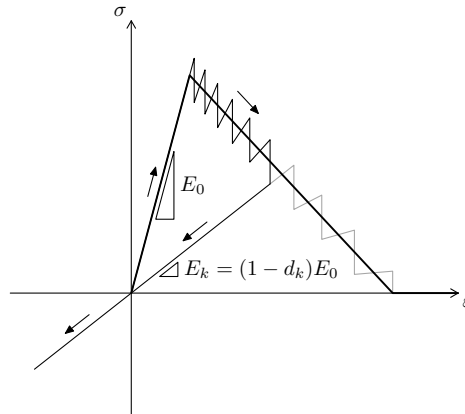


**Figure 2.13** The reduced stiffness  $E_k$  caused by tensile failure is preserved upon load reversal.

law is less suitable for modeling elasto-plastic materials, like steel reinforcement bars, since they unload in an elastic fashion. Nevertheless, for monotonic loading situations where unloading only occurs locally, the use of a saw-tooth law for this type of material may still produce acceptable results.

Another feature of the stepwise secant material law as presented in the literature is that the reduced secant stiffness is maintained, even when local load reversal occurs. That is, stiffness decrease due to tensile failure is maintained in case the material is reloaded in compression. A similar statement holds in case the material is initially damaged in compression and later on reloaded in tension. Figure 2.13 exemplifies this feature. Generally, for monotonic loading the stress redistributions will not be that pronounced that load reversal occurs frequently, but for some cases (e.g. [24]) it led to undesired effects.

## 2.4 Event-by-event strategy

In this section, we revisit the SLA solution procedure, also known as an event-by-event strategy [61], originally proposed by Rots [57]. The flowchart in Figure 2.14 shows the steps involved in this procedure. Basically, the structural response of the model is captured by a sequence of subsequent *events*. In the context of SLA an event is to be understood as the initiation or propagation of damage at some point in the model. In the current work, we limit ourselves to the following types of events:

- Initiation or propagation of a crack due to tensile failure.
- Onset or progression of yielding of a reinforcement bar.
- Initiation or propagation of reinforcement bar debonding.



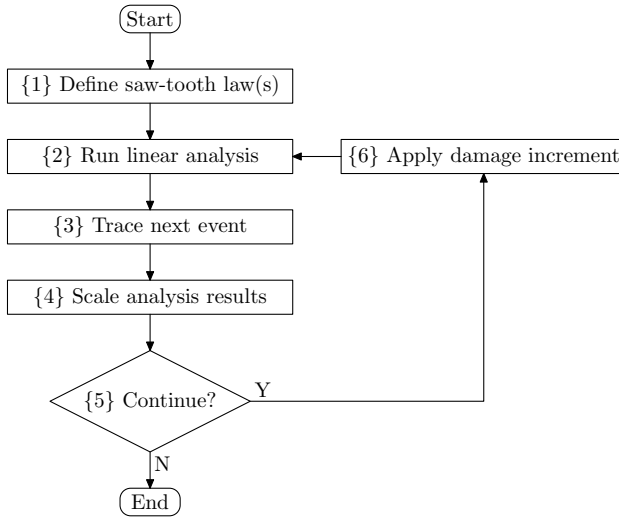


**Figure 2.14** Flowchart of the steps involved in the event-by-event strategy.

- Onset or progression of sliding along an interface.

However, we do not see any fundamental objections to include other types of events as well, such as the initiation or propagation of material crushing.

The first step is to define one or more saw-tooth laws for the nonlinear material behavior that needs to be included in the finite element analysis. The previous section introduced the notion of a saw-tooth law. Chapters 3 and 4 elaborate on how to establish these approximations.

The second step is to perform a linear analysis of the model. Since the load will be multiplied with a suitable factor in step {4}, its magnitude is not important at this stage, so a simple unit load suffices. However, in case of non-proportional loading, the load that is not to be scaled should have its actual magnitude. This will be discussed in detail in Chapter 5. Since at each integration point of the model a linear relation exists between deformation and stress, the resulting system of equations can be solved in a standard manner. At the end of this step in each integration point of the model, the deformations and corresponding stresses for the given load are known.

The third step is to identify which event will occur in the current cycle  $j$ . This is accomplished in two sub steps. First, for each integration point  $i$  a critical load multiplier  $\lambda_{\text{crit};i}^{(j)}$  is calculated based on the governing stress component  $\sigma_{\text{gov};i}^{(j)}$  and the current material strength  $f_i^{(j)}$ :

$$\lambda_{\text{crit};i}^{(j)} = \frac{f_i^{(j)}}{\sigma_{\text{gov};i}^{(j)}} \quad (2.35)$$

Subsequently, the smallest value of all calculated load multipliers  $\lambda_{\text{crit};i}^{(j)}$  is selected as the critical load multiplier  $\lambda_{\text{crit}}^{(j)}$  at model level:

$$\lambda_{\text{crit}}^{(j)} = \min \left( \lambda_{\text{crit};i}^{(j)} \right) \quad \text{for all } \lambda_{\text{crit};i}^{(j)} > 0 \quad (2.36)$$

The key idea here is that upon multiplication of the load with factor  $\lambda_{\text{crit}}^{(j)}$  the smallest load that will lead to progressive damage is obtained.

Step {4} scales the applied load with the critical load multiplier  $\lambda_{\text{crit}}^{(j)}$ , resulting in a critical stress state. That is, at one integration point the governing stress equals the current material strength. By tacitly assuming that this indeed happens at only one point, we name it the critical integration point, since there the damage will progress. At all other integration points of the model the governing stresses do not exceed the corresponding material strengths.

The fifth step determines whether or not the analysis should be continued. The simplest approach (which has been used throughout this work) is to check whether a given number of cycles has been executed. In that case, the number of cycles equals the total number of events that will occur in the model. Nonetheless, we do not see any objections that prevent us from using some other stop criterion. For example, we could terminate the analysis as soon as a certain displacement at a given degree of freedom is attained.

In case the analysis is continued (i.e. a next cycle is executed), a damage increment is applied to the critical integration point (Step {6}). That is, the stiffness and strength properties at the critical integration point are instantaneously reduced according to the provided saw-tooth law. Consequently, due to the damage progression a stress redistribution takes place in the next cycle which starts with a new linear analysis. In this way, the structural response of the model is captured by a chain of subsequent events.

**Similar strategies** In literature, several strategies to simulate nonlinear structural behavior have been proposed that are similar to the outlined SLA procedure. Here we briefly revisit some of these approaches that have been developed recently.

De Boer [7] proposed a technique called sequential static analysis that is also based on a series of linear analyses. As is common in NLFEA, he applies the total load in a number of load increments. After applying a load increment, he determines the stresses in the integration points assuming a linear relation with the corresponding strains. Next he checks for all integration points in the model whether the calculated stresses exceed the corresponding (residual) tensile strengths. In case this does not occur he proceeds with the next load increment. However, if stresses exceeding the tensile strength are present, he returns them to the constitutive law as shown in Figure 2.15. Subsequently, the new stress point is used to update the secant stiffness and residual tensile strength. Contrary to what we assume

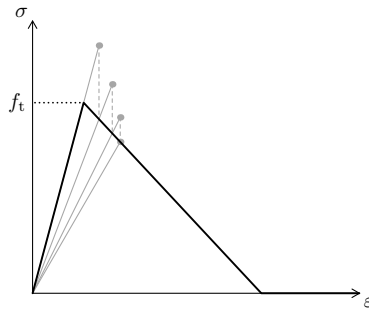


**Figure 2.15** Material degradation scheme adopted by sequential static analysis [7].

for SLA, with his approach it is possible that the secant stiffness is updated simultaneously at multiple integration points, depending on the size of the load increment and the brittleness of the structure. Also note that the stiffness and strength reductions are not predefined, but they are calculated as the analysis progresses. After reducing the material stiffness and strength, he performs another linear analysis that maintains the applied load level. Once again, he checks for any stresses exceeding the tensile strength. The process of reducing the stiffness and strength properties, running a linear analysis and checking the stresses is repeated until at all integration points the stresses are acceptable from a material law point of view. Only then, the load is incremented. The DIANA finite element package offers an implementation of the outlined strategy named stiffness adaptation analysis [49].

Some researchers have combined a total approach, such as SLA, with an incremental approach [28, 30]. They prefer to use the incremental approach throughout the numerical analysis. Only when critical bifurcation points are found they adopt the total approach. Assuming piecewise linear constitutive relations they first compute a critical load factor such that the nearest point connecting two lines is obtained. After this trial step they obtain the true load increment by multiplying the trial load increment with the critical load multiplier. Also the material stiffness is updated accordingly. If no admissible solution can be found in this way, they switch to a total formulation using the secant stiffness to continue the analysis. Here they adopt either the automatic method or the non-iterative energy based method (NIEM). Once this step has been completed they revert to the incremental approach.

Also the continuous, incremental-only tangential analysis (CITA) method, which has been developed by Salam Al-Sabah and Laefer [62], uses piecewise linear constitutive relations. It is similar to SLA in the sense that it employs an event-by-event strategy. However, instead of completely unloading the structure upon the occurrence of an event and then reloading it again, they simply continue the analysis to the next event. Since the method works in an incremental way only, they are forced to use tangent stiffness matrices rather than secant stiffness matrices. The next event is traced by scaling a unit load increment such that for some integration

point the end of the current line in the constitutive relation is reached. For that integration point the tangent stiffness matrix is updated according to the slope of the next line in the constitutive relation. The primary advantage of CITA over SLA is a significant reduction of the required computation time since it needs less analysis steps. On the other hand, indefinite tangent stiffness matrices may arise due to lines with negative slope in case of tension softening. Although such matrices may result in numerical instabilities, they are accepted. It is assumed that the gradual introduction of damage (i.e. a single event per step) provides sufficient analysis control to avoid these problems. So far, no numerical instabilities have been encountered using CITA.

## 2.5 Limitations

This section lists three limitations of the original SLA concept that need to be addressed to make SLA available for a wider range of problems. In fact, the issues presented here form the basis of the next three chapters.

1. *No comprehensive concept to define stepwise secant material laws*

In the literature several methods have been proposed to set up a stepwise secant material law for a given constitutive relation. These methods will be revisited in detail in Section 3.1. The recommended method, the so-called band width ripple concept, has a significantly improved performance with respect to its predecessors. Nonetheless, under certain conditions that method may deliver saw-tooth laws that are not objective with respect to fracture energy and/or ultimate strain. Furthermore, to cope with snap-back at constitutive level an adjusted formulation is required. Chapter 3 proposes two new methods to set up stepwise secant material laws that address these limitations.

2. *No stepwise secant laws for Coulomb friction*

In the literature the concept of a stepwise secant law had only been applied to material behavior that can be adequately described by a relation between one stress component and one deformation component, like simple crack and bond-slip models. However, a proper description of Coulomb friction requires taking into account multiple stress and deformation components. Consequently, the existing methods to set up stepwise secant material laws cannot be adopted to approximate this material behavior. Still many practical applications require the incorporation of Coulomb friction, for example to describe the behavior of joints in masonry. Chapter 4 presents two methods to include Coulomb friction in an SLA simulation.

3. *Non-proportional loading schemes are complex*

So far in this thesis, the treatment of SLA assumed proportional loading which means that all loads are to be scaled with some critical load multiplier. However, when a combination of constant loads (e.g. self-weight) and live loads

need to be considered, the procedure to identify the critical integration point and load multiplier becomes more complex since the constant loads should not be scaled. This is particularly relevant for real-world structures, where non-proportional loading may have a crucial impact on the response. Chapter 5 examines non-proportional loading schemes for SLA in detail.

## 2.6 Summary

This chapter explained that convergence issues in NLFEA were an important reason to start the development of SLA. In particular finite element models that are used to simulate brittle failure are prone to these problems due to the strongly nonlinear behavior of the materials involved. In engineering practice, the effect of cracking is commonly taken into account by reducing the stiffness in areas that are expected to crack. This pragmatic yet effective approach enables engineers to account for stress redistributions using simple linear-elastic analysis. Together with lattice analysis, it proved to be a valuable source of inspiration for the development of SLA.

The stepwise secant material law, also often referred to as saw-tooth law, is one of the fundamentals of the SLA framework. Essentially, it approximates a nonlinear constitutive relation by a finite number of secant branches, representing a stepwise degradation of the material. As soon as the limiting stress of some secant branch in a point of the model is attained, the mechanical properties of that point are instantaneously reduced. These properties include the normal and shear stiffness as well as Poisson's ratio and the material strength. This concept may also be perceived as a series of subsequent damage increments.

The nonlinear response of a structure may be traced by employing the stepwise secant material law in an event-by-event strategy. Basically, the nonlinear behavior is captured by a series of linear analyses. At the end of each linear analysis, the next event (which is to be understood as the initiation or propagation of damage) needs to be determined. That is, the critical load multiplier as well as the corresponding critical integration point need to be identified based on a strength criterion. Subsequently, the damage is incremented at the critical integration point which triggers a stress redistribution in the next linear analysis.

The outlined non-iterative strategy is inherently stable and robust. Nonetheless, it also has a number of limitations which currently restrict the application area. The next three chapters extensively examine the following items and propose extensions to deal with them:

1. There is no comprehensive concept to define a stepwise secant material law available.
2. There is no stepwise secant law available for Coulomb friction.
3. Non-proportional loading schemes are complex.

## Chapter 3 Stepwise secant material laws

The previous chapter revisited and discussed the basic concepts and limitations of sequentially linear analysis (SLA). It explained that a fundamental assumption of SLA is that nonlinear constitutive relations are approximated by stepwise secant laws (in the literature often referred to as saw-tooth laws). Subsequently, a non-iterative event-by-event strategy could be adopted to trace the structural response of the nonlinear finite element model in a robust way.

This chapter demonstrates how stepwise secant material laws (which are essential for SLA) can be set up. Section 3.1 reviews and discusses three methods from the literature. Although the recommended method, which is named the band width ripple concept, generally delivers satisfactory saw-tooth laws, it can be shown that it is not invariant with respect to fracture energy and ultimate strain. However, this is a fundamental requirement in order to achieve numerical analysis results that are insensitive to mesh and/or saw-tooth law refinements. Section 3.2 proposes an improved band width ripple concept that addresses these shortcomings. Another issue that needs attention is snap-back at constitutive level. This phenomenon may occur for total strain crack models involving a combination of low fracture energy and a relatively coarse mesh. Section 3.3 presents a special stepwise secant formulation that covers this case.

The stepwise secant laws presented in this chapter apply to uni-axial stress-strain or traction-relative displacement relations. For material laws formulated in terms of multiple stress and strain/relative displacement components we will adopt another approach. The next chapter elaborates on this topic for the case of Coulomb friction.

### 3.1 Literature review and discussion

This section reviews and discusses three methods to set up stepwise secant material laws. The first SLA studies [57] adopted either a constant stress decrements method or a constant stiffness reductions method to set up saw-tooth laws. Later, for these two methods several regularization techniques were introduced [58] to make them fracture energy invariant. So far, the recommended way to set up saw-tooth laws is to employ the band width ripple concept [59] which is supposed to have an implicit regularization scheme.

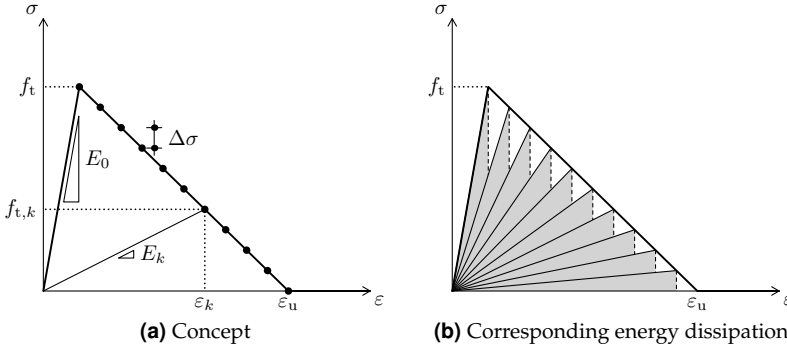


**Figure 3.1** Unregularized saw-tooth law based on the constant stress decrements method with stress decrement  $\Delta\sigma$ .

### 3.1.1 Constant stress decrements method

As suggested by its name, a saw-tooth law set up according to this method is based on points along the softening tail adopting a constant stress decrement  $\Delta\sigma$  which is determined through

$$\Delta\sigma = \frac{f_t}{N} \quad (3.1)$$

with  $f_t$  the initial tensile strength and  $N$  the number of saw-teeth (or damage increments). Figure 3.1a shows the resulting vertically equidistant points along the softening tail. Note that for the special case of linear softening these points are also horizontally spaced at equal distances. For each secant branch  $k$  the reduced tensile strength  $f_{t,k}$  and the corresponding total strain  $\varepsilon_k$  can then be computed from

$$f_{t,k} = \left(1 - \frac{k}{N}\right) f_t \quad (3.2)$$

$$\varepsilon_k = \left(1 - \frac{k}{N}\right) \varepsilon_p + \frac{k}{N} \varepsilon_u \quad (3.3)$$

with  $\varepsilon_p$  the total strain corresponding to the peak stress  $f_t$  and  $\varepsilon_u$  the ultimate strain. Subsequently, the reduced normal stiffness  $E_k$  of secant branch  $k$  can be computed from the reduced tensile strength  $f_{t,k}$  and the strain  $\varepsilon_k$  through

$$E_k = \frac{f_{t,k}}{\varepsilon_k} \quad (3.4)$$

However, Rots and Invernizzi [58] stated that if no additional measures would be taken, the fracture energy associated with the saw-tooth law becomes dependent on the number of saw-teeth  $N$ . To determine the energy consumption associated with the saw-tooth law straight vertical lines are assumed to connect the

individual secant branches (drawn with dashed lines in Figure 3.1b). In fact, the energy dissipation corresponding to the stepwise secant law (indicated with the shaded area in Figure 3.1b) always underestimates the energy consumption  $G_f^I/h$  corresponding to the base material law. However, note that the error diminishes upon increasing  $N$ .

Three ways to regularize the saw-tooth laws were suggested, i.e. to make them fracture energy invariant:

1. Increase the initial tensile strength from  $f_t$  to  $f_t^* = c \cdot f_t$  with  $c > 1$ .
2. Increase the ultimate strain from  $\varepsilon_u$  to  $\varepsilon_u^* = c \cdot \varepsilon_u$  with  $c > 1$ .
3. Combine the previous two options.

For all options, the factor  $c$  has to be chosen such that the energy dissipation corresponding to the saw-tooth law matches the one corresponding to the base law.

Figures 3.2 to 3.4 illustrate the three suggested regularization options. The first one is depicted in Figure 3.2a. The black dots along the softening tail are identical to the ones shown in Figure 3.1a. The black dots along the dashed line are the intersection points of the extended secant branches with the dashed line. The filled area in Figure 3.2b represents the energy consumption associated with the regularized saw-tooth law. A benchmark test on a notched beam showed that by using the first option the numerical results were objective with respect to  $N$ . However, with this approach the peak load was consistently overestimated. Figure 3.3 exemplifies the second regularization option. The black dots along the softening tail and the dashed line (Figure 3.3a) are found in the same way as explained for the first option. The corresponding energy consumption is indicated by the filled area in Figure 3.3b. Contrary to the first option, the benchmark test for the second option revealed that the peak load was underestimated. Figure 3.4a demonstrates the third regularization option. Note that factor  $c$  is used to increase  $f_t$  as well as  $\varepsilon_u$ . Also here, the black dots along the softening tail and dashed line are found in the same way as explained for the first option. The benchmark test showed that this option gives the best results in terms of peak load and post-peak behavior. Moreover, a closed-form expression could be obtained for factor  $c$

$$c = \sqrt{\frac{G_f^I/h}{\sum_{k=0}^{N-1} \frac{1}{2} \varepsilon_k f_{t,k} \left(1 - \frac{E_{k+1}}{E_k}\right)}} \quad (3.5)$$

In general, we have noticed that the use of a constant stress decrement leads to a strong stiffness reduction upon crack initiation. This effect is even more pronounced when the ultimate crack strain  $\varepsilon_u$  is much larger than the total strain at peak stress  $\varepsilon_p$ , which occurs frequently when realistic material parameters are used.



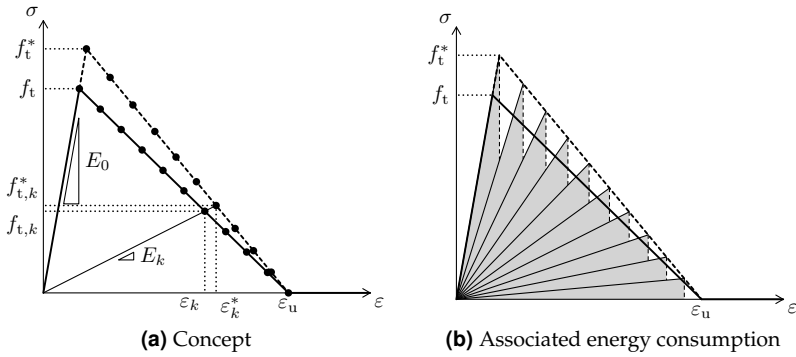


**Figure 3.2** Regularized constant stress decrements method through an increased tensile strength  $f_t^*$ .

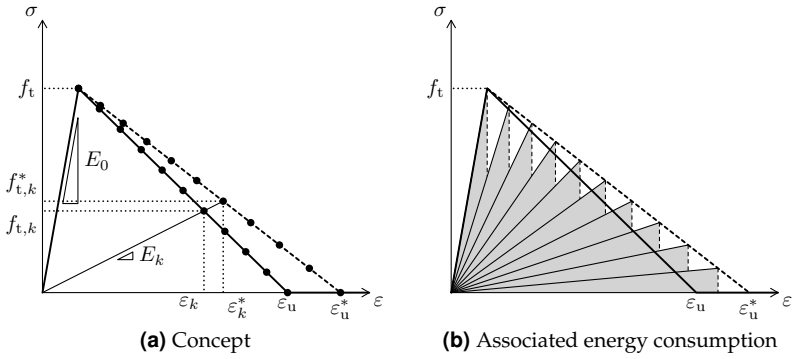


**Figure 3.3** Regularized constant stress decrements method through an increased ultimate strain  $\epsilon_u^*$ .

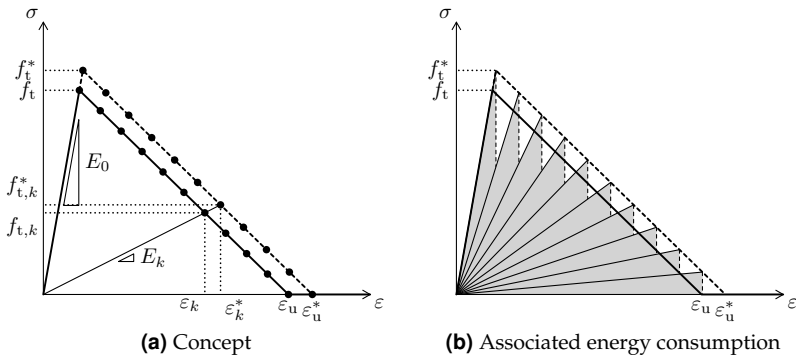


**Figure 3.4** Regularized constant stress decrements method through an increased tensile strength  $f_t^*$  and an increased ultimate strain  $\epsilon_u^*$ .

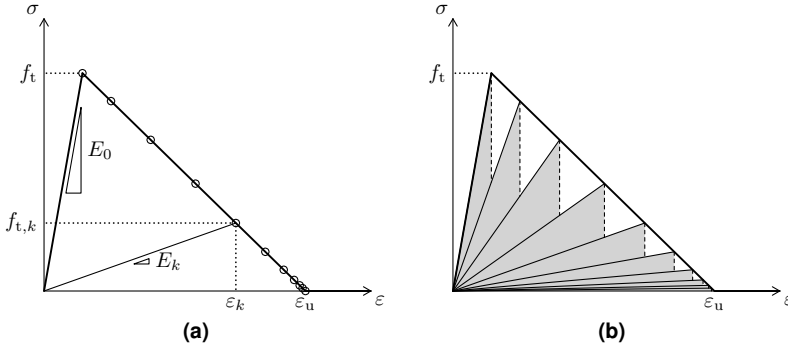


**Figure 3.5** Unregularized saw-tooth law based on the constant stiffness reductions method with reduction factor  $a$  (here  $a = 2$ ).

### 3.1.2 Constant stiffness reductions method

This method for setting up a stepwise secant material law is based on a subsequent reduction of the stiffness by a constant factor  $a$ . That is, the reduced Young's modulus  $E_{k+1}$  corresponding to secant branch  $k + 1$  is calculated from the reduced Young's modulus  $E_k$  corresponding to secant branch  $k$  through the geometric sequence

$$E_{k+1} = \frac{E_k}{a} \quad \text{with } a > 1 \quad (3.6)$$

Note that the reduced stiffness approaches zero asymptotically. Rots and Invernizzi [58] suggested to retain a small dummy stiffness after  $N$  saw-teeth to resemble complete failure. Figure 3.5a shows an example saw-tooth law that was set up with the constant stiffness reductions model using  $a = 2$ .

As for the constant stress decrements method, if no additional measures are taken the energy consumption of the resulting material law becomes dependent on the number of saw-teeth  $N$ . Also here, the energy consumption is always underestimated, regardless the values of  $a$  and  $N$ , as shown by Figure 3.5b. The earlier introduced three regularization options are also applicable to the constant stiffness reductions method. The option that multiplies the tensile strength  $f_t$  as well as the ultimate strain  $\varepsilon_u$  with a factor  $c$  again results in a closed-form solution for factor  $c$

$$c = \sqrt{\frac{G_f^I/h}{\sum_{k=0}^{N-1} \frac{1}{2} (f_{t,k})^2 / E_k b_k}} \quad (3.7)$$

with

$$b_k = \begin{cases} (1 - \frac{1}{a}) & \text{if } 0 \leq k < N \\ 1 & \text{if } k = N \end{cases} \quad (3.8)$$

Figure 3.6 demonstrates the regularized constant stiffness reductions method.

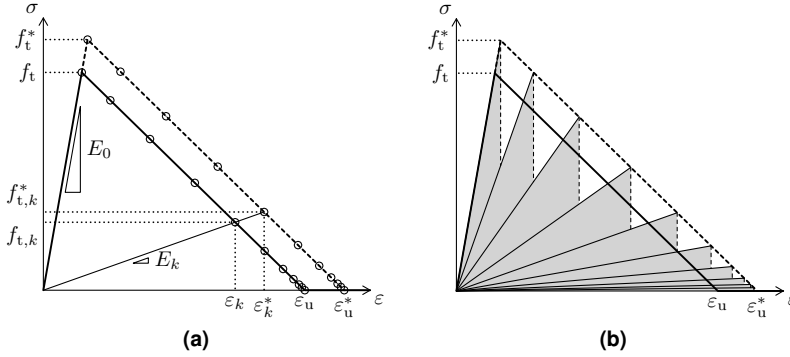


**Figure 3.6** Regularized constant stiffness reductions method through an increased tensile strength  $f_t^*$  and an increased ultimate strain  $\varepsilon_u^*$ .

Compared to the constant stress decrements method, the constant stiffness reductions method generally has a less strong stiffness reduction upon crack initiation depending on the value of  $a$ . On the other hand, as can be seen in the figures of this section, the latter method produces many secant branches that tend to have a low stiffness compared to the initial value.

### 3.1.3 Band width ripple concept

Rots et al. [59] proposed a concept for setting up stepwise secant material laws using a band centered at the base material law as illustrated in Figure 3.7. Two imaginary curves (drawn with dashed lines in the figure) constitute the band. They are the result of shifting the base softening tail over a predefined distance  $pf_t$  in upward and downward direction. Hence, at any point along the base softening tail the band has a width of  $2pf_t$ .

The stepwise secant material law is now set up as follows. Starting from secant branch  $k$ , with reduced stiffness  $E_k$ , the intersection with the uplifted curve is determined first. The corresponding stress limit and total strain are denoted by  $f_{t,k}^+$  and  $\varepsilon_k$ , respectively. Subsequently, the reduced stiffness  $E_{k+1}$  of the next secant branch  $k+1$  is determined by lowering the stress limit to  $f_{t,k}^-$  while maintaining the total strain  $\varepsilon_k$

$$E_{k+1} = \frac{f_{t,k}^-}{\varepsilon_k} \quad (3.9)$$

with

$$f_{t,k}^- = f_{t,k}^+ - 2pf_t \quad (3.10)$$

This process is repeated until the stress limit  $f_{t,k}^+$  becomes smaller than  $2pf_t$  as that would result in a negative lowered stress limit  $f_{t,k}^-$  and thus a negative stiffness  $E_{k+1}$ . Note that the calculation of  $\varepsilon_k$  might not be straightforward, since an

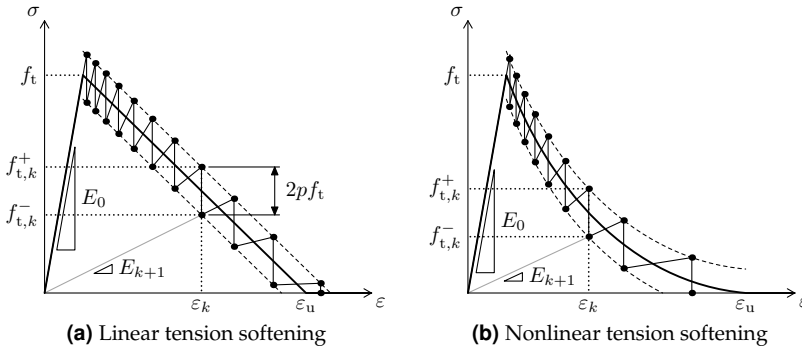


**Figure 3.7** The band width ripple concept is based on a band with a fixed width of  $2pf_t$  centered at the base material law.

explicit formulation for the softening tail may not exist as explained in Section 2.1. The next section will explain how we deal with this problem by using an iterative procedure.

The use of a band centered at the base material law was meant to give fracture energy invariant saw-tooth laws. Rots et al. [59] motivated this statement by considering the triangular areas above and below the base material law. The hatched triangles in Figure 3.8a indicate two of these areas. The left one represents an underestimation of the energy dissipation whereas the right one indicates an overestimation. Through a geometrical argument it can be shown that for linear tension softening these two triangles are equal in size, which means that the overestimation cancels out the underestimation. Since the triangles appear in pairs, it was suggested that in this way fracture energy invariant saw-tooth laws could be obtained, regardless the exact value of the band width  $2pf_t$ . However, a careful consideration reveals that this motivation generally does not hold. First of all, the number of triangles located above the base material law exceeds the number of triangles below the base curve by one. Furthermore, the rightmost area that represents an overestimation needs not necessarily be a triangle. For example, in Figure 3.8a this area is quadrilateral in shape. In addition, for nonlinear base material laws, the areas that represent the underestimations and overestimations are not similar in shape, since one of their sides is curved as shown in Figure 3.8b. Consequently, their areas are not by definition equal in size. Although the error in energy dissipation may be sufficiently small to be acceptable, this cannot be guaranteed without explicitly examining the resulting saw-tooth laws. Therefore, Section 3.2 proposes several improvements to the band width ripple concept to make it fracture energy invariant.

Rots et al. [59] demonstrated that the band width ripple concept can be used to model crushing of concrete or yielding of reinforcement bars as well.

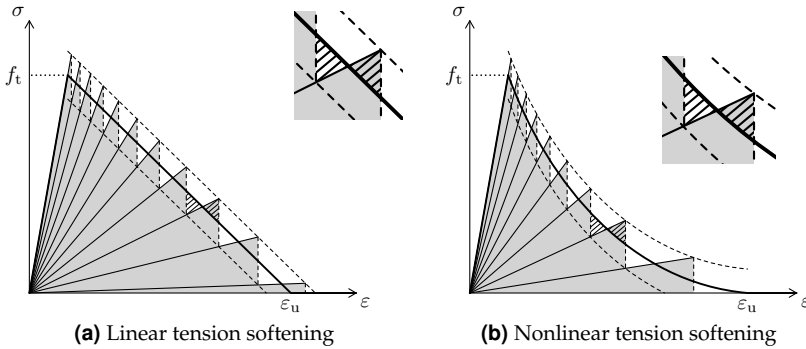


**Figure 3.8** The energy dissipation corresponding to the band width ripple concept is not invariant with respect to the band width  $2pf_t$ .

## 3.2 Improved band width ripple concept

The present section proposes an improved version of the band width ripple concept to ensure invariance of the fracture energy with respect to the number of saw-teeth. The improvement is based on the idea that the vertical shifts of the base material law that define the band, need not necessarily be equal. Figure 3.9 shows that we assume the upper imaginary curve to be shifted over a distance  $p_1 f_t$  whereas the lower imaginary curve is shifted over a distance  $p_2 f_t$ . Moreover, we determine the band width parameters  $p_1$  and  $p_2$  iteratively, given the number of saw-teeth  $N$  and the following two requirements:

1. The area enclosed by the saw-tooth law (which represents the amount of dissipated energy) should be equal to the area enclosed by the base material law.
2. The ultimate strain of the saw-tooth law should be equal to the ultimate strain of the base material law.

Note that the proposed improved concept requires the number of saw-teeth as input and computes the corresponding ripple band width, whereas for the original concept it is the other way around.

Figure 3.10 shows a flowchart of the steps involved in the improved band width ripple concept. It uses a Newton-Raphson procedure to solve for the band width parameters  $p_1$  and  $p_2$ . To improve the robustness of the iterative procedure, Slobbe [70] proposed an alternative approach using a Simplex algorithm.

Step {1} is to make a first estimation of the band width parameters  $p_1$  and  $p_2$ , taking into account the desired number of saw-teeth  $N$ . Subsequently, Steps {2} and {3} set up a stepwise secant material law consisting of  $N$  saw-teeth by using the estimated band in a similar way as the original band width ripple concept.

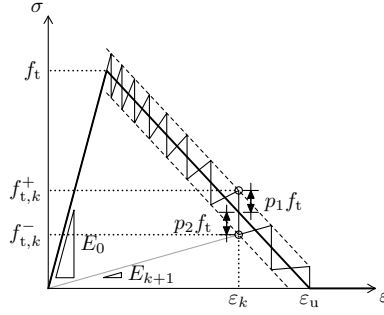


**Figure 3.9** The improved band width ripple concept applied to a linear tension softening law.

One issue that complicates the procedure of setting up the saw-tooth law is how to determine the total strain  $\varepsilon_k$  at the end of secant branch  $k$ . The reason is that no explicit analytical description of the softening tail may exist. The way we solved this issue will be presented later in this section. Step {4} determines the energy dissipation  $(G_f^I/h)^*$  and the ultimate strain  $\varepsilon_u^*$  corresponding to the saw-tooth law. The former equals the area enclosed by the diagram and can be written as

$$\left(\frac{G_f^I}{h}\right)^* = \frac{1}{2}\varepsilon_N p_1 f_t + \sum_{k=1}^{N-1} \frac{1}{2}\varepsilon_k (p_1 + p_2) f_t \quad (3.11)$$

whereas the latter reads

$$\varepsilon_u^* = \varepsilon_N \quad (3.12)$$

Step {5} checks whether the obtained saw-tooth approximation meets the following requirements

$$1 - \frac{G_f^I/h^*}{G_f^I/h} < \varepsilon_{tol} \quad (3.13)$$

$$\left(1 - \frac{\varepsilon_u^*}{\varepsilon_u}\right)^2 + \left(\frac{\sigma_u^*}{f_t}\right)^2 < \varepsilon_{tol} \quad (3.14)$$

with  $\sigma_u^*$  the ultimate stress at the end of the saw-tooth law and  $\varepsilon_{tol}$  a given tolerance (for the results presented in this work we adopted  $\varepsilon_{tol} = 1.0 \times 10^{-10}$ ). If these conditions hold simultaneously, we accept the saw-tooth law. Otherwise, Step {6} updates the estimation of the band width parameters  $p_1$  and  $p_2$  and subsequently a new saw-tooth law is set up.

One issue that needs to be addressed is how to find the intersection of secant branch  $k$  with the imaginary upper curve. Note that this problem originates from the fact that no explicit analytical expression may exist for the softening tail in terms of total strain (see also Section 2.1). Consequently, the issue also applies to the original band width ripple concept. Figure 3.11 shows a flowchart with the

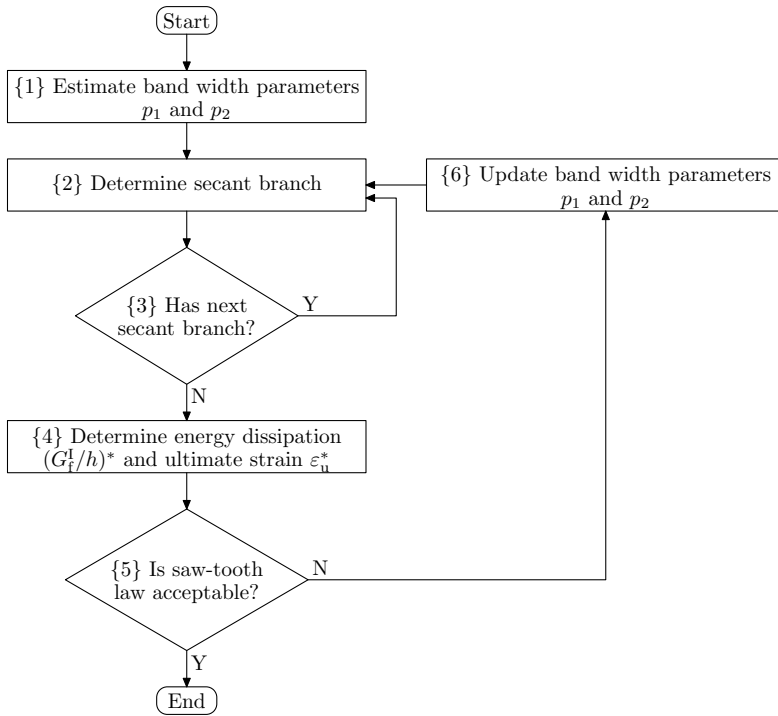


**Figure 3.10** Flowchart of the steps involved in the improved band width ripple concept.

steps that we follow to determine  $\varepsilon_k$ . In Step {2a} we need to estimate the crack strain contribution  $\varepsilon_k^{cr}$  to the total strain  $\varepsilon_k$ . Subsequently, Step {2b} calculates the stress  $\sigma_k$  that is transferred across the crack from the tension softening relation using the estimated value of  $\varepsilon_k^{cr}$ . Also the raised stress limit  $f_{t,k}^+$  needs to be calculated

$$f_{t,k}^+ = \sigma_k + p_1 f_t \quad (3.15)$$

Step {2c} determines the elastic strain component  $\varepsilon_k^{el}$  through Equation (2.24) and the total strain  $\varepsilon_k$  according to Equation (2.23). Next, Step {2d} calculates the raised stress limit  $\underline{f}_{t,k}^+$  based on the secant formulation

$$\underline{f}_{t,k}^+ = E_k \varepsilon_k \quad (3.16)$$

Step {2e} compares the raised stress limits  $f_{t,k}^+$  and  $\underline{f}_{t,k}^+$ . The total strain  $\varepsilon_k$  is accepted in case the difference between these raised stress limits is sufficiently small. If not, Step {2f} updates the estimated crack strain and subsequently the outlined procedure is repeated. Once  $\varepsilon_k$  is known, the reduced stiffness of the next secant branch  $k + 1$  can be calculated from

$$E_{k+1} = \frac{f_{t,k}^+ - \Delta\sigma_k}{\varepsilon_k} \quad (3.17)$$

with

$$\Delta\sigma_k = \begin{cases} (p_1 + p_2) f_t & \text{if } 0 \leq k < N \\ p_1 f_t & \text{if } k = N \end{cases} \quad (3.18)$$

Although the improved band width ripple concept was explained assuming a smeared crack model, it is equally well suited for a discrete crack model. In that case, we need to keep in mind that the initial stiffness  $k_n$  is given a high dummy value (see Section 2.1) and that consequently a relatively large number of saw-teeth may be required to set up a proper saw-tooth law.

Often the computed values of  $p_1$  and  $p_2$  are close. Most case studies and examples presented in Chapters 6 and 7 use the improved band width ripple concept to set up saw-tooth approximations. There we will show some resulting values of  $p_1$  and  $p_2$ .

### 3.3 Snap-back at constitutive level

As mentioned in Section 2.1, for total strain based crack models a snap-back may occur at constitutive level in case of relatively large elements and/or materials with extremely brittle properties. Since classical incremental-iterative schemes cannot cope with these special constitutive relations, a workaround is required to remedy the issue. Possible workarounds include adopting a finer mesh (which reduces the crack band width  $h$ ), lowering the tensile strength  $f_t$  and/or increasing



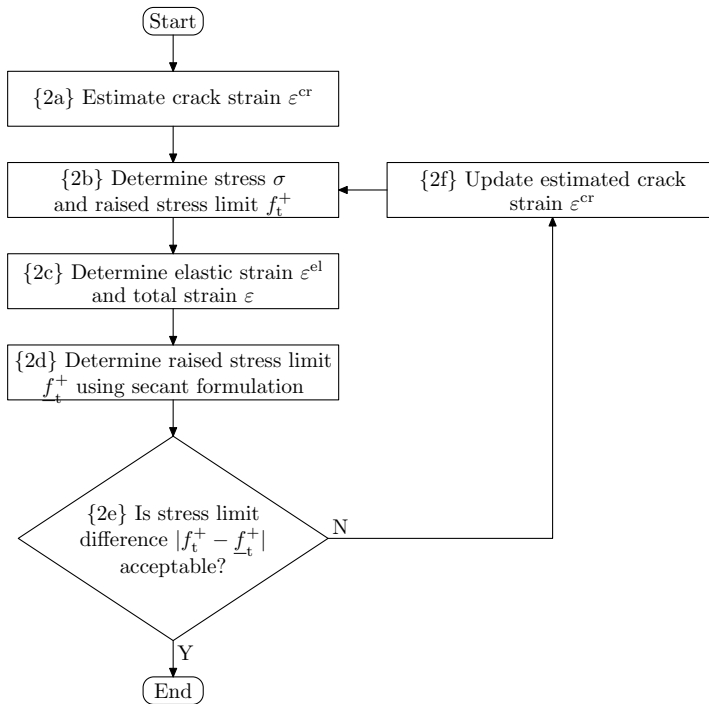


**Figure 3.11** Flowchart of the steps involved in determining a secant branch using the (improved) band width ripple concept.

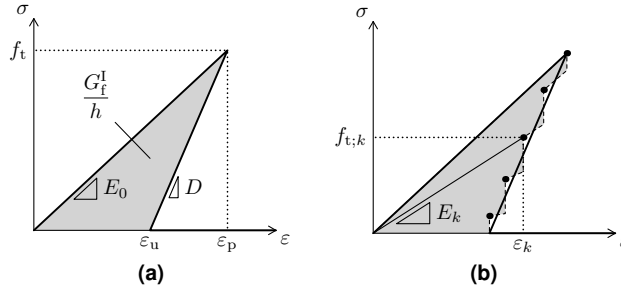


**Figure 3.12** Linear snap-back at constitutive level.

the fracture energy  $G_f^I$ . In contrast, the SLA scheme can cope with a snap-back at constitutive level, since a saw-tooth law may be regarded as a collection of consecutive secant branches. The challenge here is to provide an adequate stepwise secant material law, as the previously presented methods implicitly assume that the softening modulus is negative.

Invernizzi, Trovato, Hendriks, and Van de Graaf [39] introduced an alternative band width ripple concept that is targeted at total strain based formulations exhibiting a linear snap-back (see Figure 3.12a). These constitutive relations are characterized by a total strain  $\varepsilon_p$  at peak stress  $f_t$  which is greater than the ultimate strain  $\varepsilon_u$ . For linear tension softening this can be expressed as

$$\varepsilon_u = \frac{2G_f^I}{h f_t} < \varepsilon_p = \frac{f_t}{E_0} \quad (3.19)$$

Consequently, the softening modulus  $D$  is positive and it can be calculated through

$$D = \frac{f_t}{\varepsilon_p - \varepsilon_u} \quad (3.20)$$

Figure 3.12a illustrates the characterizing material parameters.

One of the issues we had to face was how to define the path that connects two consecutive secant branches. This is important as it is used to determine the energy dissipation corresponding to the saw-tooth law. The commonly adopted assumption of a straight vertical path could not be employed here since for each secant branch  $k$  the corresponding limit strain  $\varepsilon_k$  is smaller than the previous one  $\varepsilon_{k-1}$  due to the snap-back. Therefore, we introduced the kinked path shown in Figure 3.12b.

In essence, the suggested approach is along the lines of the improved band width ripple concept as stipulated in Section 3.2. However, the outlined approach replaces the two band width parameters  $p_1$  and  $p_2$  by a single parameter  $p$ . At the end of this section, we will explain why this simplification works for the case of linear tension softening. Another difference with the previously outlined band

width ripple concept is that for the elastic branch, no stress overshoot is applied, so

$$f_{t,0}^+ = f_t \quad (3.21)$$

The corresponding lowered stress limit  $f_{t,0}^-$  is calculated from

$$f_{t,0}^- = (1 - p)f_t \quad (3.22)$$

Subsequently, the reduced stiffness  $E_1$  of the first secant branch is determined through

$$E_1 = \frac{f_{t,0}^-}{\varepsilon_p} \quad (3.23)$$

Also for the next secant branches explicit analytical expressions exist to define them. Starting from secant branch  $k$  with reduced stiffness  $E_k$  the corresponding ultimate strain  $\varepsilon_k$  is defined by

$$\varepsilon_k = \frac{D\varepsilon_u - pf_t}{D - E_k} \quad (3.24)$$

The corresponding raised stress limit  $f_{t,k}^+$  can be calculated from

$$f_{t,k}^+ = E_k\varepsilon_k \quad (3.25)$$

Subsequently, the reduced stiffness  $E_{k+1}$  of the next secant branch  $k + 1$  is known by subtracting a stress decrement  $\Delta\sigma_k$  from the raised stress limit  $f_{t,k}^+$  while retaining the total strain  $\varepsilon_k$

$$E_{k+1} = \frac{f_{t,k}^+ - \Delta\sigma_k}{\varepsilon_k} \quad (3.26)$$

with

$$\Delta\sigma_k = \begin{cases} 2pf_t & \text{if } 1 \leq k < N \\ pf_t & \text{if } k = N \end{cases} \quad (3.27)$$

As for the improved band width ripple concept, also here the band width parameter  $p$  needs to be determined iteratively given the number of saw-teeth  $N$  (see the flowchart in Figure 3.10).

For the special case of a linear snap-back, from the viewpoint of fracture energy invariance it is sufficient to adopt a single band width parameter  $p$ . The reason is that the triangular areas corresponding to an overestimation and underestimation of the energy dissipation are similar in shape and size. Hence, they cancel out in pairs. Note also that, contrary to the original band width ripple concept, the number of triangular areas above and below the material base law are equal.

We expect that it is not straightforward to extend the presented concept towards more general nonlinear snap-backs. In particular, if the strain along the snap-back does not monotonously decrease new issues are introduced. For example, contrary to what we have seen so far, at some point the shifted curves that define the band will intersect the material base law. Furthermore, it is not obvious how to define the path that connects two consecutive secant branches.

## 3.4 Conclusions

The objective of this chapter was to present a number of methods that can be used to approximate a nonlinear stress–strain relation by a stepwise secant material model. These nonlinear stress–strain laws include strain-softening relations for modeling the behavior of unreinforced concrete, masonry and glass, uniaxial elasto-plastic relations for modeling the behavior of reinforcement bars and bond-slip relations.

First, we discussed three methods from literature: the constant stress decrements method, the constant stiffness reductions method and the band width ripple concept. We explained in which ways the first two methods could be regularized in order to obtain mesh size objective results. And although the band width ripple concept was supposed to not need any regularization procedure, we have shown that the obtained fracture energy dissipation is not invariant with respect to the given ripple band width.

To make the band width ripple concept invariant with respect to the dissipated fracture energy, we have proposed an improved version. The starting point is that the number of saw-teeth is given, not the ripple band width. We determine the ripple band width iteratively by assuming the following two constraints:

1. The obtained energy dissipation should be equal to the energy dissipation of the base material law.
2. The obtained ultimate crack strain or crack width should be equal to the one of the base material law.

As a result, the ripple band width is no longer centered at the softening tail.

To cope with snap-backs at constitutive level, we have developed an alternative band width ripple concept. Such a peculiar constitutive relation is of particular interest for total strain based crack models in case of relatively large elements and/or materials with extremely brittle properties.



# Chapter 4 Stepwise secant Coulomb friction laws

The previous chapter elaborated on methods to set up stepwise secant material laws. Those methods were targeted at material behavior that can be adequately described in terms of a single stress component that only depends on one deformation component. Although this covers a substantial number of material models, including discrete and smeared crack models, bond–slip models and elasto-plastic models, constitutive relations that involve multiple stress and/or deformation components require a more sophisticated approach. For example, structural masonry analysis frequently employs the Coulomb friction law which formulates shear failure in terms of normal and shear stress.

This chapter explains how we include Coulomb friction laws in our sequentially linear analysis (SLA) based simulations. First, Section 4.1 stipulates how to determine the critical load multiplier based on the Coulomb failure criterion assuming proportional loading. The next two sections elaborate on how to account for the arising damage in a stepwise fashion. Section 4.2 proposes an uncoupled formulation, ignoring dilatancy effects, which takes into account cohesion softening. Section 4.3 introduces a more complex coupled formulation based on plasticity theory which accounts for dilatancy effects. Contrary to the uncoupled formulation, we exclude cohesion softening in the coupled formulation. Finally, Section 4.4 combines the Coulomb friction formulation of Section 4.2 with a tension cut-off, thus taking shear failure as well as tensile failure into account.

## 4.1 Critical load multiplier

Since the Coulomb friction criterion defines shear failure in terms of normal and shear traction, the calculation of the critical load multiplier  $\lambda_{\text{crit};i}^{(j)}$  at integration point  $i$  for cycle  $j$  can be expressed as follows. Assuming proportional loading, for each integration point  $i$  the traction vector  $\mathbf{t}_i^{(j)}$  should be scaled to the failure contour by multiplying it with a proper value of  $\lambda_{\text{crit};i}^{(j)}$  as shown in Figure 4.1a. Disregarding cohesion softening, the critical load multiplier  $\lambda_{\text{crit};i}^{(j)}$  can be determined directly from

$$\lambda_{\text{crit};i}^{(j)} = \frac{c}{t_{n,i}^{(j)} \tan \phi + |t_{t,i}^{(j)}|} \quad (4.1)$$

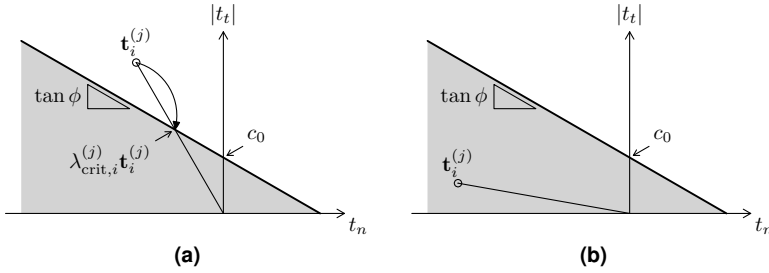


**Figure 4.1** In general, for a Coulomb friction law the critical load multiplier  $\lambda_{\text{crit},i}^{(j)}$  is determined by scaling the traction vector  $\mathbf{t}_i^{(j)}$  to the yield contour (a). However, such scaling is not always possible (b).

with  $c$  the cohesion and  $\tan \phi$  the friction coefficient. However, Figure 4.1b shows that such scaling is not always possible. To be more specific, if the following conditions are met, no critical load multiplier can be determined

$$\frac{|t_{t,i}^{(j)}|}{t_{n,i}^{(j)}} \leq \tan \phi \quad \text{and} \quad t_{n,i}^{(j)} < 0 \quad (4.2)$$

That is, if the above condition is fulfilled, the integration point under consideration will not become critical, regardless the value of  $\lambda_{\text{crit},i}^{(j)}$ . The same holds in case the traction vector is equal to the zero vector.

In case of cohesion softening (e.g. as per Equation (2.31)) we will follow an alternative approach to calculate the critical load multiplier  $\lambda_{\text{crit},i}^{(j)}$ . Here we assume the mobilized cohesion  $c$  — which is a function of the plasticity parameter  $\kappa$  — to be dependent on  $\lambda_{\text{crit},i}^{(j)}$ . Then the critical load multiplier can no longer be determined directly. We have solved this issue by adopting a local Newton-Raphson scheme.

Recall that Equation (4.1) is valid for proportional loading only. In case of non-proportional loading, the expression tends to get more complex, particularly when also cohesion softening needs to be considered.

## 4.2 An uncoupled formulation

The previous section explained how the critical load multiplier  $\lambda_{\text{crit},i}^{(j)}$  at each integration point  $i$  could be determined for the Coulomb friction law assuming proportional loading. In the present section we introduce an uncoupled secant formulation for the Coulomb friction law that reduces the shear stiffness stepwise. Since no coupling terms are present in the adopted constitutive matrix, dilatancy is not

taken into account, i.e.  $\psi = 0$ . As stated in CUR report 171 [14], this assumption gives good results for masonry structures, which will be confirmed by analysis results presented in Section 7.1.

For the time being, we assume that the normal traction  $t_n$  which is transferred across the sliding plane is in compression. Effectively, that means the normal stiffness  $k_n$  does not have to be updated, since the interface will not open up. However, Section 4.4 will show how to combine this uncoupled formulation with a tension cut-off criterion to allow for discrete cracking as well which is important in case of structural masonry analysis.

For the critical integration point, the updated secant stiffness matrix looks as follows

$$\mathbf{D}_{\text{sec}}^{(j+1)} = \begin{bmatrix} k_{n,0} & 0 \\ 0 & k_t^{(j+1)} \end{bmatrix} \quad (4.3)$$

with  $k_{n,0}$  and  $k_t^{(j+1)}$  the initial normal and updated shear stiffness components, respectively. Contrary to the saw-tooth laws discussed in Chapter 3, the stepwise secant Coulomb friction law is not set up in advance. Instead, each shear stiffness reduction is computed at analysis time and it is based on the critical shear traction  $t_{t,\text{crit}}^{(j)}$  and the critical relative shear displacement  $u_{t,\text{crit}}^{(j)}$  of the last cycle  $j$ . That is, for the critical integration point the updated shear stiffness  $k_t^{(j+1)}$  is computed from

$$k_t^{(j+1)} = \frac{t_{t,\text{crit}}^{(j)}}{u_{t,\text{crit}}^{(j)} + \underline{\Delta u}_t^{(j)}} \quad \text{with } \underline{\Delta u}_t^{(j)} = a_t u_{t,\text{crit}}^{(j)} \quad (4.4)$$

where  $\underline{\Delta u}_t^{(j)}$  denotes a *specified* relative displacement increment which we have chosen as a factor  $a_t$  times  $u_{t,\text{crit}}^{(j)}$ . Section 7.1 suggests an appropriate value for  $a_t$ . Figure 4.2 demonstrates the proposed shear stiffness reduction strategy. The updated shear stiffness can thus be interpreted as the secant stiffness which belongs to a specified increased shear displacement  $(1 + a_t)u_{t,\text{crit}}^{(j)}$  and a specified constant normal displacement  $u_n^{(j)}$ .

The introduction of a specified relative displacement increment is just an alternative view on the definition of saw-tooth laws. Figure 4.3 demonstrates this for a uni-axial tension softening relation from Chapter 3. Basically, starting from secant branch  $k$ , the next one can be defined by considering a specified strain increment  $\underline{\Delta \varepsilon}_k$  and the corresponding stress decrement  $\Delta \sigma_k$

$$E_{k+1} = \frac{\sigma_{k+1}}{\varepsilon_{k+1}} = \frac{\sigma_k + \Delta \sigma_k}{\varepsilon_k + \underline{\Delta \varepsilon}_k} \quad (4.5)$$

where the stress decrement  $\Delta \sigma_k$  is determined through the tangent stiffness (here the softening modulus  $D$ ). Note that we underline specified quantities. Also note that the updated secant stiffness is exact only for a specified strain increment of  $\underline{\Delta \varepsilon}_k$ . In all other cases, we assume it gives a reasonable approximation.



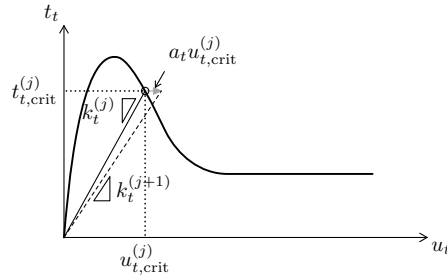


**Figure 4.2** For the uncoupled formulation, the reduced shear stiffness  $k_t^{(j+1)}$  is computed from the relative shear displacement  $u_{t,crit}^{(j)}$ , a given magnification factor  $a_t$  and the shear traction  $t_{t,crit}^{(j)}$ . The bold line indicates the  $t_t$ - $u_t$  relation for a monotonically increasing  $u_t$  and a constant  $u_n$ .

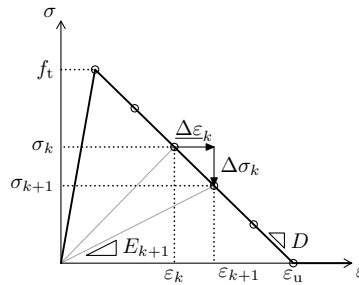


**Figure 4.3** Alternative way to define a saw-tooth law for a uniaxial tension softening relation through a specified strain increment  $\Delta\epsilon_k$  and the corresponding stress decrement  $\Delta\sigma_k$ .

Another difference with the earlier discussed saw-tooth laws is that the strength properties (here the mobilized cohesion  $c$  and the friction angle  $\phi$ ) are not reduced stepwise like the shear stiffness. Instead, the mobilized cohesion is computed while the analysis progresses, whereas the friction angle is assumed constant.

### 4.3 A coupled formulation

The previous section presented an uncoupled formulation of the reduced secant stiffness matrix  $\mathbf{D}_{\text{sec}}^{(j+1)}$ . The relatively simple formulation generally makes it the preferred approach for cases where dilatancy is less relevant. However, especially for cases where the coupling terms are relevant (i.e. dilatancy) the proposed formulation is inadequate. Therefore, this section introduces a coupled formulation of  $\mathbf{D}_{\text{sec}}^{(j+1)}$  for a two-dimensional model which is derived from the tangent stiffness matrix  $\mathbf{D}_{\text{tan}}^{(j)}$  and a set of specified relative displacement increments.

Adopting the view on saw-tooth laws as outlined in the previous section we can define a secant stiffness matrix for the Coulomb friction law with the advantage that coupling terms can be taken into account. Since  $\mathbf{D}_{\text{sec}}^{(j+1)}$  has four unknown components, we need four equations to solve for them. Starting from two specified relative displacement increment vectors  $\underline{\Delta \mathbf{u}}_{\text{I}}^{(j)}$  and  $\underline{\Delta \mathbf{u}}_{\text{II}}^{(j)}$  the corresponding traction increment vectors  $\underline{\Delta \mathbf{t}}_{\text{I}}^{(j)}$  and  $\underline{\Delta \mathbf{t}}_{\text{II}}^{(j)}$  can be calculated through

$$\underline{\Delta \mathbf{t}}_{\text{I}}^{(j)} = \mathbf{D}_{\text{tan}}^{(j)} \underline{\Delta \mathbf{u}}_{\text{I}}^{(j)} \quad (4.6a)$$

$$\underline{\Delta \mathbf{t}}_{\text{II}}^{(j)} = \mathbf{D}_{\text{tan}}^{(j)} \underline{\Delta \mathbf{u}}_{\text{II}}^{(j)} \quad (4.6b)$$

with  $\mathbf{D}_{\text{tan}}^{(j)}$  the tangent stiffness matrix from Equation (2.33) which is repeated here for convenience

$$\mathbf{D}_{\text{tan}}^{(j)} = \frac{1}{k_{n,0} \tan \phi \tan \psi + k_{t,0}} \begin{bmatrix} k_{n,0} k_{t,0} & -k_{n,0} k_{t,0} \tan \psi \frac{t_{t,\text{crit}}^{(j)}}{|t_{t,\text{crit}}^{(j)}|} \\ -k_{n,0} k_{t,0} \tan \phi \frac{t_{t,\text{crit}}^{(j)}}{|t_{t,\text{crit}}^{(j)}|} & k_{n,0} k_{t,0} \tan \phi \tan \psi \end{bmatrix} \quad (4.7)$$

Here  $k_{n,0}$  and  $k_{t,0}$  denote the initial normal and shear stiffness, respectively,  $\tan \phi$  is the friction coefficient and  $\tan \psi$  denotes the dilatancy coefficient. Subsequently, we determine the total relative displacement vectors for step  $j + 1$

$$\mathbf{u}_{\text{I}}^{(j+1)} = \mathbf{u}_{\text{crit}}^{(j)} + \underline{\Delta \mathbf{u}}_{\text{I}}^{(j)} \quad (4.8a)$$

$$\mathbf{u}_{\text{II}}^{(j+1)} = \mathbf{u}_{\text{crit}}^{(j)} + \underline{\Delta \mathbf{u}}_{\text{II}}^{(j)} \quad (4.8b)$$

with  $\mathbf{u}_{\text{crit}}^{(j)}$  the scaled total relative displacement vector at the end of step  $j$ . In a similar way we can determine the traction vectors in step  $j + 1$

$$\mathbf{t}_{\text{I}}^{(j+1)} = \mathbf{t}_{\text{crit}}^{(j)} + \underline{\Delta \mathbf{t}}_{\text{I}}^{(j)} \quad (4.9a)$$

$$\mathbf{t}_{\text{II}}^{(j+1)} = \mathbf{t}_{\text{crit}}^{(j)} + \underline{\Delta \mathbf{t}}_{\text{II}}^{(j)} \quad (4.9b)$$

with  $\mathbf{t}_{\text{crit}}^{(j)}$  the scaled traction vector at the end of step  $j$ . Finally, we should relate the total traction vectors of step  $j + 1$  to the corresponding total relative displacement vectors through the secant stiffness matrix  $\mathbf{D}_{\text{sec}}^{(j)}$

$$\mathbf{t}_{\text{I}}^{(j+1)} = \mathbf{D}_{\text{sec}}^{(j+1)} \mathbf{u}_{\text{I}}^{(j+1)} \quad (4.10a)$$

$$\mathbf{t}_{\text{II}}^{(j+1)} = \mathbf{D}_{\text{sec}}^{(j+1)} \mathbf{u}_{\text{II}}^{(j+1)} \quad (4.10b)$$

Note that the obtained secant stiffness matrix  $D_{\text{sec}}^{(j+1)}$  yields exact results for  $\underline{\Delta \mathbf{u}}_{\text{I}}^{(j)}$  and  $\underline{\Delta \mathbf{u}}_{\text{II}}^{(j)}$  only. For any other relative displacement increment vector we assume that the obtained matrix is a reasonable approximation.

We propose that the considered sets of specified relative displacement increment vectors  $\underline{\Delta \mathbf{u}}_{\text{I}}^{(j)}$  and  $\underline{\Delta \mathbf{u}}_{\text{II}}^{(j)}$  depend on the actual stress situation after scaling. We distinguish the following three cases:

1. A positive shear traction  $t_{t,\text{crit}}^{(j)}$ .
2. A negative shear traction  $t_{t,\text{crit}}^{(j)}$ .
3. Zero shear traction  $t_{t,\text{crit}}^{(j)}$ .

These will be elaborated in the remainder of this section.

**Positive shear traction** In case the scaled shear stress  $t_{t,\text{crit}}^{(j)}$  is positive, it was scaled to the indicated yield line in Figure 4.4a. We consider the following vectors of specified relative displacement increments

$$\underline{\Delta \mathbf{u}}_{\text{I}}^{(j)} = \begin{bmatrix} a_n \\ 0 \end{bmatrix} \quad \text{with } a_n > 0 \quad (4.11)$$

and

$$\underline{\Delta \mathbf{u}}_{\text{II}}^{(j)} = \begin{bmatrix} 0 \\ a_t \end{bmatrix} \quad \text{with } a_t > 0 \quad (4.12)$$

Thus we respectively consider a displacement increment in the “opening” direction without shear displacement, and a displacement increment in pure shear which increases the shear that is already there. The two specified displacement increments thus address the main causes for the Coulomb friction law to become plastic.

Next, we substitute these vectors into the set of equations (4.6) to obtain the traction increment vectors  $\Delta \mathbf{t}_{\text{I}}^{(j)}$  and  $\Delta \mathbf{t}_{\text{II}}^{(j)}$ . Subsequently, we determine the total traction vectors  $\mathbf{t}_{\text{I}}^{(j)}$  and  $\mathbf{t}_{\text{II}}^{(j)}$  through the set of equations (4.9) and the total relative displacement vectors  $\mathbf{u}_{\text{I}}^{(j)}$  and  $\mathbf{u}_{\text{II}}^{(j)}$  through the set of equations (4.8). Then by

substituting the resulting total vectors into the set of equations (4.10), we obtain the following system of equations

$$\begin{aligned}
 & \begin{bmatrix} t_{n,\text{crit}}^{(j)} + \frac{k_{n,0}k_{t,0}a_n}{k_{n,0} \tan \phi \tan \psi + k_{t,0}} \\ t_{t,\text{crit}}^{(j)} - \frac{k_{n,0}k_{t,0} \tan \phi a_n}{k_{n,0} \tan \phi \tan \psi + k_{t,0}} \\ t_{n,\text{crit}}^{(j)} - \frac{k_{n,0}k_{t,0} \tan \psi a_t}{k_{n,0} \tan \phi \tan \psi + k_{t,0}} \\ t_{t,\text{crit}}^{(j)} + \frac{k_{n,0}k_{t,0} \tan \phi \tan \psi a_t}{k_{n,0} \tan \phi \tan \psi + k_{t,0}} \end{bmatrix} \\
 &= \begin{bmatrix} u_{n,\text{crit}}^{(j)} + a_n & u_{t,\text{crit}}^{(j)} & 0 & 0 \\ 0 & 0 & u_{n,\text{crit}}^{(j)} + a_n & u_{t,\text{crit}}^{(j)} \\ u_{n,\text{crit}}^{(j)} & u_{t,\text{crit}}^{(j)} + a_t & 0 & 0 \\ 0 & 0 & u_{n,\text{crit}}^{(j)} & u_{t,\text{crit}}^{(j)} + a_t \end{bmatrix} \begin{bmatrix} D_{11,\text{sec}}^{(j+1)} \\ D_{12,\text{sec}}^{(j+1)} \\ D_{21,\text{sec}}^{(j+1)} \\ D_{22,\text{sec}}^{(j+1)} \end{bmatrix} \quad (4.13)
 \end{aligned}$$

The solution reads

$$D_{11,\text{sec}}^{(j+1)} = \frac{k_{n,0}a_t \tan \psi (t_{n,\text{crit}}^{(j)} \tan \phi + u_{t,\text{crit}}^{(j)} k_{t,0}) + k_{n,0}k_{t,0}a_n (u_{n,\text{crit}}^{(j)} + a_t) + t_{n,\text{crit}}^{(j)} a_t k_{t,0}}{(k_{n,0} \tan \phi \tan \psi + k_{t,0})(u_{n,\text{crit}}^{(j)} a_t + u_{t,\text{crit}}^{(j)} a_n + a_n a_t)} \quad (4.14a)$$

$$D_{12,\text{sec}}^{(j+1)} = \frac{-k_{n,0}k_{t,0} \tan \psi a_t (u_{n,\text{crit}}^{(j)} + a_n) + k_{n,0}a_n (t_{n,\text{crit}}^{(j)} \tan \phi \tan \psi - k_{t,0}u_{n,\text{crit}}^{(j)}) + a_n t_{n,\text{crit}}^{(j)} k_{t,0}}{(k_{n,0} \tan \phi \tan \psi + k_{t,0})(u_{n,\text{crit}}^{(j)} a_t + u_{t,\text{crit}}^{(j)} a_n + a_n a_t)} \quad (4.14b)$$

$$D_{21,\text{sec}}^{(j+1)} = \frac{-k_{n,0}k_{t,0} \tan \phi a_n (u_{t,\text{crit}}^{(j)} + a_t) + k_{n,0} \tan \phi \tan \psi a_t (t_{t,\text{crit}}^{(j)} - k_{t,0}u_{t,\text{crit}}^{(j)}) + a_t t_{t,\text{crit}}^{(j)} k_{t,0}}{(k_{n,0} \tan \phi \tan \psi + k_{t,0})(u_{n,\text{crit}}^{(j)} a_t + u_{t,\text{crit}}^{(j)} a_n + a_n a_t)} \quad (4.14c)$$

$$D_{22,\text{sec}}^{(j+1)} = \frac{k_{n,0} \tan \phi \tan \psi (t_{t,\text{crit}}^{(j)} a_n + a_t k_{t,0} (u_{n,\text{crit}}^{(j)} + a_t)) + k_{t,0} a_n (k_{n,0} \tan \phi u_{n,\text{crit}}^{(j)} + t_{t,\text{crit}}^{(j)})}{(k_{n,0} \tan \phi \tan \psi + k_{t,0})(u_{n,\text{crit}}^{(j)} a_t + u_{t,\text{crit}}^{(j)} a_n + a_n a_t)} \quad (4.14d)$$

Recall that the above solution of  $\mathbf{D}_{\text{sec}}^{(j+1)}$  is exact if and only if the specified relative displacement increment vector  $\underline{\Delta \mathbf{u}}^{(j)}$  equals either  $(a_n, 0)$  or  $(0, a_t)$ .

**Negative shear traction** In case the scaled shear traction  $t_{t,\text{crit}}^{(j)}$  is negative, it was scaled to the indicated yield line in Figure 4.4b. Now we consider the following specified relative displacement increment vectors

$$\underline{\Delta \mathbf{u}}_{\text{I}}^{(j)} = \begin{bmatrix} a_n \\ 0 \end{bmatrix} \quad \text{with } a_n > 0 \quad (4.15)$$

and

$$\underline{\Delta \mathbf{u}}_{\text{II}}^{(j)} = \begin{bmatrix} 0 \\ -a_t \end{bmatrix} \quad \text{with } a_t > 0 \quad (4.16)$$

Similar to the case of positive shear traction, the second specified displacement increment increases the shear displacement in absolute sense. We can obtain a

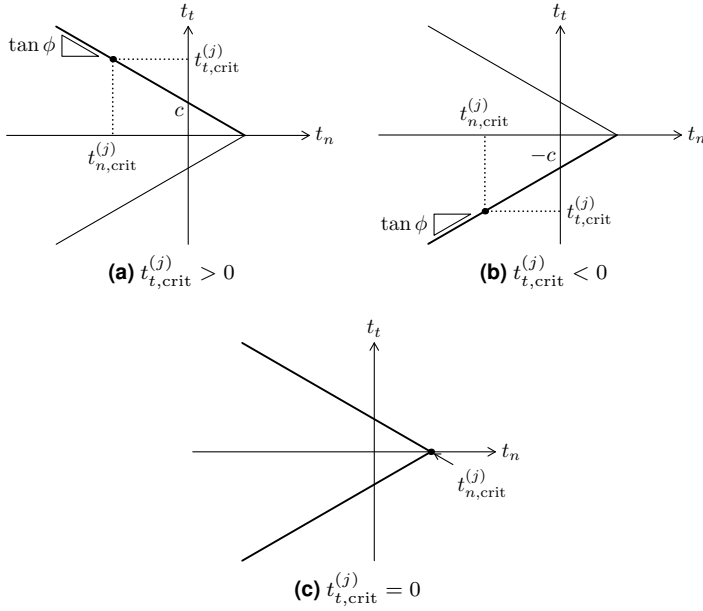


**Figure 4.4** We considered three cases for the derivation of the secant stiffness matrix  $\mathbf{D}_{\text{sec}}^{(j+1)}$ .

system of linear equations for the unknown components of  $\mathbf{D}_{\text{sec}}^{(j+1)}$  in a similar way as described before:

$$\begin{aligned}
 & \begin{bmatrix} t_{n,\text{crit}}^{(j)} + \frac{k_{n,0}k_{t,0}a_n}{k_{n,0}\tan\phi\tan\psi+k_{t,0}} \\ t_{t,\text{crit}}^{(j)} + \frac{k_{n,0}k_{t,0}\tan\phi a_n}{k_{n,0}\tan\phi\tan\psi+k_{t,0}} \\ t_{n,\text{crit}}^{(j)} - \frac{k_{n,0}k_{t,0}\tan\psi a_t}{k_{n,0}\tan\phi\tan\psi+k_{t,0}} \\ t_{t,\text{crit}}^{(j)} - \frac{k_{n,0}k_{t,0}\tan\phi\tan\psi a_t}{k_{n,0}\tan\phi\tan\psi+k_{t,0}} \end{bmatrix} \\
 &= \begin{bmatrix} u_{n,\text{crit}}^{(j)} + a_n & u_{t,\text{crit}}^{(j)} & 0 & 0 \\ 0 & 0 & u_{n,\text{crit}}^{(j)} + a_n & u_{t,\text{crit}}^{(j)} \\ u_{n,\text{crit}}^{(j)} & u_{t,\text{crit}}^{(j)} - a_t & 0 & 0 \\ 0 & 0 & u_{n,\text{crit}}^{(j)} & u_{t,\text{crit}}^{(j)} - a_t \end{bmatrix} \begin{bmatrix} D_{11,\text{sec}}^{(j+1)} \\ D_{12,\text{sec}}^{(j+1)} \\ D_{21,\text{sec}}^{(j+1)} \\ D_{22,\text{sec}}^{(j+1)} \end{bmatrix} \quad (4.17)
 \end{aligned}$$

The secant stiffness matrix that satisfies the above equations has the following components

$$D_{11,\text{sec}}^{(j+1)} = \frac{k_{n,0}a_t \tan \psi (t_{n,\text{crit}}^{(j)} \tan \phi - u_{t,\text{crit}}^{(j)} k_{t,0}) - k_{n,0}k_{t,0}a_n(u_{t,\text{crit}}^{(j)} - a_t) + t_{n,\text{crit}}^{(j)} a_t k_{t,0}}{(k_{n,0} \tan \phi \tan \psi + k_{t,0})(u_{n,\text{crit}}^{(j)} a_t - u_{t,\text{crit}}^{(j)} a_n + a_n a_t)} \quad (4.18a)$$

$$D_{12,\text{sec}}^{(j+1)} = \frac{k_{n,0}k_{t,0} \tan \psi a_t (u_{n,\text{crit}}^{(j)} + a_n) - k_{n,0}a_n (t_{n,\text{crit}}^{(j)} \tan \phi \tan \psi - k_{t,0}u_{n,\text{crit}}^{(j)}) - a_n t_{n,\text{crit}}^{(j)} k_{t,0}}{(k_{n,0} \tan \phi \tan \psi + k_{t,0})(u_{n,\text{crit}}^{(j)} a_t - u_{t,\text{crit}}^{(j)} a_n + a_n a_t)} \quad (4.18b)$$

$$D_{21,\text{sec}}^{(j+1)} = \frac{-k_{n,0}k_{t,0} \tan \phi a_n (u_{t,\text{crit}}^{(j)} - a_t) + k_{n,0} \tan \phi \tan \psi a_t (t_{t,\text{crit}}^{(j)} - k_{t,0}u_{t,\text{crit}}^{(j)}) + a_t t_{t,\text{crit}}^{(j)} k_{t,0}}{(k_{n,0} \tan \phi \tan \psi + k_{t,0})(u_{n,\text{crit}}^{(j)} a_t - u_{t,\text{crit}}^{(j)} a_n + a_n a_t)} \quad (4.18c)$$

$$D_{22,\text{sec}}^{(j+1)} = \frac{k_{n,0} \tan \phi \tan \psi (-t_{t,\text{crit}}^{(j)} a_n + a_t k_{t,0}(u_{n,\text{crit}}^{(j)} + a_n)) + k_{t,0}a_n (k_{n,0} \tan \phi u_{n,\text{crit}}^{(j)} - t_{t,\text{crit}}^{(j)})}{(k_{n,0} \tan \phi \tan \psi + k_{t,0})(u_{n,\text{crit}}^{(j)} a_t - u_{t,\text{crit}}^{(j)} a_n + a_n a_t)} \quad (4.18d)$$

**Zero shear traction** In case the scaled shear traction  $t_{t,\text{crit}}^{(j)}$  equals zero, it was scaled to the apex as shown in Figure 4.4c. For that special case, we consider the following specified relative displacement increment vectors

$$\underline{\Delta \mathbf{u}}_{\text{I}}^{(j)} = \begin{bmatrix} a_n \\ a_t \end{bmatrix} \quad \text{with } a_n, a_t > 0 \quad (4.19)$$

and

$$\underline{\Delta \mathbf{u}}_{\text{II}}^{(j)} = \begin{bmatrix} a_n \\ -a_t \end{bmatrix} \quad \text{with } a_n, a_t > 0 \quad (4.20)$$

We follow the same approach as outlined before to set up a system of linear equations for the components of  $\mathbf{D}_{\text{sec}}^{(j+1)}$

$$\begin{bmatrix} t_{n,\text{crit}}^{(j)} + \frac{k_{n,0}k_{t,0}(a_n - a_t \tan \psi)}{k_{n,0} \tan \phi \tan \psi + k_{t,0}} \\ t_{t,\text{crit}}^{(j)} + \frac{k_{n,0}k_{t,0} \tan \phi (a_t \tan \psi - a_n)}{k_{n,0} \tan \phi \tan \psi + k_{t,0}} \\ t_{n,\text{crit}}^{(j)} + \frac{k_{n,0}k_{t,0}(a_n - a_t \tan \psi)}{k_{n,0} \tan \phi \tan \psi + k_{t,0}} \\ t_{t,\text{crit}}^{(j)} + \frac{k_{n,0}k_{t,0} \tan \phi (a_n - a_t \tan \psi)}{k_{n,0} \tan \phi \tan \psi + k_{t,0}} \end{bmatrix} = \begin{bmatrix} u_{n,\text{crit}}^{(j)} + a_n & u_{t,\text{crit}}^{(j)} + a_t & 0 & 0 \\ 0 & 0 & u_{n,\text{crit}}^{(j)} + a_n & u_{t,\text{crit}}^{(j)} + a_t \\ u_{n,\text{crit}}^{(j)} + a_n & u_{t,\text{crit}}^{(j)} - a_t & 0 & 0 \\ 0 & 0 & u_{n,\text{crit}}^{(j)} + a_n & u_{t,\text{crit}}^{(j)} - a_t \end{bmatrix} \begin{bmatrix} D_{11,\text{sec}}^{(j+1)} \\ D_{12,\text{sec}}^{(j+1)} \\ D_{21,\text{sec}}^{(j+1)} \\ D_{22,\text{sec}}^{(j+1)} \end{bmatrix} \quad (4.21)$$

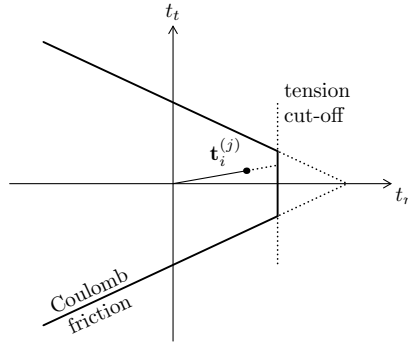


**Figure 4.5** Tension–shear failure criterion for interface elements which consists of a tension cut-off and a Coulomb failure contour.

which has the following solution

$$D_{11,\text{sec}}^{(j+1)} = \frac{k_{n,0}k_{t,0}(a_n - a_t \tan \psi) + t_{n,\text{crit}}^{(j)}(k_{t,0} + k_{n,0} \tan \phi \tan \psi)}{(u_{n,\text{crit}}^{(j)} + a_n)(k_{t,0} + k_{n,0} \tan \phi \tan \psi)} \quad (4.22a)$$

$$D_{12,\text{sec}}^{(j+1)} = 0 \quad (4.22b)$$

$$D_{21,\text{sec}}^{(j+1)} = \frac{k_{n,0}k_{t,0}u_{t,\text{crit}}^{(j)} \tan \phi (a_n - a_t \tan \psi) + t_{t,\text{crit}}^{(j)} a_t (k_{t,0} + k_{n,0} \tan \phi \tan \psi)}{(k_{n,0} \tan \phi \tan \psi + k_{t,0})(u_{n,\text{crit}}^{(j)} + a_n) a_t} \quad (4.22c)$$

$$D_{22,\text{sec}}^{(j+1)} = -\frac{k_{n,0}k_{t,0} \tan \phi (a_n - a_t \tan \psi)}{a_t (k_{n,0} \tan \phi \tan \psi + k_{t,0})} \quad (4.22d)$$

We have found that for this particular case, the ratio between  $a_n$  and  $a_t$  is important. Appendix A shows that when  $a_n/a_t > \tan \psi$  the relative normal displacement  $u_n$  tends to grow towards a certain limit. Therefore, we advise to choose  $a_n$  and  $a_t$  such that  $a_n/a_t \leq \tan \psi$ .

## 4.4 Tension–shear failure criterion

This section extends the Coulomb friction model with a tension cut-off criterion resulting in a tension–shear failure criterion. Such a model is useful in, for example, structural masonry analysis, where joints may be subjected to a combination of shear and tension. Figure 4.5 shows the joined contour of the model. The formulation of the tension cut-off follows the one of the discrete crack model (see Subsection 2.1.1). For the Coulomb friction part of the model, we assume the uncoupled formulation of Section 4.2.

To determine the critical load multiplier  $\lambda_{\text{crit},i}^{(j)}$  of integration point  $i$  at step  $j$  we start by determining the individual load multipliers  $\lambda_{t,i}^{(j)}$  and  $\lambda_{C,i}^{(j)}$  of the tension

cut-off and Coulomb friction criterion, respectively. For the tension cut-off criterion, we only need to calculate the corresponding load multiplier  $\lambda_{t,i}^{(j)}$  if the normal traction  $t_{n,i}^{(j)}$  is positive. In that case, we calculate it as follows

$$\lambda_{t,i}^{(j)} = \frac{f_{t,i}^{(j)}}{t_{n,i}^{(j)}} \quad \text{assuming } t_{n,i}^{(j)} > 0 \quad (4.23)$$

Like for the discrete crack model we only take the normal traction  $t_{n,i}^{(j)}$  into account thus disregarding the effect of the shear traction  $t_{t,i}^{(j)}$  on crack initiation and propagation. For the Coulomb friction criterion we calculate the critical load multiplier  $\lambda_{C,i}^{(j)}$  as stipulated in Section 4.1.

Once we have determined  $\lambda_{t,i}^{(j)}$  and  $\lambda_{C,i}^{(j)}$ , the selection of the actual critical load multiplier  $\lambda_{\text{crit},i}^{(j)}$  depends on the situation. If neither load multiplier yields a finite value then also  $\lambda_{\text{crit},i}^{(j)}$  has no finite value and consequently the integration point under consideration cannot become critical. When only one of the two load multipliers yields a finite value, it automatically becomes the critical load multiplier. If both load multipliers are finite we select the minimum value as the critical one.

How to update the secant constitutive matrix  $\mathbf{D}_{\text{sec}}^{(j+1)}$  depends on the governing failure criterion of the critical integration point. If the tension cut-off criterion was found to yield the critical load multiplier  $\lambda_{\text{crit}}^{(j)}$  then the normal stiffness  $k_n^{(j+1)}$  as well as the shear stiffness  $k_t^{(j+1)}$  of the critical integration point are updated. The normal stiffness is reduced according to the applicable saw-tooth law whereas the shear stiffness is reduced at the same rate as the normal stiffness, i.e.

$$k_t^{(j+1)} = k_{t,0} \frac{k_n^{(j+1)}}{k_{n,0}} \quad (4.24)$$

The exception to this rule is when the current shear stiffness  $k_t^{(j)}$  is already smaller than the updated shear stiffness  $k_t^{(j+1)}$  of Equation (4.24). In that case, the shear stiffness is not updated. When the Coulomb friction criterion was found governing, the shear stiffness  $k_t$  is updated according to Equation (4.4), whereas the normal stiffness is not updated.

## 4.5 Conclusions

This chapter described how the Coulomb friction model can be incorporated in an SLA-based simulation. We have addressed the following issues:

1. How to find the critical load multiplier of the current cycle assuming proportional loading?



## 2. How to update the secant stiffness matrix of the critical integration point?

To determine the critical load multiplier of the current cycle at some integration point, we scale the traction vector resulting from the unit loads to the Coulomb failure contour. We achieved this by following a set of rules which identify positive load multipliers only, if any, in a direct way. An iterative procedure is adopted when cohesion softening is included in the formulation since in that case the failure contour is shifted depending on the amount of plastic shear deformation.

To update the constitutive matrix of the critical integration point we proposed two different stepwise secant approximations of the material model. Contrary to the saw-tooth laws discussed in Chapter 3, the stepwise secant Coulomb friction law is not set up in advance but while the analysis progresses. The first approximation is a relatively simple non-dilatant model which only updates the secant shear stiffness upon progressive shearing using a specified relative shear displacement increment. We assume this increment to be a given fraction of the scaled relative shear displacement. The second approximation updates all components of the secant stiffness matrix which is determined from the tangential stiffness matrix and a given set of specified relative displacement increments. We assume these increments to be constant throughout the analysis. Besides a rigorous basis, the second approximation offers the possibility to include dilatancy.

Finally, we proposed a tension–shear failure criterion that consists of a tension cut-off and a Coulomb failure contour. In essence, the proposed criterion is a combination of the discrete crack model and the uncoupled formulation of the Coulomb friction model that we developed earlier. That implies that for both failure criteria we have to determine the critical load multiplier and then take the minimum of those two multipliers as the governing one. The update of the constitutive matrix of the critical integration point depends on the governing failure criterion. If the traction vector is scaled to the tension cut-off then the normal and shear stiffness components are updated. In case of friction failure we only update the shear stiffness component.

# Chapter 5 Non-proportional loading strategies

The previous two chapters presented techniques to set up stepwise secant approximations of material behavior and Coulomb friction. As pointed out in Section 2.5 another issue that needs to be addressed in order to broaden the application field of sequentially linear analysis (SLA) is non-proportional loading.

This chapter discusses strategies to deal with non-proportional loading for SLA and what difficulties may arise. Section 5.1 introduces non-proportional loading in a general way and it outlines which particular case is considered in this thesis. Subsequently, Section 5.2 reviews and discusses three approaches from the literature. As a basis for further discussion, Section 5.3 reformulates the non-proportional loading problem as a constrained maximization. Finally, Section 5.4 presents a newly developed strategy to cope with a conceptual difficulty associated with SLA under non-proportional loading.

Chapters 6 and 7 aim at the verification and validation of the newly developed techniques and strategies presented in this chapter and the previous two.

## 5.1 Introduction

In all previous chapters we assumed proportional loading which means that all loads increase and decrease simultaneously at the same rate. This implies that proportional linear relationships exist between the applied loads. The straight line in Figure 5.1a illustrates this for the case of two load cases. In this work we use the term *load case* to denote a collection of one or more loads. A *load* is understood to mean a single load, e.g. a point load, a line load, or a prescribed displacement at some node.

In order to analyze real-life structures we often have to deal with load cases that are not applied proportionally. By definition, we will call that *non-proportional loading*. For example, imagine a bridge or viaduct that is initially loaded by self-weight and subsequently by traffic loads as well. The curved line in Figure 5.1a illustrates in a more general way the case of non-proportional loading assuming two load cases.

In the present work we assume a specific kind of non-proportional loading involving two load cases. First, an initial load case  $\mathbf{F}_{\text{ini}}$  is applied followed by a

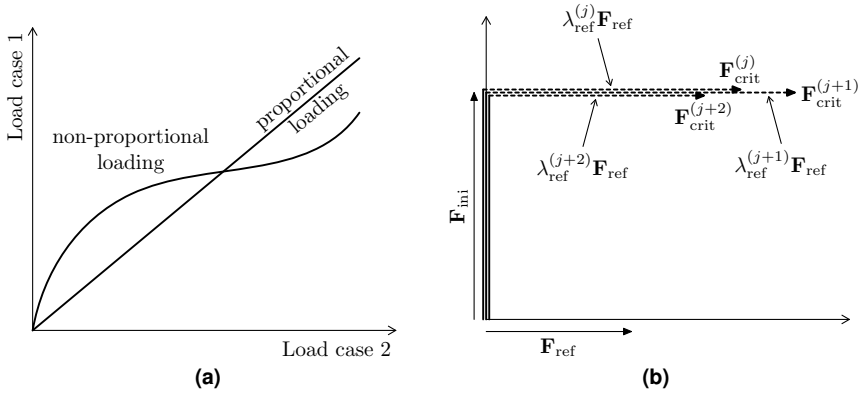


**Figure 5.1** General definition of proportional and non-proportional loading assuming two load cases (a). The non-proportional loading situation considered in this work consists of an initial load case  $\mathbf{F}_{\text{ini}}$  and a reference load case  $\mathbf{F}_{\text{ref}}$  (b).

scaled reference load case  $\lambda_{\text{ref}}^{(j)} \mathbf{F}_{\text{ref}}$ . If we assume that the application of  $\mathbf{F}_{\text{ini}}$  does not induce any damage it means that for each linear analysis (or cycle)  $j$  we reload the model by a combination of the initial and reference load case. The resulting critical load combination  $\mathbf{F}_{\text{crit}}^{(j)}$  can be denoted symbolically as

$$\mathbf{F}_{\text{crit}}^{(j)} = \lambda_{\text{ini}} \mathbf{F}_{\text{ini}} + \lambda_{\text{ref}}^{(j)} \mathbf{F}_{\text{ref}} \quad \text{with } \lambda_{\text{ini}} = 1 \quad (5.1)$$

with  $\lambda_{\text{ref}}^{(j)}$  the critical load multiplier of cycle  $j$  that leads to the next event. The initial load case  $\mathbf{F}_{\text{ini}}$  comprises all loads that are present from the start of the analysis. Examples of initial loads include self-weight and prestressing forces. All entities related to this load case are denoted by the subscript “ini”. The reference load case  $\mathbf{F}_{\text{ref}}$  (subscript “ref”) consists of all loads which are scaled in a stepwise fashion up to failure of the structure and beyond. Figure 5.1b shows that similar to the case of proportional loading the scaling of the reference load case varies from step to step for non-proportional loading.

In case of proportional loading it was evident how to determine the critical value of the global load multiplier, namely the smallest  $\lambda_{\text{crit},i}^{(j)}$  of all integration points. However, this concept cannot be applied one-to-one to non-proportional loading. In Section 5.3 we will address this issue in detail and show that critical values defined in this sense for  $\lambda_{\text{ref}}$  may not exist.

## 5.2 Literature review and discussion

This section discusses three strategies for SLA under non-proportional loading from the literature. Firstly, we will revisit the strategy proposed by DeJong et al. [16].

Their work inspired the development of the constrained maximization analogy (Section 5.3). Subsequently, we will briefly discuss an alternative approach [4] that adapts the material strength to compensate for the initial loads. In that way, only the reference loads need to be considered which effectively reduces the problem to proportional loading. Finally, we will review strategies based on stress redistributions while maintaining the applied external loads [19, 18].

### 5.2.1 Strategy developed by DeJong et al.

The strategy proposed by DeJong et al. [16] is based on stress superposition and they worked it out for a smeared crack model assuming plane stress conditions. For each cycle  $j$  of the simulation they determine at each integration point  $i$  the stresses due to the initial and reference load cases separately. Subsequently, they multiply the stresses due to the reference load case by the load multiplier  $\lambda_{\text{crit},i}^{(j)}$  and add these to the stresses induced by the initial load case. To enhance the readability of the resulting equations we have substituted  $\lambda_{\text{crit},i}^{(j)}$  by  $\lambda$  and we dropped the subscript  $i$  and superscript  $(j)$  of the stress components. Hence the resulting stress components read

$$\sigma_{xx} = \sigma_{xx,\text{ini}} + \lambda\sigma_{xx,\text{ref}} \quad (5.2a)$$

$$\sigma_{yy} = \sigma_{yy,\text{ini}} + \lambda\sigma_{yy,\text{ref}} \quad (5.2b)$$

$$\sigma_{xy} = \sigma_{xy,\text{ini}} + \lambda\sigma_{xy,\text{ref}} \quad (5.2c)$$

In their work, they consider tensile failure only and they adopt a principal stress criterion to detect crack initiation. To compute the critical value of  $\lambda$ , they start by substituting the stress components of the set of equations (5.2) into the principal stress equation

$$\sigma_{1,2} = \frac{1}{2}(\sigma_{xx} + \sigma_{yy}) \pm \sqrt{\frac{1}{4}(\sigma_{xx} - \sigma_{yy})^2 + \sigma_{xy}^2} \quad (5.3)$$

Subsequently, they set  $\sigma_{1,2}$  equal to the raised tensile strength  $f_t^+$  according to the adopted saw-tooth law and solve the resulting equation for  $\lambda$ . In that way, they obtained the following closed-form solution

$$\lambda_{1,2} = \frac{-b \pm \sqrt{b^2 - 4ac}}{2a} \quad (5.4)$$

with

$$a = \sigma_{xy,\text{ref}}^2 - \sigma_{xx,\text{ref}}\sigma_{yy,\text{ref}} \quad (5.5a)$$

$$b = f_t^+(\sigma_{xx,\text{ref}} + \sigma_{yy,\text{ref}}) + 2\sigma_{xy,\text{ini}}\sigma_{xy,\text{ref}} - \sigma_{xx,\text{ini}}\sigma_{yy,\text{ref}} - \sigma_{xx,\text{ref}}\sigma_{yy,\text{ini}} \quad (5.5b)$$

$$c = \sigma_{xy,\text{ini}}^2 - \sigma_{xx,\text{ini}}\sigma_{yy,\text{ini}} + f_t^+(\sigma_{xx,\text{ini}} + \sigma_{yy,\text{ini}}) - (f_t^+)^2 \quad (5.5c)$$

Once the load multipliers  $\lambda_{1,2}$  are known, they determine the crack orientation from

$$\gamma_{1,2} = \frac{1}{2} \tan^{-1} \left( \frac{2(\sigma_{xy,\text{ini}} + \lambda_{1,2}\sigma_{xy,\text{ref}})}{(\sigma_{xx,\text{ini}} + \lambda_{1,2}\sigma_{xx,\text{ref}}) - (\sigma_{yy,\text{ini}} + \lambda_{1,2}\sigma_{yy,\text{ref}})} \right) \quad (5.6)$$

The selection scheme to identify the critical integration point works as follows:

- Check at each integration point in each direction  $\gamma$  (determined by Equation (5.6)) the scaled normal stress (using  $\lambda$  from Equation (5.4)) due to the reference load case for tension or compression.
- In case of tension the reference load case has a crack opening effect. Consequently, the corresponding  $\lambda^t$  represents a maximum load multiplier. Compare all values of  $\lambda^t$  and select the minimum  $\lambda_{\min}^t$ . Note the similarity with Equation (2.36).
- In case of compression the reference load case has a crack closing effect. The corresponding  $\lambda^c$  represents a minimum load multiplier that is required to ensure that tensile stresses induced by the initial load case do not exceed the tensile strength. Compare all values of  $\lambda^c$  and select the maximum  $\lambda_{\max}^c$ .
- If  $\lambda_{\min}^t > \lambda_{\max}^c$  then at all integration points a constitutively admissible stress state occurs in case  $\lambda_{\text{crit}}$  is set to  $\lambda_{\min}^t$ . In the next analysis cycle a damage increment is applied to the corresponding integration point.
- However, if  $\lambda_{\min}^t < \lambda_{\max}^c$  then for at least one integration point the resulting tensile stress exceeds the tensile strength irrespective of the value chosen for  $\lambda_{\text{crit}}$ . In that case  $\lambda_{\text{crit}}$  is arbitrarily set to  $\lambda_{\max}^c$  and the damage at the corresponding integration point is incremented in the next analysis cycle.

Graça-e-Costa et al. [30] have shown that the ideas of the strategy by DeJong et al. [16] can also be used in a framework which combines total and incremental approaches.

Harrison [33] proposed an extension to the selection scheme by DeJong et al. [16]. The point is that the original scheme does not consider whether the stress redistribution due to the instantaneous stiffness reduction is feasible without triggering new events elsewhere in the model. That is, it was implicitly assumed that the application of a damage increment does not result in an avalanche of ruptures. The updated set of selection rules does not only take into account the stresses due to the initial and reference load cases but also the load multiplier that was selected in the previous analysis step.

## 5.2.2 Adapted material behavior strategy

To overcome the conceptual difficulty of potential invalid stresses as outlined in the previous subsection, Belletti et al. [4] developed a simplified approach. Basically, they approximate the non-proportional loading response by using the simpler proportional loading scheme as outlined in Section 2.4. The point is that the effects of the initial load case  $\mathbf{F}_{\text{ini}}$  are accounted for by adapting the material properties. Subsequently, they perform the analysis with the reference load case  $\mathbf{F}_{\text{ref}}$  only.

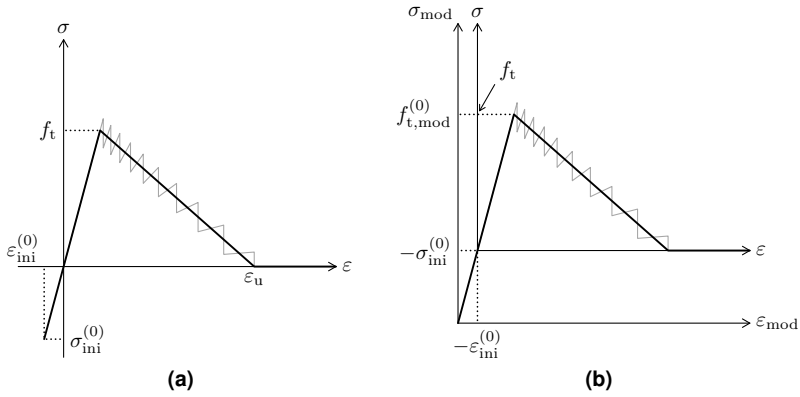


**Figure 5.2** The strategy developed by Belletti et al. [4] uses the stress due to the initial load case ( $\sigma_{ini}$ ) to adapt the material behavior.

Figure 5.2 shows the uniaxial stress–strain relation that they use to exemplify the strategy. One of the assumptions is that the application of  $\mathbf{F}_{ini}$  does not result in any damage. In the example shown, the initial loads induce a compressive stress  $\sigma_{ini}^{(0)}$ . Subsequently, they assume that the stress distribution due to  $\mathbf{F}_{ini}$  remains unchanged throughout the analysis, even though progressive damage occurs due to  $\mathbf{F}_{ref}$ . That is, for any cycle  $j$  they assume  $\sigma_{ini}^{(j)} = \sigma_{ini}^{(0)}$ .

They adopt the usual failure criterion to account for cracking

$$\sigma_{ini}^{(0)} + \lambda_{crit}^{(j)} \sigma_{ref}^{(j)} = f_t^{+(j)} \quad (5.7)$$

with  $f_t^{+(j)}$  the raised residual tensile strength of the considered integration point at step  $j$ . Consequently, the load multiplier  $\lambda_{crit}^{(j)}$  can be calculated as follows

$$\lambda_{crit}^{(j)} = \frac{f_t^{+(j)} - \sigma_{ini}^{(0)}}{\sigma_{ref}^{(j)}} \quad (5.8)$$

In the above equation the numerator can be thought to represent a modified tensile strength

$$f_{t,mod}^{+(j)} = f_t^{+(j)} - \sigma_{ini}^{(0)} \quad (5.9)$$

The primary advantage of the outlined strategy is that the critical load multiplier  $\lambda_{crit}^{(j)}$  can always be defined without obtaining invalid stresses. However, a severe drawback is that open cracks may transfer compressive stresses due to the initial loads, as the redistribution of initial stresses is not taken into account (recall that these were assumed constant throughout the analysis). The authors also mention another drawback that occurs when the crack orientation is not predefined

(e.g. in smeared cracking): the principal stress directions are not affected by the initial loads. Nevertheless, if the initial stresses are relatively small compared to the reference stresses, the outlined approach yields acceptable results.

### 5.2.3 Gradual stress redistribution strategies

In 2010, Eliáš et al. [19] suggested a force-release (F-R) method that is based on a gradual stress redistribution after applying a damage increment to the critical integration point. They recognize that once an event occurs the total applied load should be carried in another way, as the structure will be damaged locally which affects the stress distribution. The key idea is that not only should the material properties of the critical integration point be updated but also the resulting unbalance forces should be added to the nodal forces. Subsequently, the unbalance forces are to be reduced to zero, thereby triggering a stress redistribution. However, before the unbalance forces have completely vanished another event may occur. Note that this was also recognized by Harrison [33], as mentioned at the end of Subsection 5.2.1. If an event occurs before the unbalance forces have vanished, they claim that the outlined procedure can be reapplied to the new situation. In this way, the external loads may change only when all unbalance forces are fully redistributed.

The primary advantage of their scheme is that it avoids stresses that violate the material law for all analysis cycles. On the other hand their work does not show explicitly how to handle multiple ruptures starting from a certain event. In particular, it is not made clear what to do with the unbalance forces that are already present due to a previous rupture. Another disadvantage of their scheme is that it is not capable of tracing snap-back behavior. This is a result of their assumption that the total applied load should be carried by the structure during the stress redistribution process. In other words, it is impossible to obtain any structural snap-backs using this scheme.

In 2015, Eliáš [18] published a generalization of the load-unload (L-U) and F-R methods, which is also suitable for non-proportional loading. In his work, the L-U method is understood to fully unload the structure after each rupture, and then to reload it again until the next rupture occurs. As such, SLA is regarded as a formulation of the L-U method. On the other hand, the F-R method does not change the external load after a rupture, but redistributes the stresses, possibly leading to new ruptures, until a new equilibrium state is found. The paper shows that the L-U and F-R methods can be considered as the extreme cases of the developed general method. The approach that will be presented in Section 5.4 shows similarities with the F-R approach in the sense that total unloadings should be avoided.

## 5.3 Constrained maximization analogy

Inspired by the work of DeJong et al. [16], this section reformulates the non-proportional loading problem in terms of a constrained maximization. Basically, the considered failure criteria constrain the set of load multiplier values at integration point level. A value from this set  $\Lambda_i^{(j)}$  results in stresses at integration point  $i$  that do not conflict with the defined material law. Subsection 5.3.1 explains how to obtain  $\Lambda_i^{(j)}$  for some given failure criterion. Subsequently, we need to consider the load multiplier sets of all integration points in the model simultaneously. That is, we need to extract the common subset  $\Lambda^{(j)}$  of all those load multiplier sets. The resulting load multiplier set  $\Lambda^{(j)}$  at model level is used as input for the maximization which gives the critical load multiplier  $\lambda_{\text{crit}}^{(j)}$  of analysis step  $j$ . Subsection 5.3.2 describes how to obtain  $\Lambda^{(j)}$  and which issues may occur. The aim of the constrained maximization analogy is to provide a more general non-proportional loading formulation for SLA. Furthermore, it is meant to give more insight in the issues associated with non-proportional loading for SLA.

### 5.3.1 Load multiplier sets at integration point level

From a physical viewpoint, the stresses that can occur at some integration point  $i$  of the model are limited by the (residual) material strength  $f_i^{(j)}$ . Generally, for each analysis step  $j$  we can express this as follows

$$\sigma_{\text{gov},i}^{(j)} \leq f_i^{(j)} \quad (5.10)$$

with  $\sigma_{\text{gov},i}^{(j)}$  the governing stress component. For non-proportional loading,  $\sigma_{\text{gov},i}^{(j)}$  depends on the initial stresses  $\sigma_{\text{ini},i}^{(j)}$  and the scaled reference stresses  $\lambda_{\text{ref}}^{(j)} \sigma_{\text{ref},i}^{(j)}$ . In most cases,  $\sigma_{\text{gov},i}^{(j)}$  corresponds to the maximum stress at the integration point. Note that if the material can fail in multiple ways, for each failure mode an equation of the form (5.10) can be set up. For example, at an integration point  $i$  multiple cracks with different orientations may arise or the material may fail either in tension or shear.

Inequality (5.10) may be solved in terms of a set  $\Lambda_i^{(j)}$ . By definition, for any value  $\lambda_{\text{ref}}^{(j)}$  in  $\Lambda_i^{(j)}$  we are assured that the corresponding value of  $\sigma_{\text{gov},i}^{(j)}$  represents a valid stress (i.e. it satisfies the inequality in (5.10)). In the following, we will demonstrate how to obtain  $\Lambda_i^{(j)}$  for a smeared crack model (assuming a state of plane stress). Although we have applied this idea to other material models as well (including bond–slip models and elasto–plastic models) we will not work it out in this thesis. Yet it will be adopted by some of the numerical analyses in the next two chapters.



**Table 5.1** Stress components (in MPa) used for the graphs in Figure 5.3

Figure	$\sigma_{xx,ini}$	$\sigma_{yy,ini}$	$\sigma_{xy,ini}$	$\sigma_{xx,ref}$	$\sigma_{yy,ref}$	$\sigma_{xy,ref}$
5.3a	5	0	0	2.5	0	2
5.3b	-5	0	0	5	2	1
5.3c	-5	0	0	-5	-2	1
5.3d	12	0	-2	1	0	1

**Crack initiation** Let us consider the smeared crack model discussed in Subsection 2.1.2 assuming plane stress conditions. Following the work of DeJong et al. [16], we adopt a principal stress criterion to detect crack initiation, since the crack orientation is not predefined. In other words, we use the maximum principal stress  $\sigma_{1,i}^{(j)}$  as the governing stress component  $\sigma_{gov,i}^{(j)}$  in Equation (5.10). We use Equation (5.4) to calculate the corresponding load multipliers. However, note that the equation may also yield values that correspond to the minimum principal stress  $\sigma_{2,i}^{(j)}$ . The reason is that Equation (5.3) had to be squared in order to solve for  $\lambda_i^{(j)}$ . Hence the sign in front of the square root is lost and thus the distinction between  $\sigma_{1,i}^{(j)}$  and  $\sigma_{2,i}^{(j)}$ . However, in case  $\lambda_i^{(j)}$  corresponds to  $\sigma_{2,i}^{(j)}$ , the load multiplier under consideration can safely be disregarded as by definition  $\sigma_{1,i}^{(j)} \geq \sigma_{2,i}^{(j)}$ . Therefore, we suggest to check whether the obtained  $\lambda_i^{(j)}$  corresponds to  $\sigma_{1,i}^{(j)}$  through backsubstitution in Equation (5.3), considering the plus sign in front of the square root only. Subsequently, we also need to determine whether the verified  $\lambda_i^{(j)}$  represents a minimum or maximum load multiplier. This provides us with sufficient information to define the load multiplier set  $\Lambda_i^{(j)}$ .

To illustrate the outlined approach consider the graphs in Figure 5.3 which are based on the stress components given in Table 5.1.

**Crack extension and secondary cracking** Continuing the example of a smeared crack model and assuming a state of plane stress, we detect crack extension or initiation of a secondary crack as follows. Since we have fixed the orientation of the primary crack, we need to consider the normal stresses  $\sigma_{nn,ini,i}^{(j)}$  and  $\sigma_{nn,ref,i}^{(j)}$  acting on the primary crack face and the normal stresses  $\sigma_{tt,ini,i}^{(j)}$  and  $\sigma_{tt,ref,i}^{(j)}$  acting on the (potential) secondary crack face together with the corresponding raised (residual) tensile strength  $f_{t,n,i}^{+(j)}$  and  $f_{t,t,i}^{+(j)}$ , respectively

$$\sigma_{nn,ini,i}^{(j)} + \lambda_{n,i}^{(j)} \sigma_{nn,ref,i}^{(j)} \leq f_{t,n,i}^{+(j)} \quad (5.11a)$$

$$\sigma_{tt,ini,i}^{(j)} + \lambda_{t,i}^{(j)} \sigma_{tt,ref,i}^{(j)} \leq f_{t,t,i}^{+(j)} \quad (5.11b)$$

Since the inequalities are linear in  $\lambda_i^{(j)}$ , no backsubstitution like for the virgin integration points is required. Also, the inequalities reveal directly whether the determined load multiplier represents a minimum or maximum value. We can now

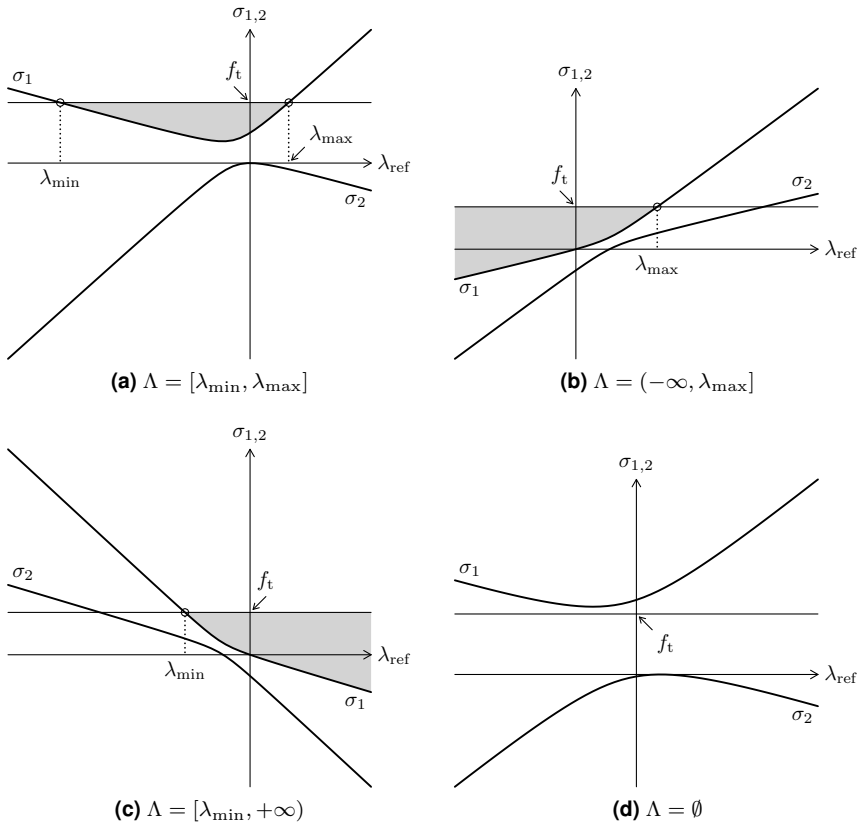


**Figure 5.3** Example load multiplier sets  $\Lambda$  which illustrate four types of sets.

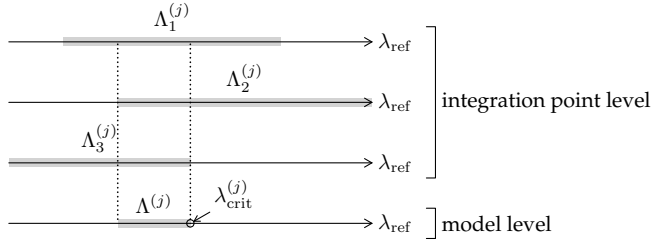


**Figure 5.4** The load multiplier set  $\Lambda^{(j)}$  at model level is the intersection of all individual load multiplier sets  $\Lambda_i^{(j)}$  at integration point level.

define two load multiplier sets:  $\Lambda_{n,i}^{(j)}$  which bounds valid stresses in  $n$ -direction and  $\Lambda_{t,i}^{(j)}$  which bounds valid stresses in  $t$ -direction. Subsequently, we need to extract the common subset  $\Lambda_i^{(j)}$  to obtain a set of load multipliers that results in constitutively admissible stresses in both directions simultaneously. This will be explained in more detail in the next subsection.

### 5.3.2 Load multiplier set at model level

The load multiplier set  $\Lambda^{(j)}$  at model level has to warrant that for each cycle  $j$  inequality (5.10) is fulfilled for all integration points simultaneously. Starting from the load multiplier sets at integration point level (see Subsection 5.3.1), we need to extract the common subset. That is, when we consider all integration points simultaneously, a constitutively admissible stress state is obtained if and only if the set  $\Lambda^{(j)}$  is defined as the intersection of all sets  $\Lambda_i^{(j)}$

$$\Lambda^{(j)} = \bigcap_{1 \leq i \leq N} \Lambda_i^{(j)} = \Lambda_1^{(j)} \cap \Lambda_2^{(j)} \cap \dots \cap \Lambda_N^{(j)} \quad (5.12)$$

with  $N$  the total number of integration points in the model. Figure 5.4 shows a graphical interpretation of Equation (5.12).

Assuming that the set  $\Lambda^{(j)}$  is non-empty, i.e. it contains at least one value, we select its maximum as the critical load multiplier  $\lambda_{crit}^{(j)}$

$$\lambda_{crit}^{(j)} = \max(\Lambda^{(j)}) \quad (5.13)$$

As outlined in Section 2.4, we apply a damage increment to the integration point that yields this load multiplier.

A conceptual difficulty arises when two or more sets  $\Lambda_i^{(j)}$  do not have a value in common, resulting in an empty set  $\Lambda^{(j)}$ . Consequently, a maximum according to Equation (5.13) does not exist. An empty set  $\Lambda^{(j)}$  means that for cycle  $j$  no combination of the initial load case and a scalar multiple of the reference load case exists

without violating the constitutive law at one or more integration points. The next section presents a strategy for non-proportional loading based on the constrained maximization analogy including tactics to cope with the issue of empty load multiplier sets.

## 5.4 Double load multiplier strategies

In order to deal with the conceptual difficulty of an empty load multiplier set  $\Lambda^{(j)}$  as outlined in the previous section and to continue the analysis, we have developed two strategies which will be described in this section. Both strategies are inspired by the idea that we consider two load load multipliers:  $\lambda_{\text{ini}}^{(j)}$  is applied to the initial load case and  $\lambda_{\text{ref}}^{(j)}$  is applied to the reference load case. The double load multiplier method was briefly mentioned in earlier publications [24, 34]. In this section we give a complete description of the method.

Before we will introduce the two so-called double load multiplier strategies, let us first consider the initial loading stage and the combined loading stage assuming no empty load multiplier set  $\Lambda^{(j)}$  arises. Each analysis starts by considering the initial load case  $\mathbf{F}_{\text{ini}}$  only, to allow for damage due to the initial loading to occur. That is, as long as  $\mathbf{F}_{\text{ini}}$  cannot be fully applied without damage initiation or extension we will adopt the proportional loading scheme presented in Section 2.4. In that case, the critical load  $\mathbf{F}_{\text{crit}}^{(j)}$  of cycle  $j$  can be denoted as

$$\mathbf{F}_{\text{crit}}^{(j)} = \lambda_{\text{ini}}^{(j)} \mathbf{F}_{\text{ini}} \quad \text{with } \lambda_{\text{ini}}^{(j)} = \lambda_{\text{crit}}^{(j)} \leq 1 \quad (5.14)$$

As soon as  $\lambda_{\text{ini}}^{(j)} > 1$  the initial loading stage ends, which may already be the case in the first analysis cycle. Subsequently, in the combined loading stage, we add scalar multiples of the reference load case  $\mathbf{F}_{\text{ref}}$  to the initial load case  $\mathbf{F}_{\text{ini}}$ . Assuming a non-empty load multiplier set  $\Lambda^{(j)}$ , the critical load  $\mathbf{F}_{\text{crit}}^{(j)}$  of cycle  $j$  can be written as

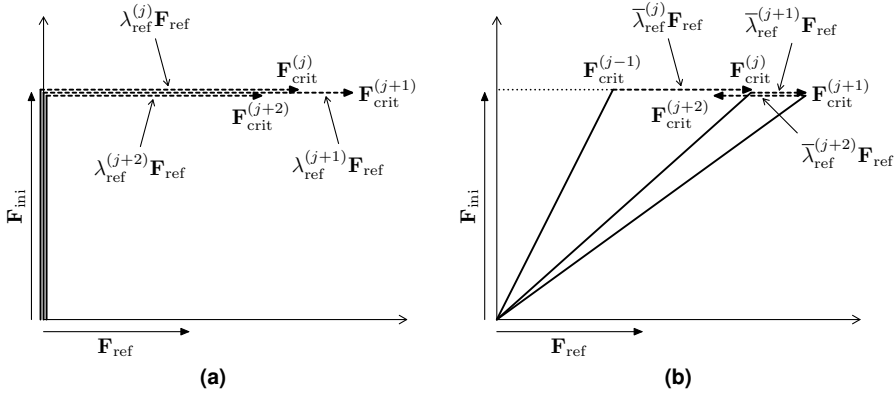
$$\mathbf{F}_{\text{crit}}^{(j)} = \lambda_{\text{ini}}^{(j)} \mathbf{F}_{\text{ini}} + \lambda_{\text{ref}}^{(j)} \mathbf{F}_{\text{ref}} \quad \text{with } \lambda_{\text{ini}}^{(j)} = 1 \text{ and } \lambda_{\text{ref}}^{(j)} = \lambda_{\text{crit}}^{(j)} \quad (5.15)$$

Figure 5.5a demonstrates this for three consecutive steps  $j$  to  $j + 2$ . Alternatively, we could rewrite the above equation by considering  $\mathbf{F}_{\text{crit}}^{(j)}$  the sum of the previous critical load  $\mathbf{F}_{\text{crit}}^{(j-1)}$  and an increment  $\bar{\lambda}_{\text{ref}}^{(j)} \mathbf{F}_{\text{ref}}$  of the reference load case:

$$\mathbf{F}_{\text{crit}}^{(j)} = \bar{\lambda}_{\text{crit}}^{(j)} \mathbf{F}_{\text{crit}}^{(j-1)} + \bar{\lambda}_{\text{ref}}^{(j)} \mathbf{F}_{\text{ref}} \quad \text{with } \bar{\lambda}_{\text{crit}}^{(j)} = 1 \text{ and } \bar{\lambda}_{\text{ref}}^{(j)} = \lambda_{\text{crit}}^{(j)} \quad (5.16)$$

Figure 5.5b demonstrates the alternative approach for the same analysis steps as in Figure 5.5a

As explained in Section 5.3 at times no critical load multiplier  $\lambda_{\text{crit}}^{(j)}$  exists without violating the material law in at least one integration point. Note that in this case even  $\lambda_{\text{crit}}^{(j)} = 0$  does not provide a constitutively admissible stress state. The



**Figure 5.5** Determination of the critical load  $\mathbf{F}_{\text{crit}}$  for three consecutive steps in two different ways that ultimately yield the same result.

first strategy that we propose to deal with this problem is to temporarily not account for  $\mathbf{F}_{\text{ref}}$  but to consider  $\mathbf{F}_{\text{ini}}$  only. That is, instead of Equation (5.15) we solve the following equation:

$$\mathbf{F}_{\text{crit}}^{(j)} = \lambda_{\text{ini}}^{(j)} \mathbf{F}_{\text{ini}} + \lambda_{\text{ref}}^{(j)} \mathbf{F}_{\text{ref}} \quad \text{with } \lambda_{\text{ini}}^{(j)} = \lambda_{\text{crit}}^{(j)} \text{ and } \lambda_{\text{ref}}^{(j)} = 0 \quad (5.17)$$

Figure 5.6a demonstrates this strategy in a graphical way. In effect, we temporarily return to a proportional loading scheme which always has a solution for  $\lambda_{\text{crit}}^{(j)}$  and we temporarily allow the initial load case to be not fully applied. In the next analysis cycle (here  $j + 3$ ) we first try to solve Equation (5.15) and if that fails again (due to an empty load multiplier set  $\Lambda^{(j+3)}$ ) we resort once more to the outlined strategy, i.e. solve Equation (5.17))

The second strategy that we propose in case of an empty load multiplier set is to temporarily scale the last “successful” critical load combination in a proportional way as demonstrated in Figure 5.6b. In other words, instead of Equation (5.16) we temporarily solve the following equation:

$$\mathbf{F}_{\text{crit}}^{(j)} = \bar{\lambda}_{\text{crit}}^{(j)} \mathbf{F}_{\text{crit}}^{(j-1)} + \bar{\lambda}_{\text{ref}}^{(j)} \mathbf{F}_{\text{ref}} \quad \text{with } \bar{\lambda}_{\text{crit}}^{(j)} = \lambda_{\text{crit}}^{(j)} \text{ and } \bar{\lambda}_{\text{ref}}^{(j)} = 0 \quad (5.18)$$

Similar to the first strategy, we temporarily reduce the applied initial load case. The difference is that the second strategy partially retains the scaled reference load case applied so far. Like for the first strategy, the second one attempts to return to the original non-proportional loading equation (here Equation (5.16)) in the next analysis cycle. Also here, if that fails we resort once more to the proposed strategy (i.e. solve Equation (5.18)).

A benchmark study by Lekkerkerker [42] has shown that the first strategy may result in improper damage progression and consequently incorrect results. This

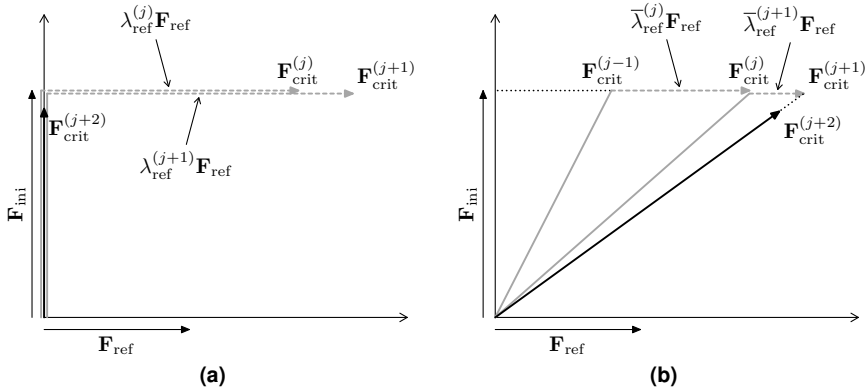


**Figure 5.6** Demonstration of the proposed double load multiplier strategies when  $\Lambda^{(j+2)}$  equals the empty set: either scale the initial load case  $\mathbf{F}_{ini}$  only (a), or scale the last “successful” load combination  $\mathbf{F}_{crit}^{(j+1)}$  (b).

may be attributed to the combination of the current damage state and the temporary removal of the reference load case. Since the model is then loaded by the initial load case only, damage may propagate in unexpected locations. Similar improper behavior was also reported by DeJong et al. [16]. Improved results were obtained with the second strategy [42]. In Section 7.1 we will demonstrate the effectiveness of the second load multiplier strategy by analyzing the behavior of a masonry shear wall.

## 5.5 Conclusions

In this chapter we have formulated the non-proportional loading problem as a constrained optimization assuming an initial load case and a reference load case. The initial load case (e.g. dead weight) is assumed to be permanently present and thus should not be scaled, whereas the reference load case should be scaled such that local failure occurs. Starting point of the approach is that for each integration point in the model we can identify one or more constraints on the load multiplier such that the applicable material law is obeyed. As a result, we get load multiplier sets at integration point level. Subsequently, we need to intersect these sets to obtain a load multiplier set at model level. Any value from this intersection yields a valid combination of the initial and reference load case, i.e. at any integration point we find constitutively admissible stresses. To trigger the next event in the analysis, we have to select the maximum value from this set.

The proposed load maximization fails in case the constraints yield conflicting load multiplier sets at integration point level, resulting in an empty set at model level. That is, we cannot select a value for the load multiplier without violating the

material law at one or more integration points. To deal with this problem we have developed two double load multiplier strategies. Both strategies adjust the applied loading such that a constitutively admissible stress state occurs. The first one resorts to scaling the initial load case when an empty load multiplier set at model level occurs. This implies that in that case the reference load case is multiplied with a factor of zero. The second strategy scales the last “successful” combination of the initial and reference load case when an empty load multiplier set is obtained. Compared to the first strategy, the second one always retains a part of the reference load case. Benchmark tests have shown that in general the second strategy yields better results. Therefore, we will adopt it exclusively in the remainder of this work.

# Chapter 6 Verification and objectivity studies

The previous three chapters presented improvements and extensions for sequentially linear analysis (SLA). In particular, Chapters 3 and 4 focused on methods to set up stepwise secant approximations (or saw-tooth laws) for nonlinear constitutive models, whereas Chapter 5 explained how to deal with non-proportional loading.

The aim of the present chapter is to verify the proposed improvements and extensions and to present objectivity studies. Aspects covered here include the objectivity with respect to mesh and damage increment refinements. A number of benchmark tests have been selected for this purpose. Section 6.1 presents numerical results of a notched beam specimen using the discrete crack approach. This notched beam specimen is analyzed once more in Section 6.2 using a smeared crack approach. Section 6.3 examines a tension–pull specimen which incorporates smeared cracking and bond–slip behavior. Finally, in Section 6.4 we study a pre-compressed masonry specimen loaded in shear using the uncoupled and coupled formulation of the Coulomb friction model.

The next chapter validates the new SLA developments by examining two more complex case studies and comparing the numerical results with other available data. It also mentions several other applications of SLA.

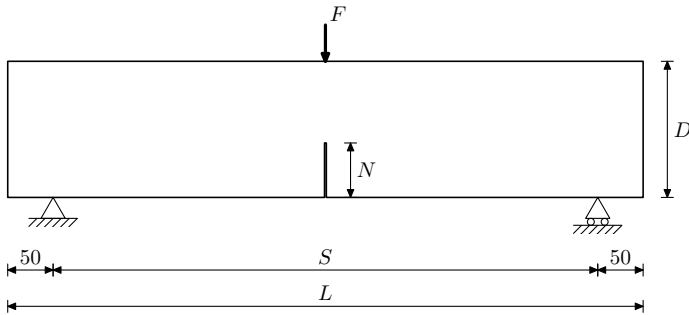
## 6.1 Notched beam specimen with discrete cracking

Elaborating on an earlier study by Van de Graaf, Hendriks, and Rots [27], this section verifies the improved band width ripple concept of Section 3.2 using a discrete crack model. To this end, we have simulated several three-point bending tests by Zhao, Kwon, and Shah [74]. Subsection 6.1.1 introduces the finite element model that has been used for our analyses. Subsequently Subsection 6.1.2 addresses the objectivity of the numerical results with respect to mesh size. Then Subsection 6.1.3 presents the results of an objectivity study with respect to the number of saw-teeth. Finally Subsection 6.1.4 investigates whether a size effect can be observed by analyzing notched beam specimens with a similar geometry, but with different sizes.



**Table 6.1** Dimensions of the notched beam specimens [74].

Specimen	$L$ (mm)	$S$ (mm)	$D$ (mm)	$N$ (mm)
SG2-B1	700	600	150	60
SG2-B3	1300	1200	300	120
SG2-B5	2100	2000	500	200

**Figure 6.1** Mechanical model of the examined notched beam specimens [74]. Table 6.1 gives the specimen-specific dimensions  $S$ ,  $L$ ,  $D$  and  $N$ . The shown dimensions are in mm.

### 6.1.1 Finite element model

Figure 6.1 shows the geometry of the investigated notched beam specimens, all having a thickness of 120 mm and a notch width of 2 mm. The specimen-specific dimensions have been collected in Table 6.1. The load  $F$  results in a mid-span deflection  $u$ , which was measured at the load application point. All numerical analyses have been carried out with beam specimen SG2-B1 except for the size effect study where we also examine beam specimens SG2-B3 and SG2-B5.

The regular meshes consist of quadratic plane stress elements representing the plain concrete and zero-thickness quadratic interface elements to model the anticipated crack. The interface elements have been inserted along a straight vertical line positioned exactly above the notch (Figure 6.2). The plane stress elements have been numerically integrated using a  $2 \times 2$  Gaussian scheme whereas for the interface elements we have adopted a 4-point Newton-Cotes scheme.

Table 6.2 presents the material properties of the beam specimens that we have used for our numerical analyses. Data that was not provided by Zhao et al. [74] has been complemented with data from the companion paper by Kwon, Zhao, and Shah [40]. Note that we have modeled the concrete as a linear-elastic material, whereas all physically nonlinear behavior was lumped into the predefined crack. The stiffness components  $k_n$  and  $k_t$  of the interface elements have been assigned sufficiently high values such that the elastic opening displacements are very small compared to the deformations of the adjacent continuum elements. Furthermore, we assume the variable shear retention relation of Equation (2.16). For all analyses

**Table 6.2** Material properties of the notched beam specimens for the discrete crack analyses [74, 40].

Material	Elasticity	Tensile failure
Plain concrete	$E_c = 16.0^*$ GPa $\nu_c = 0.15^\dagger$	None
Predefined crack	$k_n = 1.0 \times 10^6$ N/mm <sup>3</sup> $k_t = 1.0 \times 10^6$ N/mm <sup>3</sup>	Exponential tension softening $f_t = 3.78$ MPa $G_f^I = 300^\ddagger$ J/m <sup>2</sup>

\* We assigned a smaller Young's modulus  $E_c$  to fit the initial stiffness of the numerical analyses with the experimental results.

† Assumed value.

‡ Estimated value based on graphical data in [74].

in this section we have adopted 45 saw-teeth to approximate the tension softening behavior, unless stated otherwise.

### 6.1.2 Mesh size objectivity

Five different mesh sizes have been used ranging from “very coarse” to “very fine” to study the effect of mesh size on the peak load and the post-peak behavior. We have chosen the number of interface elements along the predefined crack as follows:

- Very coarse mesh: 3 elements
- Coarse mesh: 6 elements
- Medium mesh: 9 elements
- Fine mesh: 18 elements
- Very fine mesh: 36 elements

Figures 6.2a and 6.2b give an impression of the very coarse and very fine mesh, respectively.

Figure 6.3a shows the obtained load–deflection curves. They have been constructed by connecting the scaled  $(F, u)$  pairs of all analysis cycles. The load–deflection curves show that the obtained peak load and the post-peak behavior are only marginally affected by the mesh size. In other words, the peak load and the post-peak behavior are virtually objective with respect to mesh size. Note that the envelope of the load–deflection curves becomes smoother when a finer mesh is used. However, the magnitude of the local jumps is hardly affected by a mesh refinement. To support this observation we have included separate plots of the load–deflection curves obtained with the very coarse and very fine meshes in Figures 6.3b and 6.3c, respectively.

To demonstrate that the peak loads converge to some ultimate value upon increased mesh refinement we have collected the relative peak loads in a histogram

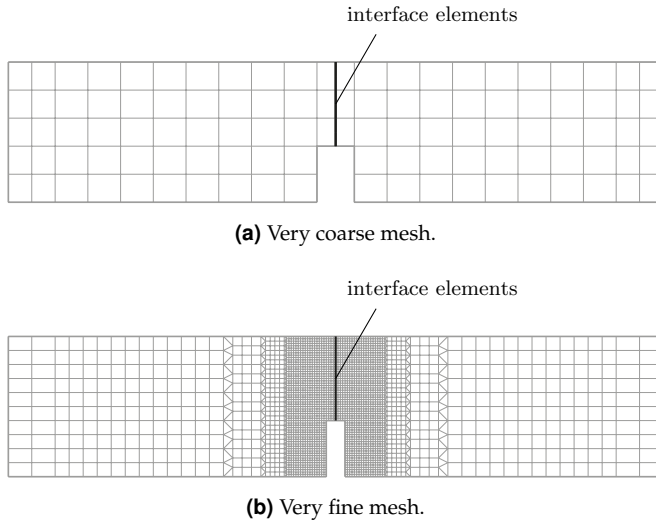


**Figure 6.2** Two meshes adopted for the notched beam analyses using the discrete crack approach.

(Figure 6.3d). Here the relative peak load has been calculated as the numerically obtained peak load divided by the experimental peak load. Hence, the corresponding semi-transparent bars in the histogram also provide insight in how closely the experimental peak value is resembled. Note that the bar colors correspond to the line colors in Figure 6.3a.

The dissipated energy at the end of each numerical analysis is nearly equal for all simulations, and it is in line with the input fracture energy. However, it deviates significantly from the experimental one. The opaque bars in Figure 6.3d indicate the ratio between the numerically obtained energy dissipation and the experimental one, both defined as the area enclosed by the envelope of the load–deflection curve. An explanation for the difference between the experimental and numerical value can be found in the adopted value for the fracture energy. From the experimental load–deflection curve we have determined the dissipated energy to be approximately equal to 2.24 J. If we assume a perfectly plane and smooth fracture surface, as we did for our simulations, then the fracture energy  $G_f^I$  should be:  $G_f^I = g_f^I/A = 2.24 \text{ J}/(0.090 \text{ m} \times 0.120 \text{ m}) = 207 \text{ J/m}^2$ , whereas the adopted estimated value equals  $300 \text{ J/m}^2$ . Note that this factor of roughly 1.5 is also seen in Figure 6.3d.

### 6.1.3 Saw-tooth objectivity

To study the effect of the number of saw-teeth on the results, we adopted saw-tooth laws with 30, 45 and 90 saw-teeth (see Table 6.3 and Figure 6.4). Note that due to the combination of a high penalty stiffness  $k_n$  with the saw-tooth ripple concept

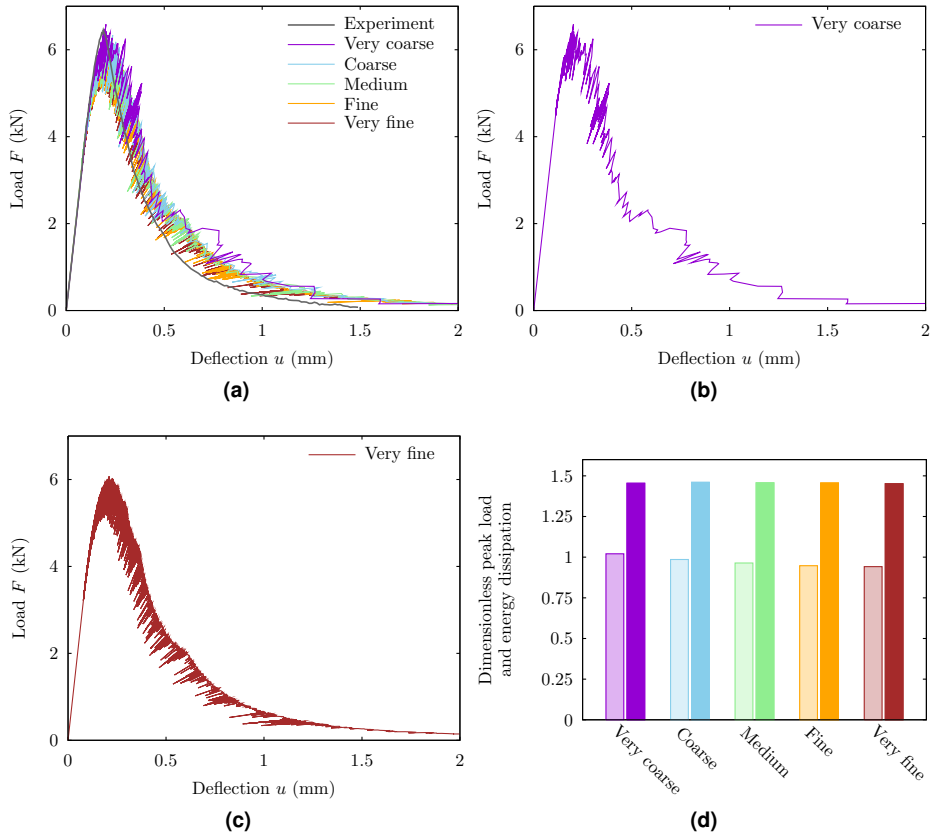


**Figure 6.3** Load–deflection curves of notched beam specimen SG2-B1 for five mesh sizes obtained with SLA using the discrete crack approach. The bars in (d) show for each mesh size the numerical peak load (semi-transparent) and dissipated energy (opaque) divided by the corresponding experimental value.

**Table 6.3** Band width parameters  $p_1$  and  $p_2$  per saw-tooth law.

Number of saw-teeth	$p_1$	$p_2$
30	$1.541 \times 10^{-1}$	$1.887 \times 10^{-1}$
45	$1.110 \times 10^{-1}$	$1.201 \times 10^{-1}$
90	$6.275 \times 10^{-2}$	$5.353 \times 10^{-2}$

most of the fracture energy is released by the last few saw-teeth. That is typical for this kind of analysis. For all simulations in this section, we employed a medium mesh size. Hence, note that the analysis with 45 saw-teeth presented here is in fact identical to the one of the previous subsection.

The numerical load–deflection curves show good agreement with the experimentally obtained curve (see Figure 6.5a). Similar to what we have seen in the previous subsection on mesh size objectivity, we observe that the peak load and the post-peak behavior are only slightly affected by adopting a more refined saw-tooth law. However, note that the size of the local jumps—typical of *SLA*—decreases upon increasing the number of saw-teeth. To better illustrate this effect, we have made separate plots of the load–deflection curves from the simulations with 30 and 90 saw-teeth in Figures 6.5b and 6.5c, respectively.

Before we explain the smaller local jumps in the load–deflection diagram, let us first investigate why these jumps occur in the first place. We will do this by focusing on a single jump in the load–deflection curve of the simulation with a coarse mesh and 45 saw-teeth (see Figure 6.6a). The considered jump actually consists of four points (corresponding to cycles 647 up to and including 650) joined by straight line segments. For those four cycles, we have drawn the normal tractions across the crack with red lines. Dashed lines indicate the integration point values. The tensile strength values at the integration points have been indicated by dark-blue lines. Considering cycle 647 (see Figure 6.6b) we can see that at several integration points the normal tractions are almost equal to the tensile strength. Yet, we only select the critical one (indicated with a filled dot) and apply a damage increment overthere. Consequently, the normal stiffness and the tensile strength are reduced at this integration point. In the next linear analysis (cycle 648, see Figure 6.6c), a stress redistribution takes place which relieves the previously critical integration point (indicated by a non-filled dot). Nevertheless, the adjacent integration points have almost no additional capacity left to take over the released stresses. The only way to cope with these additional stresses is to apply a somewhat smaller load factor  $\lambda_{\text{crit}}$  in cycle 648, which results in slightly decreased loads and displacements. The same phenomenon is observed in the next two cycles (see Figures 6.6d and 6.6e).

Smaller jumps in the load–deflection curve when using a larger number of saw-teeth can now be understood as follows. More saw-teeth implies smaller damage increments between subsequent cycles. Consequently, the decrease in stress at the critical integration point and the accompanying stress increase at adjacent integra-

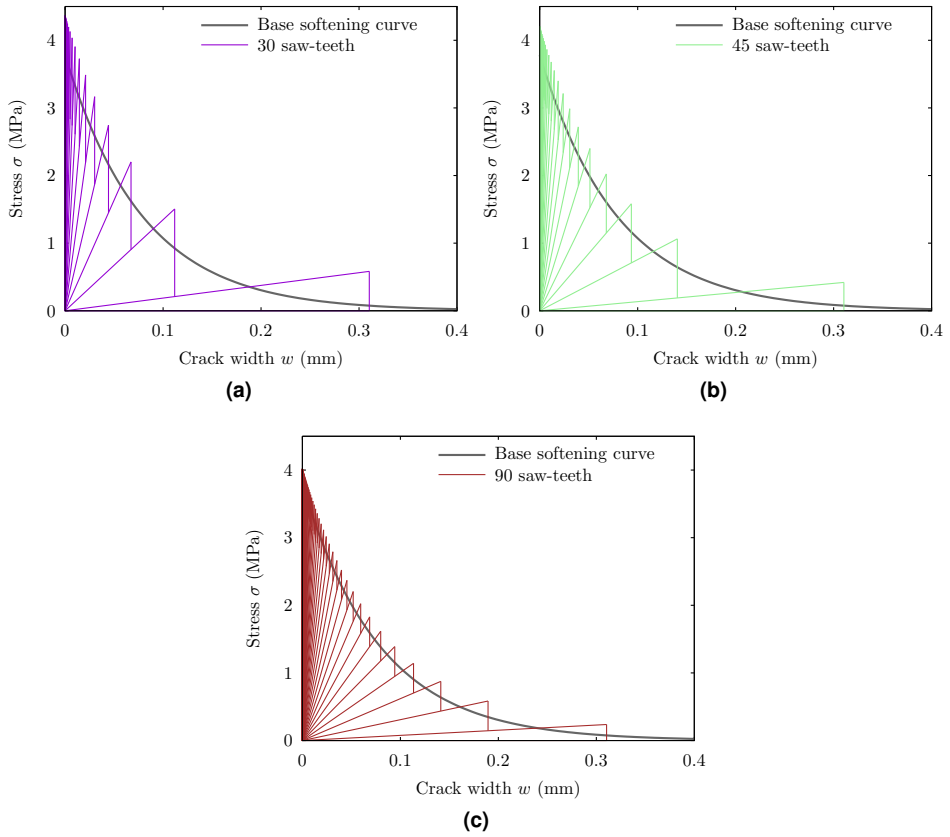


**Figure 6.4** Saw-tooth laws for the exponential softening curve consisting of 30, 45, and 90 saw-teeth, set up with the improved band width ripple concept.

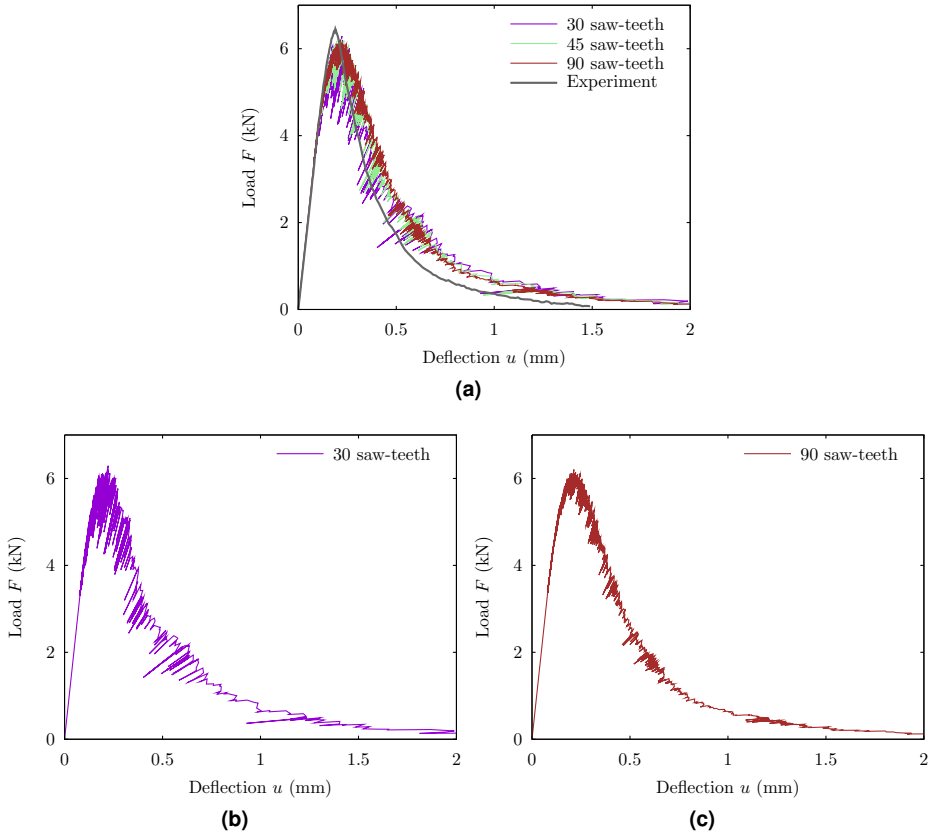
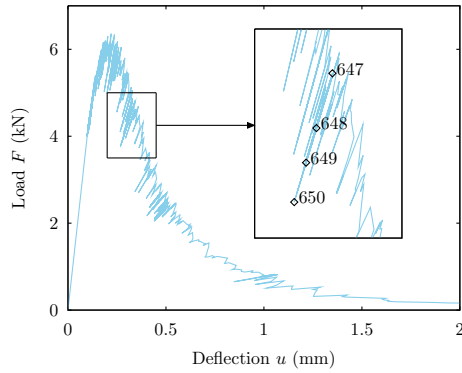
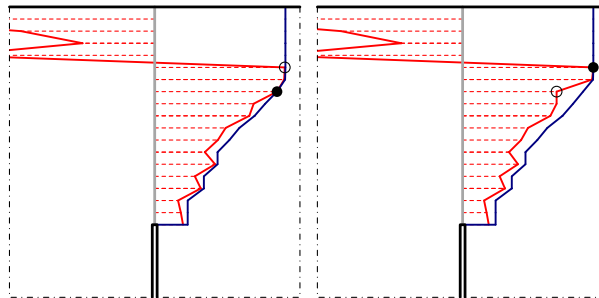


**Figure 6.5** Load–deflection curves of notched beam specimen SG2-B1 for different number of saw-teeth obtained with SLA using the discrete crack approach and a medium mesh size.

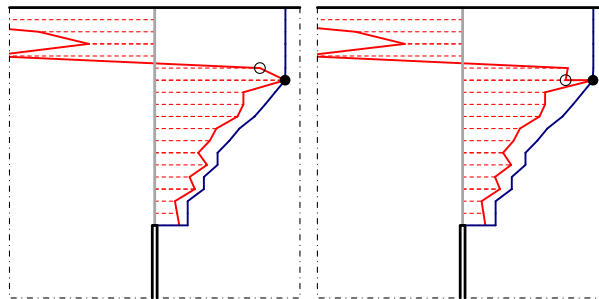


(a) Coarse mesh, 45 saw-teeth



(b) Cycle 647

(c) Cycle 648



(d) Cycle 649

(e) Cycle 650

**Figure 6.6** Normal traction and tensile strength values at the integration points, drawn with red and blue lines, respectively, for four subsequent cycles. The filled (“●”) and non-filled (“○”) dots denote the present and previous critical integration points, respectively.



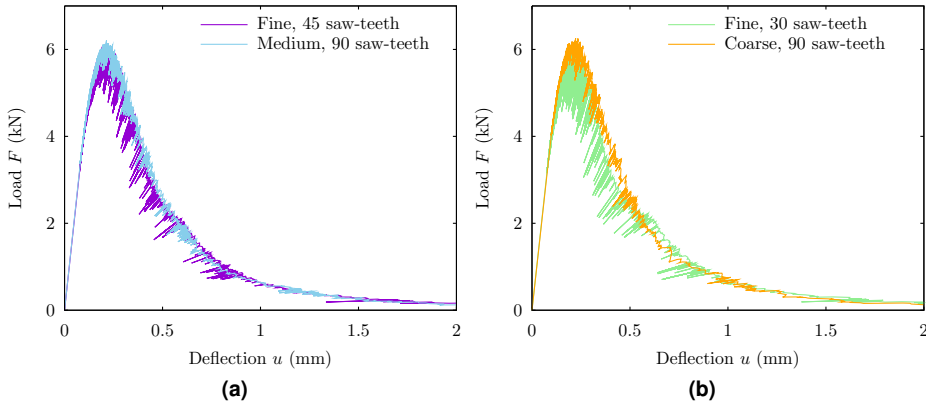


**Figure 6.7** Two comparisons of numerical analyses that require similar computational efforts in terms of number of linear analyses. Note that the size of the local snap-backs is significantly reduced when more saw-teeth are employed.

tion points is less severe. Thus, the decrease in the critical load factor  $\lambda_{\text{crit}}$  is also smaller which in turn results in smaller local jumps.

**Mesh refinement vs. saw-tooth refinement** To spend the available computing time as efficient as possible, we have examined which type of refinement improves the numerical results the most. We have made two comparisons, each one requiring a similar computational effort in terms of number of linear analyses. The first comparison considers the results of a simulation using a fine mesh and 45 saw-teeth and the results of a simulation using a medium mesh and 90 saw-teeth (see Figure 6.7a). Both simulations require about 3240 cycles,  $45 \times 18 \times 4$  and  $90 \times 9 \times 4$ , respectively, to establish a state of complete rupture (recall that the interface elements have four integration points each). For the second comparison we have used more extreme parameters: a fine mesh with 30 saw-teeth and a coarse mesh with 90 saw-teeth (see Figure 6.7b). For this comparison, both simulations require about 2160 analysis steps,  $30 \times 18 \times 4$  and  $90 \times 6 \times 4$ , respectively. Both comparisons show that the results are improved more by a saw-tooth refinement than by a mesh refinement. In particular, the local jumps which are typical of simulations with SLA are significantly reduced. This helps us in assessing the load-deflection diagram and in interpreting the local jumps (whether these represent structural snap-backs or not).

#### 6.1.4 Size effect

To investigate whether or not a size effect can be simulated using SLA, we have studied three specimens with a similar geometry but different dimensions (see Ta-

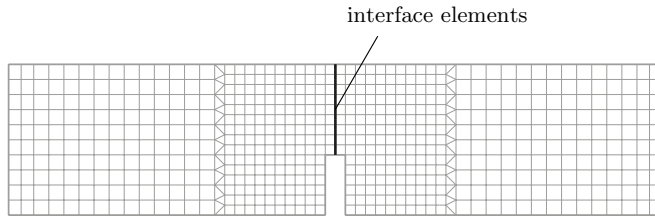


**Figure 6.8** Mesh of notched beam specimen SG2-B3 using the discrete crack approach.

ble 6.1). The smallest specimen (SG2-B1) has been investigated extensively in the previous subsections. The next specimen (SG2-B3) has dimensions which are twice as large as those of specimen SG2-B1. The largest specimen (SG2-B5) is a factor  $\frac{5}{3}$  larger than specimen SG2-B3. The only dimension that is the same for all specimens is the beam thickness:  $t = 120$  mm.

The computational models of the three beam specimens have been prepared as follows. For all meshes, nine interface elements were applied along the predefined crack. Also the way the models have been meshed is similar for all three models. Hence the size of the finite elements varies from model to model, but the mesh layout does not. Figure 6.8 displays the mesh of beam specimen SG2-B3. All material properties, including tensile strength and fracture energy, have been assigned the same values for all specimens (see Table 6.2). Recall that for the saw-tooth law we have used 45 saw-teeth.

Figure 6.9 displays the obtained dimensionless load–deflection curves which show a size effect. The horizontal axis was made dimensionless by dividing the mid-span deflection  $u$  by the beam thickness  $t$ , whereas the vertical axis was made dimensionless by dividing the applied load  $F$  by the uni-axial crack load  $F_{cr}$ :  $F_{cr} = f_t t (D - N)$ . In this way, the area enclosed by each of the three curves should be equal to  $G_f^I / (f_t t)$ , since the parameters  $G_f^I$ ,  $f_t$  and  $t$  are the same for all simulations. If there would be no size effect, the three curves should overlap. Obviously, they do not. Apparently, for larger specimen sizes the relative load bearing capacity decreases. Although this is known from literature, these analyses confirm that the size effect can be reproduced using SLA.

## 6.2 Notched beam specimen with smeared cracking

This section analyzes again notched beam specimen SG2-B1 from Section 6.1; however, here we employed a smeared crack approach. Consequently, we have removed the line interface elements from the mesh. All adopted models bridge the notch width by a single element. To ensure that the expected crack is smeared out over the full width of the element, we have adopted linear instead of quadratic elements. In that way we can make an accurate estimation of the actual crack band width  $h$  since the horizontal strain distribution is constant for linear elements. A

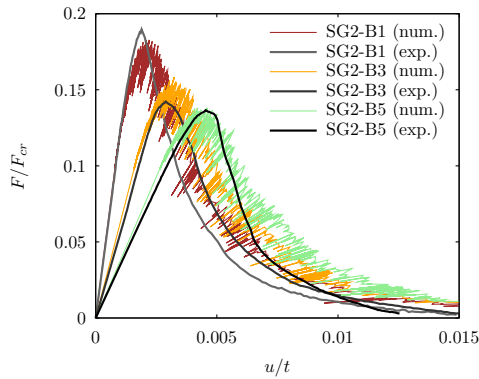


**Figure 6.9** Size effect observed for the notched beam specimens.

more rigorous approach would have been to enhance the smeared crack model with a crack-tracking technique, e.g. the one proposed by Cervera, Pelà, Clemente, and Roca [10]. More recently, numerical simulations with SLA using the proposed crack-tracking technique have been carried out by Slobbe, Hendriks, and Rots [69] and Slobbe [70].

The properties related to tensile failure previously assigned to the predefined crack (Table 6.2) are now applied to the plain concrete. For all simulations with SLA presented in this section we have adopted a saw-tooth law with 20 saw-teeth, unless stated otherwise. The reason to use less saw-teeth by default than in the section on the discrete crack approach is that here we do not have to overcome a high dummy stiffness. Furthermore we have adopted the variable shear retention relation of Equation (2.16).

Similar to what we have done in the previous section, we start by investigating the sensitivity with respect to mesh size (Subsection 6.2.1) and damage increment size (Subsection 6.2.2). In this work we have not studied the effect of mesh-directional bias since that has already been carried out by DeJong et al. [15]. Subsection 6.2.3 verifies the saw-tooth model presented in Subsection 3.3 for extremely brittle materials using a notched beam with fictitious mechanical properties.

### 6.2.1 Mesh size objectivity

The numerical simulations in this subsection are based on the same five mesh refinements listed in Section 6.1.2, ranging from “very coarse” to “very fine”. This approach makes it possible to compare similar analyses using different crack modeling strategies. In each smeared crack analysis, the crack band width  $h$  has been assumed equal to the width of the elements located above the notch, since we expect the crack to localize in that zone:

- Very coarse mesh:  $h = 30$  mm

- Coarse mesh:  $h = 15$  mm
- Medium mesh:  $h = 10$  mm
- Fine mesh:  $h = 5$  mm
- Very fine mesh:  $h = 2.5$  mm

When presenting the results, we use the same color scheme as adopted in the previous subsection on mesh size sensitivity.

The load–deflection curves in Figure 6.10a show several similarities with the ones obtained with the discrete crack approach (Figure 6.3a). Observe again the limited mesh size dependency with respect to the predicted peak loads. Note also here the smoother envelope curve upon increasing mesh refinement. And similar to what we have seen for the discrete crack approach, the local jumps in the structural response do not diminish upon mesh refinement. In fact, the number of local jumps increases when a more refined mesh is adopted. Once more, this effect is illustrated by comparing the individual curves of the very coarse and very fine meshes in Figures 6.10b and 6.10c, respectively.

Nevertheless, we also observe some differences with respect to the results presented in Subsection 6.1.2. Most notably, the post-peak capacity increases upon mesh refinement. Consequently, also the dissipated energy corresponding to an analysis with a finer mesh increases. This effect is shown by the opaque bars in Figure 6.10d, which indicate per analysis the ratio between the dissipated energy obtained numerically and experimentally. In particular the fine and very fine meshes show a pronounced increase in dissipated energy. To explain this kind of behavior, we need to consider the obtained crack patterns. Figure 6.11 shows the computed crack patterns at 1.0 mm deflection. Here, fully developed cracks are marked with thick black line segments, whereas partially opened cracks are indicated with thin dark gray line segments. Notice that for the very coarse, coarse, and medium meshes, the crack patterns are as expected: the crack localizes in a straight narrow band right above the notch. However, for the fine and very fine meshes we observe a more diffuse crack pattern near the top of the beam. This issue has been addressed by Slobbe et al. [69]. Although those cracks are not fully developed, they do contribute to the energy dissipation. Moreover since those cracks are inclined the assumed crack band width does not equal the actual crack band width. Also note that orthogonal cracks arise which contribute to the energy dissipation as well.

Yet, the predicted maximum crack width at 1.0 mm deflection is quite similar for all five simulations. The predicted maximum crack width  $w_{\max}$ , which was calculated as the product of the maximum crack strain  $\varepsilon_{cr, \max}$  and the crack band width  $h$ , varies from 0.513 mm for the simulation with the very coarse mesh to 0.557 mm for the analysis with the medium mesh. All maximum crack widths have been added to the captions of the pictures in Figure 6.11.

In the present work, we only addressed the issue of mesh size sensitivity. However, the results may also be dependent on another mesh-related aspect, namely

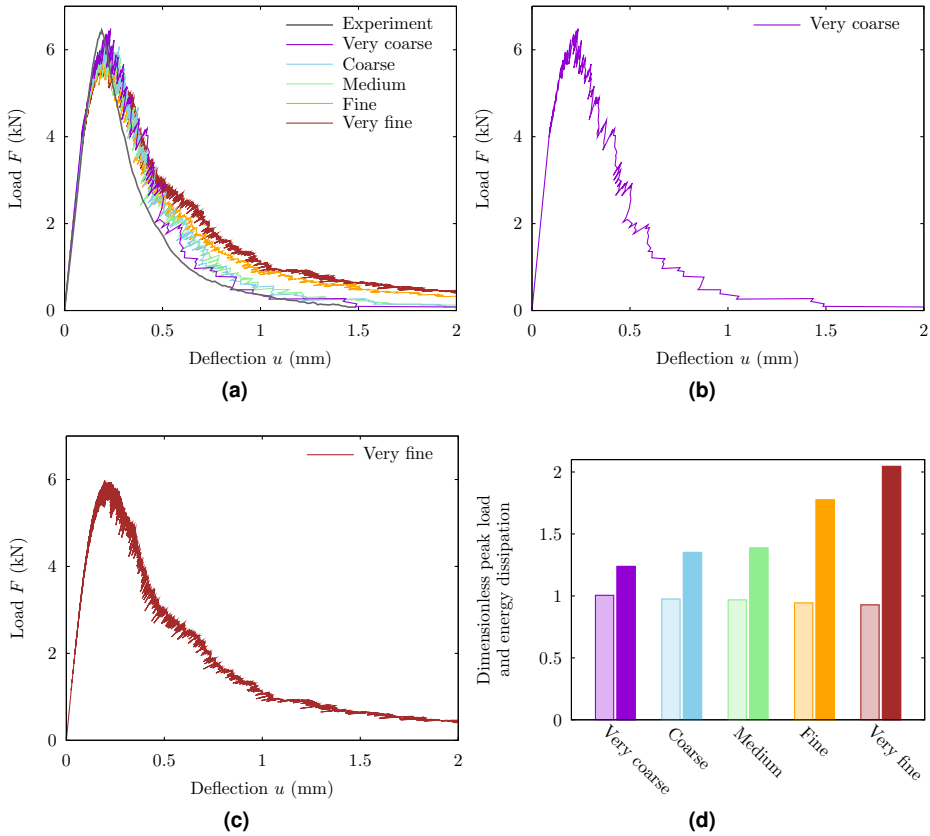


**Figure 6.10** (a)-(c) Load-deflection curves of notched beam specimen SG2-B1 for five levels of mesh refinement obtained with SLA using a smeared crack approach. (d) Numerical peak loads (semi-transparent bars) and dissipated energies (opaque bars) divided by their experimental counterparts, per mesh size.

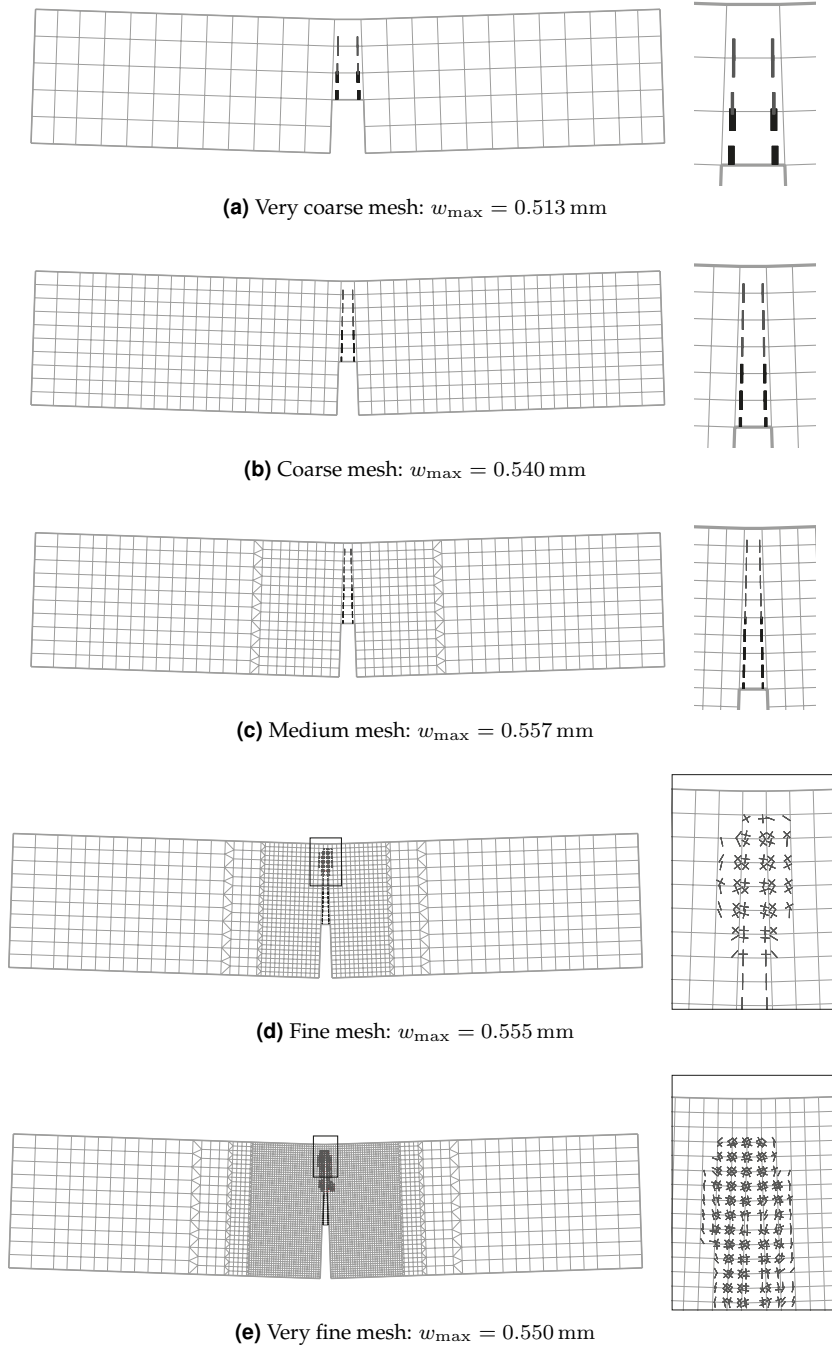


**Figure 6.11** Crack patterns and maximum crack widths at 1.0 mm deflection, predicted with SLA using five different mesh sizes.

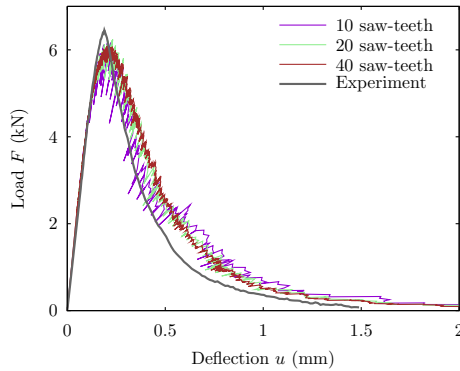


**Figure 6.12** Load–deflection diagrams of notched beam specimen SG2-B1 using a smeared crack approach for different numbers of saw-teeth.

mesh alignment. DeJong et al. [15] have studied the effect of mesh alignment on the numerical results in detail and Slobbe, Hendriks, and Rots [68] presented a systematic mesh alignment test. They both demonstrated that crack patterns may align with the meshing lines, in particular for regular meshes. They also showed that mesh alignment can be effectively limited by adopting an irregular triangulated mesh.

## 6.2.2 Saw-tooth objectivity

To study the effect of damage increment refinement on the numerical results, we have run two additional analyses adopting saw-tooth laws consisting of 10 and 40 saw-teeth, respectively. For both simulations a medium mesh was employed. Figure 6.12 shows the obtained load–deflection curves including the analysis from the previous subsection obtained with a medium mesh and 20 saw-teeth. From the displayed curves we can observe a limited effect of the damage increment size on the peak load and post-peak behavior. We have also found crack patterns which are virtually identical to the one shown in Figure 6.11c.

Note that the conclusions which we can draw from the displayed diagram are in line with the conclusions presented in the subsection on damage increment sensitivity of the discrete crack model. Also here, we can see that an increase in number of saw-teeth, which is equivalent to a damage increment refinement, results in smaller local jumps along the curve. The explanation for this phenomenon given in Subsection 6.1.3 also applies to the results shown here.

## 6.2.3 Snap-back at constitutive level

Elaborating on the study by Invernizzi et al. [39], this subsection verifies the ripple approach for extremely brittle materials of Subsection 3.3 by analyzing an aca-

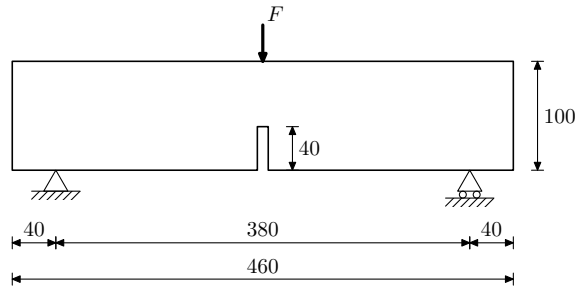


**Figure 6.13** Mechanical model of the extremely brittle notched beam. All dimensions are in mm.

**Table 6.4** Fictitious material properties of the extremely brittle notched beam.

Elasticity	Tensile failure
$E = 40$ GPa	Linear tension softening
$\nu = 0.15$	$f_t = 40$ MPa
	$G_f^I = 200$ J/m <sup>2</sup>

demically notched beam with fictitious material properties. The motivation of this study is to examine the behavior of SLA in case of constitutive laws with snap-backs, relevant for materials with extremely brittle properties and/or practical finite element models with relatively large elements.

The mechanical model of the 50 mm thick beam is shown in Figure 6.13. We examine three regular meshes, using different numbers of elements above the notch:

- Coarse mesh: 3 elements
- Medium mesh: 6 elements
- Fine mesh: 12 elements

All meshes consist of quadrilateral linear plane stress elements which are numerically integrated using a  $2 \times 2$  Gaussian scheme. Pictures of the meshes are provided when the computed crack patterns are presented.

The three mesh refinements result in three different constitutive relations through the varying crack band width  $h$ , which is chosen equal to the element width. Assuming linear softening and the fictitious mechanical properties of Table 6.4, we found a snap-back at constitutive level for the coarse mesh. We prepared two saw-tooth laws for this constitutive relation: one with 20 saw-teeth (Figure 6.14a) and one with 80 saw-teeth (Figure 6.14b). The element size of the medium mesh was chosen such that a perfectly brittle material behavior was obtained (Figure 6.14c). We have approximated that stress-strain relation with two saw-tooth laws: one consisting of a single saw-tooth and another one consisting of 20 saw-teeth. Due to the relatively small element size, the fine mesh resulted in a common tensile



**Table 6.5** Band width parameters  $p_1$  and  $p_2$  per model.

Mesh size	Number of saw-teeth	$p_1$	$p_2$
Coarse	20	$1.824 \times 10^{-2}$	$1.824 \times 10^{-2}$
Coarse	80	$4.387 \times 10^{-3}$	$4.387 \times 10^{-3}$
Fine	20	$3.524 \times 10^{-2}$	$3.587 \times 10^{-2}$

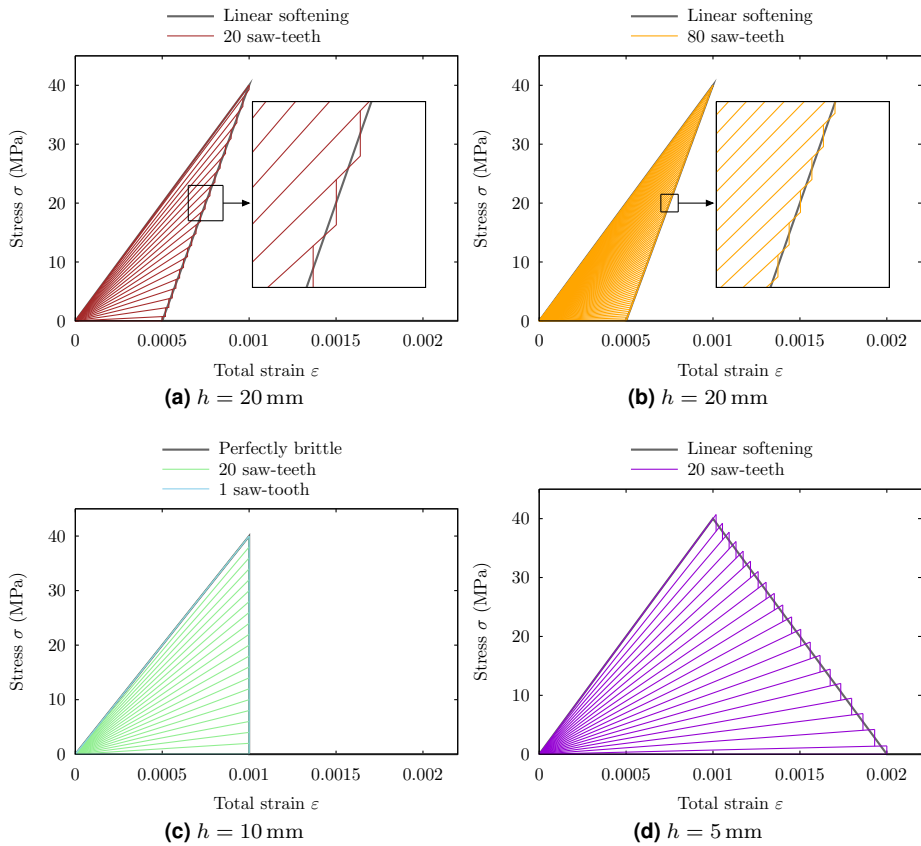
strain-softening law for which we prepared a saw-tooth law consisting of 20 saw-teeth (Figure 6.14d). Table 6.5 shows the crack band parameters for the relevant models.

Figure 6.15 shows the obtained load–deflection curves from which we can deduce a mesh size dependency of the peak load and the post-peak behavior. Observe that the peak load decreases upon increasing mesh refinement. Through linear-elastic analyses we have found that the maximum stress right above the notch significantly increases when smaller elements are used for some given imposed deflection  $u$ . On the other hand, the initial tensile strength is almost invariant for all five saw-tooth laws (Figure 6.14). Hence, the maximum applied load decreases upon mesh refinement which is well-known from an early study by Bažant and Cedolin [2]. Regarding the two analyses with a coarse mesh, it turned out that the structural response is virtually identical for 20 and 80 saw-teeth. That is, the load–deflection curves of those two analyses coincide, although the number of points along the curve is greater when 80 saw-teeth are adopted. Note that this is not true for the two analyses with the perfectly brittle behavior. We return to this observation at the end of this subsection.

Figure 6.15d displays the dissipated energy for the five analyses. The dissipated energy was calculated as the area enclosed by the load–deflection curve. Note that for all analyses except one the dissipated energy values are quite similar. From the displayed histogram we can conclude that we would better avoid the use of a single saw-tooth, even for the case of perfectly brittle material behavior, as it may yield a significant overestimation of the dissipated energy.

Nevertheless, the crack patterns at approximately 0.5 mm deflection shown in Figure 6.16 meet our expectations. For all analyses, the crack localizes in a narrow band of one element wide and no spurious cracking near the top face of the beam is found. We also calculated the maximum crack width  $w_{\max}$  for the presented crack patterns as the product of the maximum crack strain and the crack band width. Although we notice some scatter in these values, we consider them acceptable.

In order to demonstrate that the earlier found peak load dependency on the mesh size is to be attributed to the presence of the notch rather than to our saw-tooth models, we have run three additional simulations. For those analyses we have adopted a beam model without a notch. The obtained load–deflection curves showed a small, yet acceptable, sensitivity with respect to the mesh size.



**Figure 6.14** Several constitutive relations and saw-tooth laws of the extremely brittle material, assuming different values of the crack band width  $h$  and number of saw-teeth. The largest value of  $h$  results in a snap-back at constitutive level.

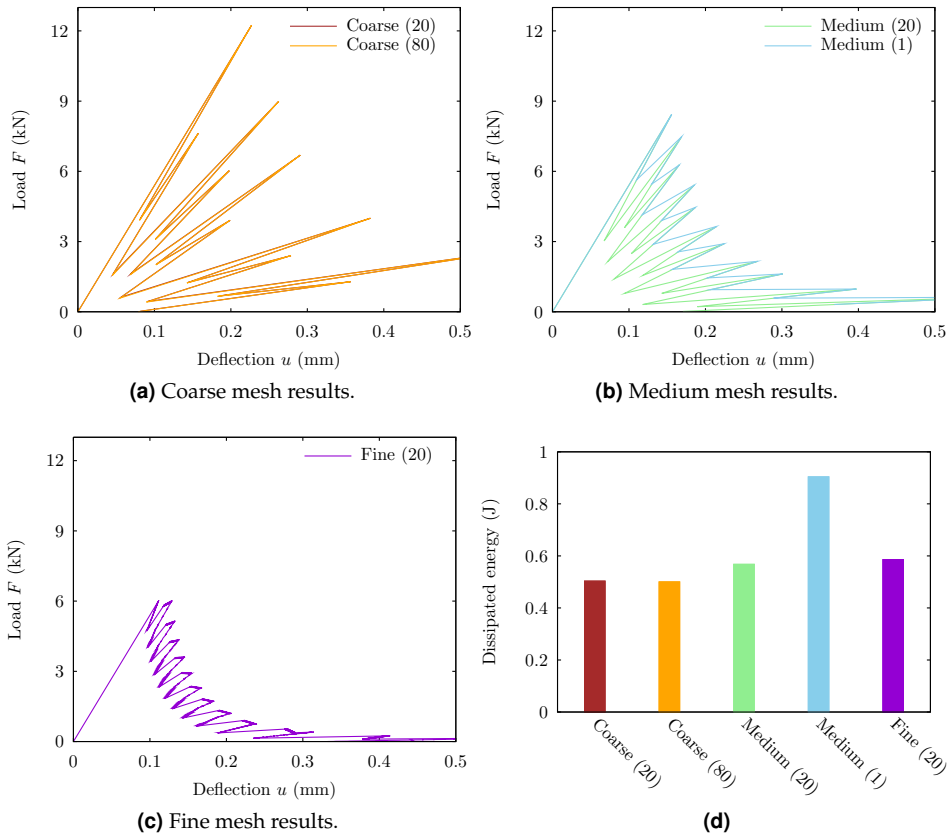
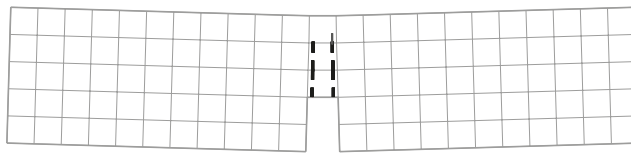
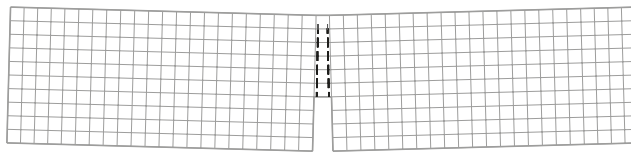


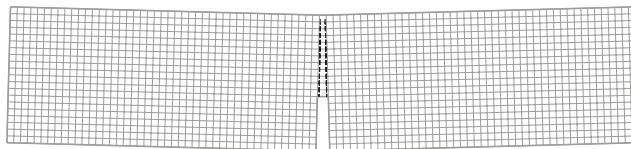
**Figure 6.15** Load–deflection curves of a notched beam with extremely brittle material properties for five combinations of mesh size (coarse, medium or fine) and number of saw-teeth (1, 20 or 80).



(a) Coarse mesh:  $w_{\max} = 0.24$  mm.



(b) Medium mesh:  $w_{\max} = 0.28$  mm.



(c) Fine mesh:  $w_{\max} = 0.30$  mm.

**Figure 6.16** Crack patterns of the extremely brittle notched beam at approximately 0.5 mm deflection, computed with SLA using three different mesh sizes.

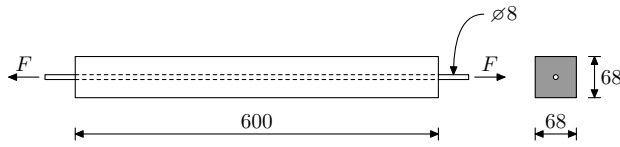


Figure 6.17 Examined RC tension-pull specimen [25].

## 6.3 Tension–pull specimen with smeared cracking and bond–slip

Elaborating on the work by Ensink [20] and Ensink, Van de Graaf, Slobbe, Hendriks, and Rots [21], we have numerically simulated the tension–pull experiment by Gijsbers and Hehemann [25] to validate the SLA approach using smeared cracking in combination with a bond–slip model. Figure 6.17 shows the geometry of the reinforced concrete (RC) tension–pull specimen.

This section is built up as follows. Subsection 6.3.1 describes the finite element model that we have used for our analyses. In Subsection 6.3.2 we present the results of our analysis using a homogeneous specimen without imperfections. As we will show, this does not pose any difficulties for the SLA-based simulation. However, we have been unable to obtain a properly converged solution for this model using incremental–iterative analysis. By pre-defining three weakened cross-sections we have been more successful with this approach. Subsection 6.3.3 presents the corresponding results and compares them with SLA-based results.

### 6.3.1 Finite element model

For all analyses of the tension–pull specimen we have adopted a plane stress model. Although an axi-symmetric model would have been more appropriate in this case considering the ring forces that may occur, we have decided to maintain the plane stress results from our initial studies. The reason is that this benchmark test is meant to demonstrate the advantages of SLA over incremental-iterative analysis in case of a homogeneous stress distribution and to demonstrate that it automatically captures structural snap-backs.

Our numerical model of the RC specimen consists of three parts: concrete, a reinforcement bar (“rebar” for short) and the interface between them. We have modeled the concrete with linear quadrilateral plane stress elements using a  $2 \times 2$  Gaussian integration scheme. The regular mesh consists of 70 elements over the specimen length and 8 elements over the depth. Since the cracks are expected to follow the mesh lines, we have chosen the crack band width  $h$  equal to the element width of 8.6 mm. The steel rebar has been modeled with linear truss elements that are directly integrated. These truss elements are connected to the plane stress elements through linear interface elements with a 3-point Newton-Cotes integration

**Table 6.6** Adopted material properties of concrete, steel and interface.

Material	Elasticity	Failure
Concrete	$E_c = 28$ GPa $\nu_c = 0.2$	Tension softening according to Hordijk [37] $f_t = 2.5$ MPa $G_f^I = 100$ J/m <sup>2</sup>
Steel	$E_s = 200$ GPa	$f_y = 400$ MPa
Interface	$k_n = 1.0 \times 10^6$ * N/mm <sup>3</sup> $k_t = 79.17$ N/mm <sup>3</sup>	$\tau_u = 4.75$ MPa

\* This value is assumed constant, even when slipping occurs.

scheme.

Each part of the model has been assigned a nonlinear constitutive law, see Figure 6.18. The adopted relations and the accompanying material properties (see Table 6.6) are based on a numerical study of the same tension-pull specimen carried out by Rots [56]. For the concrete we assumed Hordijk's tension softening relation of Equation (2.22). Figure 6.18a shows the corresponding saw-tooth approximation with 100 saw-teeth that was realized using the improved band width ripple concept which gives  $p_1 = 2.101 \times 10^{-2}$  and  $p_2 = 2.214 \times 10^{-2}$ . We assumed a uni-axial elastic–perfectly plastic stress–strain relation for the rebar. The corresponding saw-tooth law in Figure 6.18b was set up with the band width ripple concept of Subsection 3.1.3 taking  $p = 0.025$ . For the bond–slip model Rots [56] employed a nonlinear relation proposed by Dörr [17]. For simplicity's sake, we have used the bi-linear relation shown in Figure 6.18c. The corresponding saw-tooth law was also set up with the original band width ripple concept again taking  $p = 0.025$ .

The boundary conditions and the loading scheme were as follows. The rebar was supported in the vertical direction over the full length. In this way, we ensured the specimen to remain straight throughout the analysis. Also the horizontal displacement at the rebar's left end was restrained. We loaded the RC specimen by pulling the right end of the rebar. Through the interface between rebar and concrete, the load was partially transferred to the concrete.

### 6.3.2 Analysis without material imperfections

This subsection presents the SLA results of the homogeneous RC specimen presented in the previous subsection. We have tried to run this model with incremental–iterative analysis as well, but unfortunately we did not succeed due to convergence issues. This is attributed to cracking that occurs at many integration points simultaneously due to the homogeneous stress state of the virgin specimen resulting in bifurcations and numerical instability. Moreover, the structural response of this type of models generally shows strong snap-backs which makes it difficult to trace

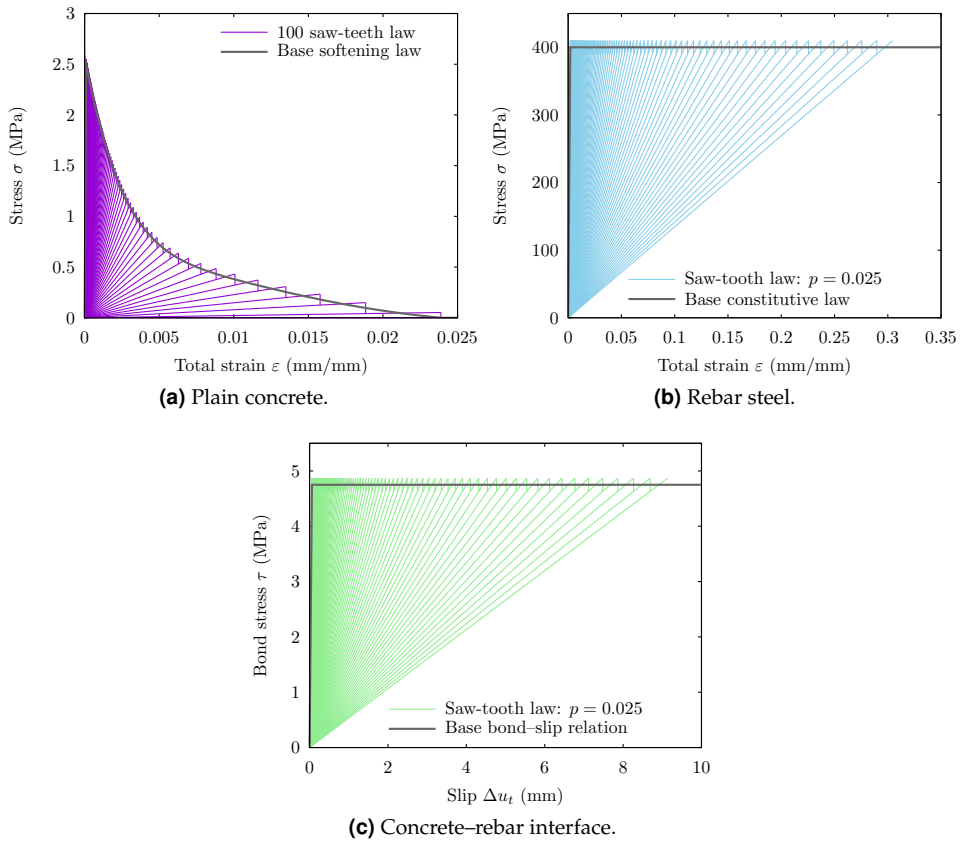


**Figure 6.18** Three nonlinear constitutive relations including their saw-tooth approximations adopted for the tension-pull analysis.

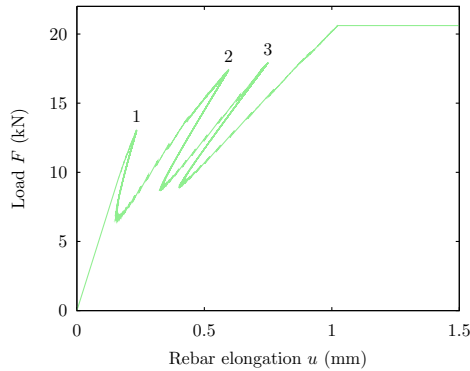


**Figure 6.19** Load–rebar elongation diagram of the homogeneous RC specimen obtained with SLA.

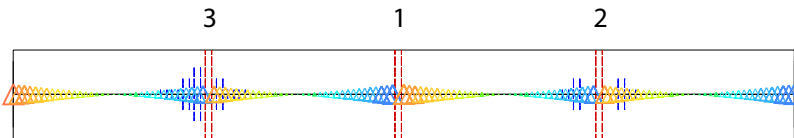


**Figure 6.20** Crack pattern and slip (indicated with triangles) between the concrete and the rebar for the homogeneous RC specimen obtained with SLA at 1.0 mm rebar elongation.

the global behavior. As we will show the SLA approach does not suffer from these problems, since for each cycle it automatically selects the most critical integration point, even when multiple integration points are about to crack. In this way it avoids bifurcations.

Figure 6.19 shows the load–rebar elongation diagram obtained with SLA adopting 10 850 cycles. Note that first three local peaks had to be overcome before the ultimate load is attained. Then the reinforcement bars start to yield. Also note that we have found three strong snap-backs without using some advanced arc-length scheme. Each snap-back corresponds to the initiation of a strain localization. Subsequently the new crack propagates over the depth of the specimen and fully develops just before the next local peak load is found. Eventually, three primary cracks have been developed.

The labels ‘1’ to ‘3’ in Figure 6.20 indicate the order of crack appearance. Note that the three localizations constitute the fully developed crack pattern, since no new localizations arise between the existing ones once the ultimate load is attained. Also note that the crack spacing is obtained automatically and that we did not have to “help” the algorithm in this respect, e.g. by pre-defining weakened cross-sections. In the same figure the absolute amount of slip between the concrete and the rebar is indicated by the size of the triangles. As expected, the largest slip values are found near the localizations and the ends of the specimen.



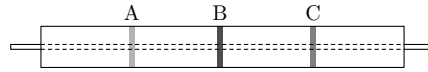


**Figure 6.21** Three predefined material imperfections at locations A, B, and C.

**Table 6.7** Reduced material properties at the predefined weakened cross-sections.

Location	Reduced tensile strength* $f_{t,\text{red}}$ (MPa)	Reduced fracture energy† $G_{f,\text{red}}^I$ (J/m <sup>2</sup> )
A	2.375	90.25
B	2.125	72.25
C	2.25	81.0

\* The value of  $f_t$  from Table 6.6 has been reduced by a factor 0.95, 0.85, and 0.90 at locations A, B, and C, respectively.

† The value of  $G_f^I$  from Table 6.6 has been reduced by the square of the reduction factor applied to the tensile strength.

The results of this simulation demonstrate the strengths of SLA: the quasi-brittle response of the considered RC specimen is captured effectively and no special techniques had to be employed to find the structural snap-backs. This is in line with a discussion on bifurcation issues by Rots et al. [60]. Also note that the combination of three physically nonlinear phenomena (i.e. smeared cracking, bond-slip behavior and yielding of reinforcement) works well with SLA.

### 6.3.3 Analyses with material imperfections

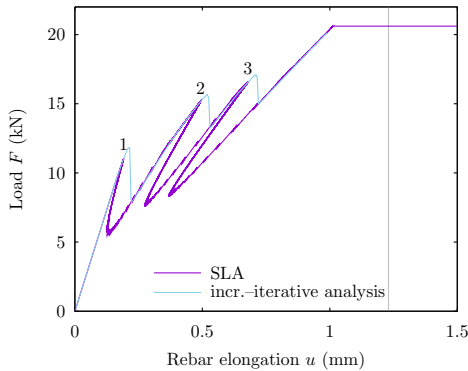
To compare SLA-based results with results from an incremental-iterative analysis, we have examined the same RC tension-pull specimen and added three predefined weakened cross-sections. The material imperfections are intended to help the incremental-iterative approach to find strain localizations. Figure 6.21 shows the locations of the weakened cross-sections. Note that they coincide with the crack locations found in the previous subsection. Table 6.7 provides the values of the reduced tensile strength  $f_{t,\text{red}}$  and fracture energy  $G_{f,\text{red}}^I$  that we have adopted at these locations.

Table 6.8 shows the analysis settings adopted for the incremental-iterative analysis. We have chosen to run the analysis using displacement control to “jump” over the expected structural snap-backs and hence avoid the accompanying numerical difficulties. Alternatively, the analysis could be run using arc-length control which makes it possible to capture the snap-backs. Good results obtained with this approach have been reported by Rots [56]. Since we are less interested in exactly reproducing the structural snap-backs with incremental-iterative analysis, we have decided to use the simpler displacement-controlled approach for our analysis.

The light blue line in Figure 6.22 shows the structural response obtained with

**Table 6.8** Analysis settings adopted for the incremental-iterative analysis.

Step sizes	0.005 (300)
Iteration scheme	Modified Newton–Raphson Maximum number of iterations per load step: 50
Convergence criteria	Force tolerance: $1.0 \times 10^{-3}$ Displacement tolerance: $1.0 \times 10^{-3}$ Energy tolerance: $1.0 \times 10^{-6}$
Line search algorithm	Upper bound on scale factor: $\eta_{\max} = 1$ Lower bound on scale factor: $\eta_{\min} = 0.1$ Terminating relative energy change: $\psi = 0.8$ Terminating interval length for Regula Falsi: $\Delta\eta = 0.1$ Maximum number of searches per iteration: 5

**Figure 6.22** Load–rebar elongation diagram of the inhomogeneous RC specimen obtained with SLA and incremental-iterative analysis.

incremental-iterative analysis. Converged parts of the equilibrium path have been drawn with solid lines, whereas non-converged parts have been drawn with dashed lines. Note that non-convergence only occurs just after a new crack was initiated. The analysis aborted with a divergence error just before the rebar started to yield. Figure 6.23a shows the obtained localizations. Like before, the numbers indicate the order of appearance.

The purple line in Figure 6.22 shows the load–rebar elongation diagram obtained with SLA and Figure 6.23b shows the corresponding crack pattern. Also here the slip between the concrete and the rebar has been indicated with triangles. Again the size of the triangles is proportional to the absolute amount of slip. After approximately 1.0 mm of rebar elongation, the steel that bridges the crack at location B starts to yield and the ultimate load of the specimen is attained.

Figure 6.24 shows the plastic strain distribution along the rebar at 1.5 mm elongation. The steel stresses at locations A and C remain just under the yield stress,

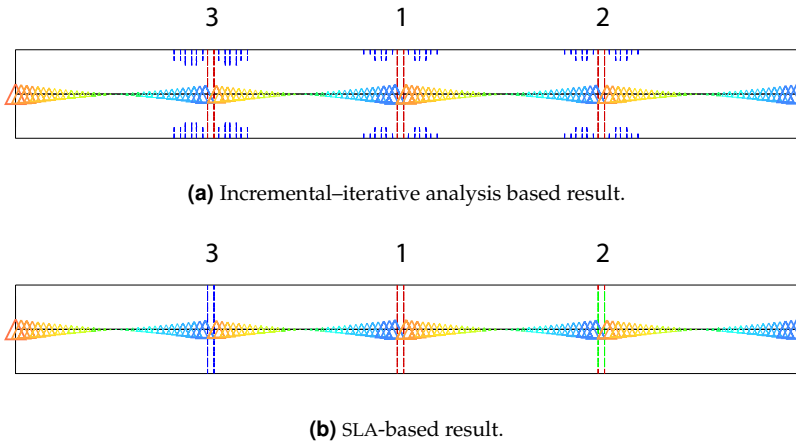


**Figure 6.23** Crack pattern and slip (indicated with triangles) between the concrete and the rebar for the RC specimen with pre-defined weakened cross-sections at 1.0 mm rebar elongation.

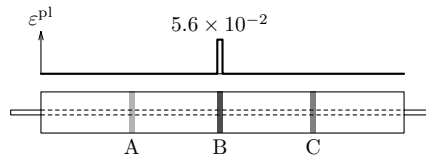


**Figure 6.24** Plastic strain distribution along the rebar at 1.5 mm rebar elongation.

thus no plastic strains are found there. Note that yielding of the rebar starts at a lower elongation level than if we would consider the rebar alone. The latter can be calculated from the steel parameters, assuming a uniform deformation of the rebar:  $u_y = (f_y/E_s)\ell = (410 \text{ MPa}/200\,000 \text{ MPa})600 \text{ mm} = 1.23 \text{ mm}$  (mind the stress overshoot typical for SLA). The gray line in Figure 6.22 indicates this elongation level. However, for the considered tension-pull specimen, the deformation along the rebar is non-uniform: yielding only occurs at location B which results in a smaller rebar elongation when the ultimate load is attained.

## 6.4 Masonry specimen with Coulomb friction and non-proportional loading

This section verifies the two saw-tooth approximations that we have developed for the Coulomb friction model in Chapter 4. For this purpose we will use a small pre-compressed masonry specimen that is loaded in shear. To deal with the non-proportional loading we employed the second double load multiplier strategy from Section 5.4. Subsection 6.4.1 presents the adopted finite element model. Then

**Table 6.9** Brick and mortar properties.

Material	Elasticity
Clay brick	$E_b = 16.7$ GPa
	$\nu_b = 0.15$
Mortar	$E_m = 2.974$ GPa
	$\nu_m = 0.15$

Subsection 6.4.2 shows the numerical results obtained with the uncoupled formulation from Section 4.2. In a similar way Subsection 6.4.3 verifies the numerical results obtained with the coupled formulation from Section 4.3.

### 6.4.1 Finite element model

Figure 6.25a shows the experimental set-up of the shear test conducted by Van der Pluijm [53]. The masonry specimen consists of two clay bricks (or “units”). Each clay brick is 200 mm long, 50 mm deep, and 100 mm thick, and they are joined by a 15 mm thick mortar layer. Table 6.9 shows the brick and mortar properties. In our numerical simulations we only modeled the masonry specimen and not the steel frame to which the specimen was attached (Figure 6.25b). Furthermore, we adopted the simplified micro-modeling strategy [14, 44] which means that the mortar layer is reduced to a zero-thickness interface, whereas the units are equally extended to retain the specimen depth of 115 mm.

We lumped the nonlinear material behavior into the joint, whereas for the extended bricks we employed linear-elastic behavior (see Table 6.10). For our numerical analyses, we adopted the material properties provided by Van der Pluijm [53], complemented with data from a numerical study by Shieh-Beygi and Pietruszczak [66]. We based the interface normal stiffness  $k_n$  on the Young’s moduli  $E_u$  and  $E_m$  of the unit and mortar, respectively, and the mortar thickness  $t_m$ , using the following formula [44]

$$k_n = \frac{E_u E_m}{t_m (E_u - E_m)} \quad (6.1)$$

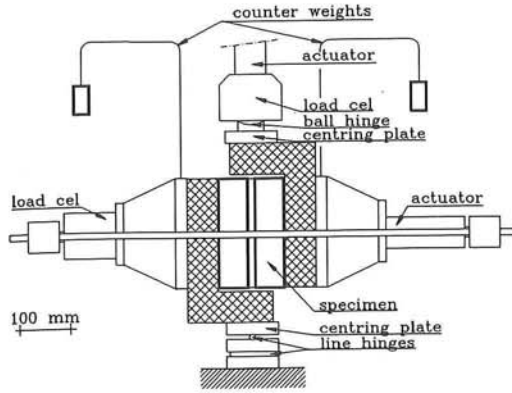
resulting in  $k_n = 241 \text{ N/mm}^3$ . In a similar way, we computed the interface shear stiffness  $k_t$  based on the shear moduli  $G_u$  and  $G_m$  of the unit and mortar, respectively, and the mortar thickness  $t_m$ , through the following expression [44]

$$k_t = \frac{G_u G_m}{t_m (G_u - G_m)} \quad (6.2)$$

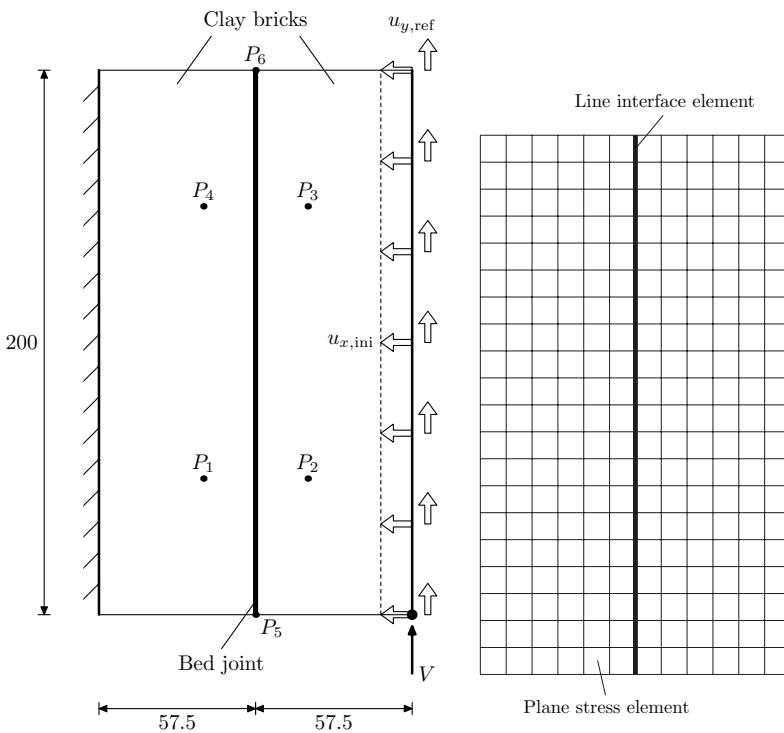
with the shear moduli

$$G_u = \frac{E_u}{2(1 + \nu_u)} \quad \text{and} \quad G_m = \frac{E_m}{2(1 + \nu_m)} \quad (6.3)$$

resulting in  $k_t = 105 \text{ N/mm}^3$ .



(a) Experimental set-up [53].



(b) Mechanical model (dimensions in mm).

(c) Finite element mesh.

**Figure 6.25** Pre-compressed masonry specimen loaded in shear.

**Table 6.10** Material properties assigned to the numerical model [53, 66].

Component	Elasticity	Coulomb friction
Extended unit	$E_u = 16.7^*$ GPa $\nu_u = 0.15^*$	None
Zero-thickness joint	$k_n = 241$ N/mm <sup>3</sup> $k_t = 105$ N/mm <sup>3</sup>	Exponential cohesion-softening $c_0 = 0.88^*$ MPa $\tan \phi = 0.75$ $G_f^{\text{II}} = 0.058 - 0.13\sigma$ N mm/mm <sup>2</sup>

\* Data taken from Shieh-Beygi and Pietruszczak [66].

Our computational model assumes plane stress conditions. The regular mesh consists of quadratic plane stress elements, representing the extended units, and quadratic interface elements which represent the joint. The plane stress elements have been numerically integrated using a  $2 \times 2$  Gaussian scheme, whereas for the interface elements a 4-point Newton-Cotes scheme was adopted.

The two load cases have been applied non-proportionally. First, the specimen has been loaded in compression through a prescribed uniform displacement  $u_{x,\text{ini}}$  along the right edge. Subsequently, a prescribed shear displacement  $u_{y,\text{ref}}$  was superimposed on the same edge. The size of the initial load case determines the level of compression. In our simulations, we adopted prescribed displacements  $u_{x,\text{ini}}$  of  $1.096 \times 10^{-3}$  mm,  $5.478 \times 10^{-3}$  mm, and  $1.096 \times 10^{-2}$  mm to achieve mean normal stress levels of  $-0.1$  MPa,  $-0.5$  MPa, and  $-1.0$  MPa, respectively. To account for the non-proportional loading we will adopt the second strategy from Section 5.4.

## 6.4.2 Uncoupled formulation

This subsection verifies the uncoupled formulation proposed in Section 4.2. We start by presenting the results of three analyses, each corresponding to a different level of pre-compression. For these analyses we have adopted a saw-tooth discretization parameter  $a_t = 0.025$ . Later in this subsection we will explore the effect of larger values of  $a_t$  for the case  $\sigma = -0.5$  MPa.

**Confinement variation** Figure 6.26a shows the development of the mean shear stress  $\tau_m$  for three levels of compression as a function of the mean shear displacement  $\delta_m$  obtained with SLA. We calculated the mean shear stress  $\tau_m$  as the quotient of the applied shear force  $V$  and the interface area  $A$  of  $100 \text{ mm} \times 200 \text{ mm}$ . To resemble the experimental results as closely as possible, we determined the mean shear displacement  $\delta_m$  as the average of the displacement differences  $\delta_1$  and  $\delta_2$ . We calculated the displacement difference  $\delta_1$  by subtracting the vertical displacement at point  $P_3$  from the one at point  $P_1$  (see Figure 6.25b). Similarly, displacement difference  $\delta_2$  was based on the vertical displacements at points  $P_2$  and  $P_4$ . After attaining the peak value, the shear stress decreases due to cohesion softening. As

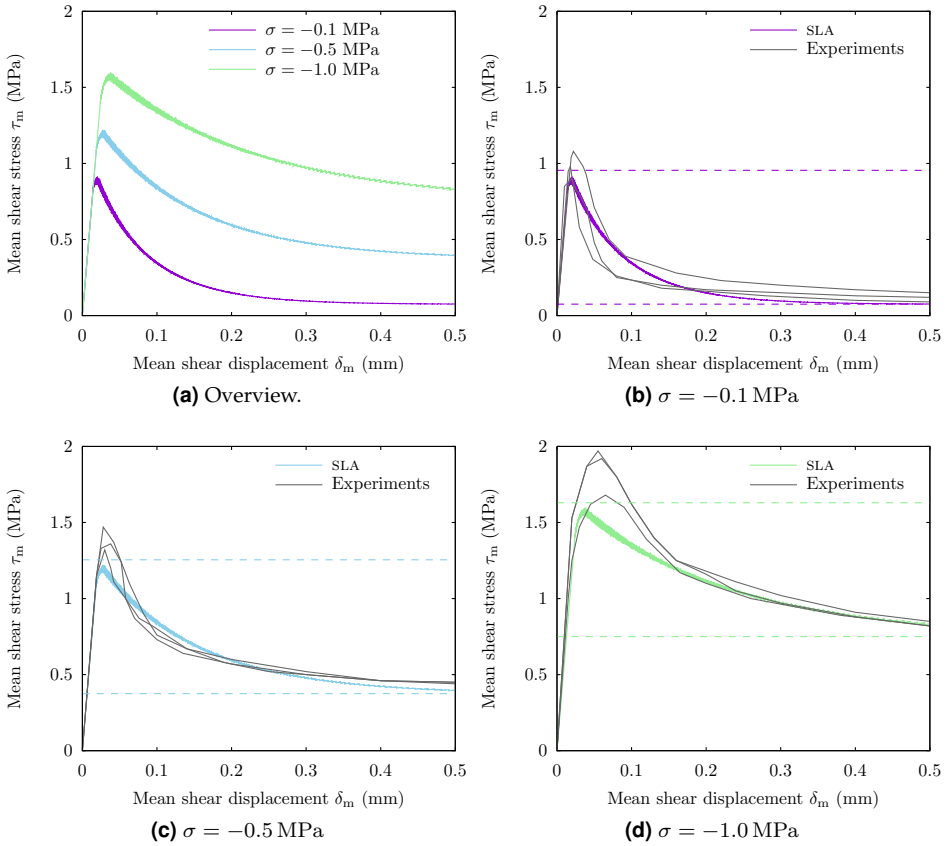


**Figure 6.26** Mean shear stress–shear displacement diagram of the shear test for different levels of pre-compression. The SLA results have been obtained with the uncoupled formulation and  $a_t = 0.025$ .

soon as the cohesion has fully softened, the residual shear resistance is determined entirely by dry friction. Note that for lower compressive stresses a more brittle behavior is found. We can explain that from the shear fracture energy  $G_f^{\text{II}}$  which is assumed a linear function of the normal stress  $\sigma$  across the interface. Unsurprisingly, the peak stress as well as the residual shear stress increase upon increasing confinement.

Figures 6.26b- 6.26d display the individual results once more along with the experimental results, the theoretical maximum shear stress, and the expected residual capacity. Note that the numerical simulations were able to capture the experimentally observed phenomena of softening and a residual shear resistance for larger shear displacements. The theoretical maximum shear stress is determined by considering full cohesion and dry friction:  $\tau_{\text{max}} = c_0 - \sigma \tan \phi$ . For the resid-

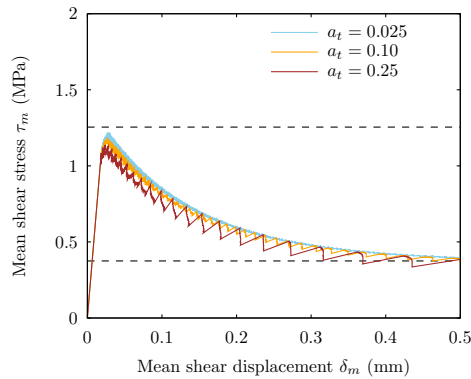


**Figure 6.27** Mean shear stress–shear displacement curves of the masonry test obtained with SLA using the uncoupled formulation and  $\sigma = -0.5$  MPa for three different values of  $a_t$ .

ual shear resistance we only need to consider dry friction:  $\tau_{\text{res}} = -\sigma \tan \phi$ . These two values have been indicated with dashed lines in all three diagrams. Note that most experimental curves show peak stresses exceeding the theoretical maximum. This might be explained by dilatancy: in case of a non-smooth fracture surface additional compressive stresses are introduced due to restrained uplift. In turn, the higher confinement level results in a larger shear capacity. Note that this effect is not taken into account by the uncoupled formulation.

Since the numerical results match the experimental ones quite well, we conclude that the proposed uncoupled formulation works as intended. Moreover, the obtained results show that the suggested non-proportional loading strategy is effective.

**Variation of discretization parameter** To demonstrate that moderately large values of  $a_t$  still produce acceptable results, we have performed two additional simulations. Both analyses have been based on a compressive stress  $\sigma = -0.5$  MPa. For the first simulation we have adopted  $a_t = 0.10$  and for the second one  $a_t = 0.25$ . Figure 6.27 presents the resulting mean shear stress–mean shear displacement curves, including the earlier obtained graph for  $a_t = 0.025$ . Most notably, the curves become less smooth upon increasing  $a_t$ . However, the peak stress and post-peak behavior are still in line with our previous result. Thus to save computational costs when analyzing large-scale structures a relatively large value for  $a_t$  still delivers acceptable results.

### 6.4.3 Coupled formulation

The numerical simulations in this subsection have been carried out with the coupled formulation presented in Section 4.3. Recall that this formulation accounts for dilatancy, but that it cannot consider cohesion softening. It takes a specified



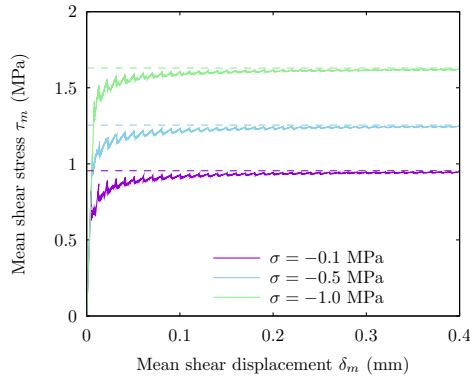


**Figure 6.28** Mean shear stress–shear displacement diagram of the shear test for different levels of pre-compression. The results have been obtained with the coupled formulation,  $\tan \psi = 0$  and  $\Delta u_n = \Delta u_t = 0.01$  mm.

relative displacement increment vector as input. For the first series of analyses we will take  $\Delta u_n = \Delta u_t = 0.01$  mm and we set  $\tan \psi = 0$  to check whether it correctly accounts for the confinement level. Subsequently we will present two analyses that employ different values for the dilatancy coefficient, to check whether the shear resistance continues to increase upon increasing shear displacement (dilatancy softening is not taken into account). Finally we will present the results of three additional analyses to investigate the effect of the specified relative displacement increment vector.

**Confinement variation** The mean shear stress–mean shear displacement diagram in Figure 6.28 reflects the absence of cohesion softening and dilatancy. The mean shear displacement  $\delta_m$  in this graph (but also in the other diagrams in this subsection) is based on the average of the relative shear displacements at positions  $P_5$  and  $P_6$  (see Figure 6.25b). Since we have set  $\tan \psi = 0$ , no additional compressive stresses are built up and thus no additional shear resistance was found. The ultimate shear resistance for large shear displacements was determined with the following formula:  $\tau_u = c_0 - \sigma \tan \phi$ . For each pre-compression level the corresponding ultimate shear stress has been indicated with a dashed line. Note that the effect of the normal stress which acts at the interface is as expected: for larger compressive stresses a larger shear resistance was found.

**Variation of dilatancy coefficient** To check whether the coupled formulation correctly captures the effects of dilatancy, we have run two additional analyses: one with  $\tan \psi = \frac{1}{2} \tan \phi = 0.375$  and one with  $\tan \psi = \tan \phi = 0.75$ . For both analyses we adopted  $\sigma = -0.5$  MPa. Figure 6.29 shows the resulting  $\tau_m$ – $\delta_m$  curves. Note that contrary to our previous simulations with the coupled model, now we observe a continuously growing shear stress. The reason is that the uplift of the

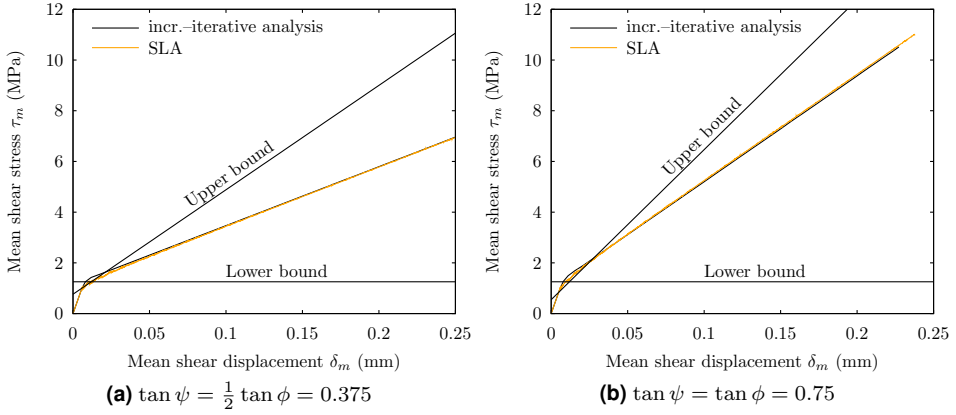


**Figure 6.29** Mean shear stress–shear displacement curves of the shear test for different values of  $\tan \psi$ . The SLA results have been obtained with the coupled formulation and  $\Delta u_n = \Delta u_t = 0.01$  mm

joint cannot freely occur due to the adjacent bricks. In other words, the plastic normal displacement that would occur due to dilatancy is partially restrained, resulting in an elastic normal displacement in opposite direction. That elastic normal displacement results in an increase of the compressive stress and hence leads to a larger shear stress. Unsurprisingly, the growth rate of the mean shear stress is related to the dilatancy coefficient  $\tan \psi$ .

The diagrams also show that the SLA solutions comply with analytically established upper and lower bound solutions. The upper bound solution is based on the assumption of infinitely stiff bricks, which implies that any uplift of the bed joint is fully restrained. That is, we assume that any plastic normal deformation is counteracted by an equal elastic normal deformation in opposite direction. Then, the development of the normal stress  $\sigma$  as a function of the shear displacement  $\delta$  reads

$$\sigma(\delta) = \sigma_0 - k_n u_n^{\text{pl}} \quad (6.4a)$$

$$= \sigma_0 - k_n u_t^{\text{pl}} \tan \psi \quad (6.4b)$$

$$= \sigma_0 - k_n \left( u_t - \frac{\tau}{k_t} \right) \tan \psi \quad (6.4c)$$

with  $\sigma_0$  being the initial normal stress. Next, we substitute the above expression of the normal stress in the Coulomb failure criterion:

$$\tau = c_0 - \sigma(\delta) \tan \phi \quad (6.5a)$$

$$= c_0 - \left( \sigma_0 - k_n \left( u_t - \frac{\tau}{k_t} \right) \tan \psi \right) \tan \phi \quad (6.5b)$$

By rearranging terms we have found the following explicit relation between shear

stress  $\tau$  and shear displacement  $\delta$ :

$$\tau(\delta) = \frac{k_t}{k_t + k_n \tan \psi \tan \phi} (c_0 - (\sigma_0 - k_n \delta \tan \psi) \tan \phi) \quad (6.6)$$

Note that this expression assumes that the Coulomb failure criterion is met, i.e. it is valid only for ongoing plasticity. The analytical lower bound is based on plastic normal deformations which are free to occur. In other words, we assume that the bricks have no stiffness at all. In that case, no additional normal stresses are induced and thus no extra shear capacity is gained. Hence, the lower bound solution is represented by the horizontal line  $\tau = c_0 - \sigma_0 \tan \phi$ .

To complete the verification, we have also run the same computational models with an incremental–iterative scheme. Figure 6.29 includes the resulting mean shear stress–mean shear displacement curves which match the ones obtained with SLA.

**Variation of discretization parameters** We conclude this subsection by presenting the results of three analyses that consider different specified relative displacement increment vectors. Since the previous variation study showed relatively smooth curves obtained with SLA, we have decided to consider a coarser discretization only. We expect that taking a finer discretization will yield results that hardly differ from the previous ones. These are the considered combinations:

- $\Delta u_n = 0.10$  mm and  $\Delta u_t = 0.01$  mm
- $\Delta u_n = 0.01$  mm and  $\Delta u_t = 0.10$  mm
- $\Delta u_n = 0.10$  mm and  $\Delta u_t = 0.10$  mm

For the analyses presented here we adopted  $\sigma = -0.5$  MPa and  $\tan \psi = \frac{1}{2} \tan \phi = 0.375$ .

From the resulting mean shear stress–mean shear displacement relations in Figure 6.30a we notice that all curves tend to converge to the earlier obtained curve using  $\Delta u_n = \Delta u_t = 0.01$  mm (drawn with orange lines in Figure 6.30). However, when we zoom in at small mean shear displacements we find considerable differences when a relatively large value of  $\Delta u_t$  was adopted, as illustrated by Figures 6.30c and 6.30d. This could probably be explained by the small ratio between the shear displacement  $u_t$  and the specified relative shear displacement increment  $\Delta u_t$ .

## 6.5 Conclusions

This chapter presented verification and sensitivity studies of improvements and extensions of SLA introduced earlier in the present work. The examined case studies involved four different material models: discrete and smeared crack models,

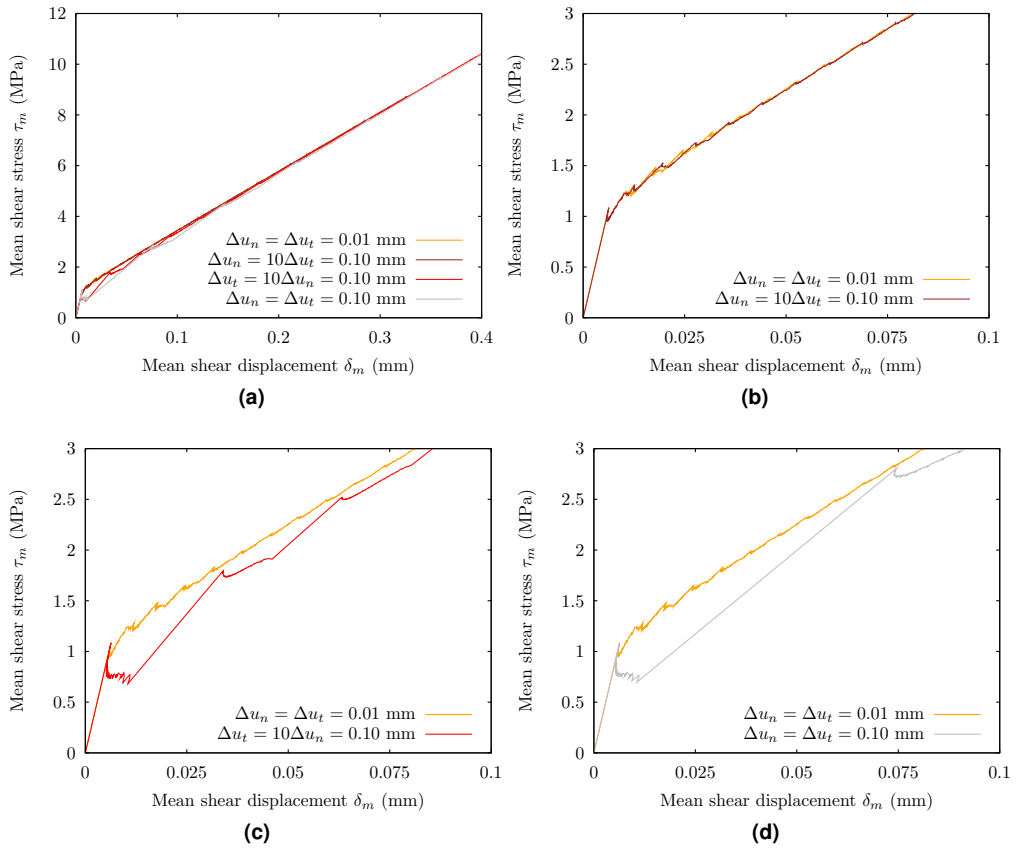


**Figure 6.30** Mean shear stress–mean shear displacement curves of the shear test for different presumed relative displacement increment vectors. The results have been obtained with the coupled formulation,  $\tan \psi = \frac{1}{2} \tan \phi$  and  $\sigma = -0.5$  MPa.

a bond–slip model and the Coulomb friction model. The final case study also included non-proportional loading.

In conclusion we can say that in general the proposed improvements and extensions are effective. More specifically, we draw the following conclusions:

- The improved band width ripple concept introduced in Section 3.2 showed a limited sensitivity with respect to mesh refinement. In particular for discrete crack models, the results proved virtually objective in terms of peak load and post-peak behavior. For smeared crack models we observed a small increase in post-peak capacity which may be attributed to a more diffuse crack pattern near the compressive zone. Possibly, the incorporation of a crack-tracking technique eliminates this spurious dependency.
- We demonstrated that the investigated saw-tooth approximations are nearly objective with respect to damage increment refinement, at least for moderately small damage increments. By refining the damage increments, we obtained a smoother structural response which eases the interpretation of local snaps and jumps.
- We showed that SLA can effectively cope with a snap-back at constitutive level which may occur in smeared crack analysis, by adopting a special type of saw-tooth approximation. This is particularly relevant for materials with extremely brittle properties and/or practical finite element models with relatively large elements.
- The analysis of a RC tensile test demonstrated that SLA does not require the use of imperfections to aid crack localizations. Localized failure occurs automatically due to the scaling of single events.
- We verified that both suggested stepwise approximations of the Coulomb friction model are able to capture the effect of the normal stress on the shear resistance. Moreover, we demonstrated that the uncoupled model adequately incorporates cohesion softening, whereas the coupled model effectively reproduced the dilatancy effect.
- The masonry shear example showed that the second double load multiplier strategy for non-proportional loading works well.

## Chapter 7 Validation and application

The previous chapter verified sequentially linear analysis (SLA) and the stepwise secant approximations that we developed for nonlinear constitutive models by analyzing the response of relatively small structural components. Furthermore, we demonstrated that the numerical results were only slightly affected by variations in mesh size and/or damage increment size.

This chapter validates SLA by examining two more complex case studies and it shows some results of two more applications. The first case study, presented in Section 7.1, concerns a pre-compressed masonry wall loaded in shear. The performed numerical analysis features non-proportional loading and the uncoupled Coulomb friction model (i.e. zero dilatancy) combined with discrete cracking. Section 7.2 presents a case study on a 1/10<sup>th</sup> scaled masonry façade that is subjected to self-weight and tunneling-induced settlements. This case study involves non-proportional loading as well as smeared cracking. Section 7.3 briefly revisits two other case studies that have been carried out in collaboration with other researchers: a reinforced glass beam and a reinforced concrete (RC) slab.

### 7.1 Pre-compressed masonry shear wall

The case study in this section concerns the numerical simulation of a pre-compressed masonry shear wall which was tested experimentally by Raijmakers and Vermeltoort [54] and Vermeltoort and Raijmakers [71]. The objective of the performed analysis is to assess whether SLA is capable of reproducing the phenomena observed in the experiment.

**Finite element model** Figure 7.1 shows the geometry and non-proportional loading scheme of our model which was inspired by the one adopted by Lourenço [45]. The wall was built with 18 courses. All DOFs of the nodes along the bottom edge of the lower course were restrained. The shear wall was initially loaded by a top load of 30 kN that compresses the wall. The nodes along the top edge of the upper course were given an initial vertical displacement  $u_{y,ini}$  of 0.083 mm to simulate this load (we determined the imposed displacement through a preliminary linear analysis). Subsequently, we apply a prescribed reference displacement  $u_{x,ref}$  to the top edge nodes. Hence, the imposed boundary conditions prevent rotations of the

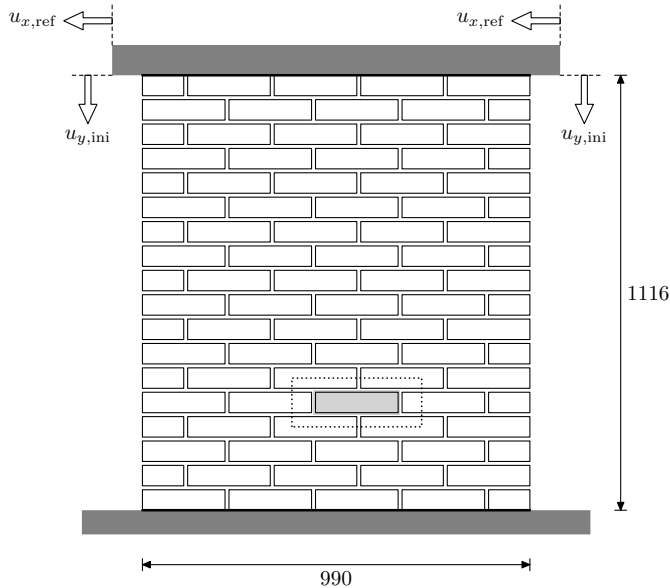


**Figure 7.1** Shear wall geometry and non-proportional loading scheme. The dimensions are in mm. Figure 7.2 provides details of the masonry modeling.

top and bottom edges of the wall. This has been indicated with thick black lines in Figure 7.1.

For the numerical representation of the masonry we adopted the simplified micro-modeling strategy [14, 44]. The mortar joints and the mortar–brick interface were collectively lumped into a zero-thickness interface. Consequently, the bricks needed to be extended to compensate for the mortar thickness (Figure 7.2a). In the experiment, the wall consisted of bricks with dimensions of 210 mm  $\times$  52 mm  $\times$  100 mm and the mortar layers were 10 mm thick. Using the micro-modeling approach the extended bricks in the numerical model had dimensions of 220 mm  $\times$  62 mm  $\times$  100 mm. Also, potential vertical brick cracks were included at mid-brick length to allow full bricks to break into two parts.

Figure 7.2b shows that the mesh was built up using eight-noded quadratic plane stress elements for the “extended” bricks and six-noded quadratic interface elements for the mortar joints and the potential brick cracks. One full brick was divided in four continuum elements over the length and two over the depth. At mid-brick length, interface elements were inserted to allow for a vertical crack inside the brick. The continuum elements were integrated using a  $2 \times 2$  Gauss scheme whereas for the interface elements a 3-point Newton-Cotes scheme was used.

In the numerical model all physically nonlinear behavior was lumped into the interface elements. We distinguished two kinds of interfaces: those representing the mortar joints and those representing the potential brick cracks. For the mortar

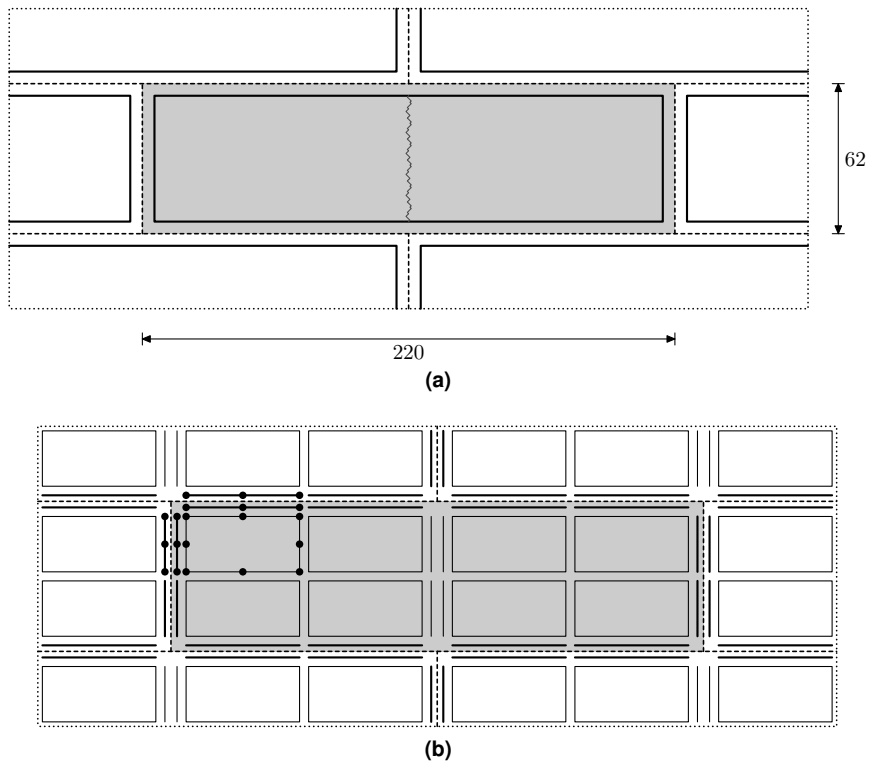


**Figure 7.2** Close-up of an "extended" brick (dimensions are in mm). (a) The mesh consists of a repetitive pattern of plane stress and line interface elements (b).



**Table 7.1** Material parameters of the head and bed joints [45, 54, 71, 14].

Elasticity		Tension cut-off		Coulomb friction	
$k_n = 82$	N/mm <sup>3</sup>	$f_t = 0.25$	MPa	$c_0 = 0.35$	MPa
$k_t = 36$	N/mm <sup>3</sup>	$G_f^I = 18$	J/m <sup>2</sup>	$\tan \phi = 0.75$	
				$G_f^{II} = 125$	J/m <sup>2</sup>

**Table 7.2** Material parameters of the bricks and the potential brick cracks [45, 54, 71, 14].

Bricks		Potential brick cracks			
Elasticity		Elasticity		Tension cut-off	
$E = 16.7$	GPa	$k_n = 1.0 \times 10^6$	N/mm <sup>3</sup>	$f_t = 2.0$	MPa
$\nu = 0.15$		$k_t = 1.0 \times 10^6$	N/mm <sup>3</sup>	$G_f^I = 80$	J/m <sup>2</sup>

joints we followed the suggestion from CUR 171 [14] to adopt  $\tan \psi = 0$ . This enables us to use the tension–shear failure criterion of Section 4.4. Recall that this failure criterion combines the uncoupled Coulomb friction model (including cohesion softening) with a tension cut-off. Compressive failure is not taken into account. For the Coulomb friction contour we adopted a discretization factor  $a_t = 0.05$  (see Equation (4.4)) and for the tension cut-off we assumed a linear tension softening relation approximated by a saw-tooth diagram with  $N = 15$ . Table 7.1 lists the adopted material parameters of the head and bed joints. We modeled the potential brick cracks using the discrete crack approach. A saw-tooth law consisting of 40 saw-teeth was set up to approximate the exponential tension softening relation. Table 7.2 gives the material parameters of the potential brick cracks. It also lists the properties of the linear-elastic bricks.

**Analysis results** Figure 7.3 compares the numerically obtained lateral load–lateral displacement curve with the experimental ones. Observe that the numerical result resembles the experimental ones well. Also the ultimate load predicted with SLA is reasonably close to the experimental value. Note from the red line segments in Figure 7.3 that for a number of analysis steps it was not possible to fully apply the initial load case. Figure 7.4 indicates those steps with a red dot. Nevertheless, we consider the numerical result acceptable, demonstrating that the suggested strategy for non-proportional loading in Section 5.4 works. Since we did not take into account compressive failure, we have abandoned the analysis results as soon as the maximum compressive stress in the joints exceeded the assumed compressive strength  $f_c$  of the material ( $f_c = 10.5$  MPa).

Also the numerical damage evolution followed the experimental description relatively close. Initially, two horizontal cracks developed: one near the upper left corner of the wall and another one near the bottom right corner (Figures 7.5a and 7.5b). Both cracks propagated towards the other side of the wall. However, at a certain moment these cracks were arrested and a staircase-like crack arose,

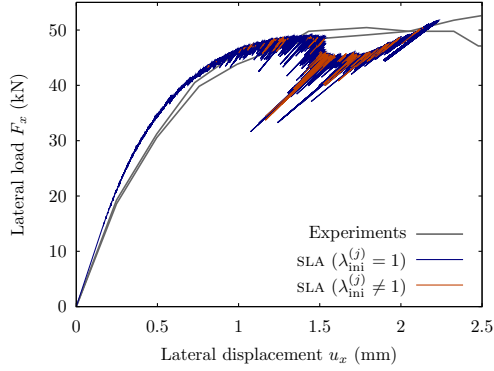


**Figure 7.3** Lateral load–lateral displacement diagram of the masonry shear wall.

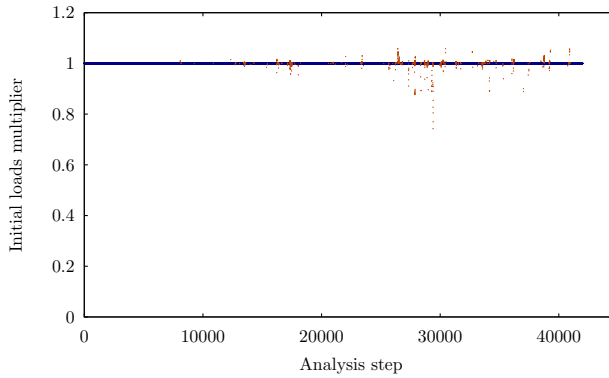


**Figure 7.4** Evolution of the load multiplier applied to the initial loads throughout the simulation with SLA.

starting from the wall's center (Figures 7.5c and 7.5d). At that loading stage, also several bricks started to break.

Another way to illustrate the damage evolution, is to keep track of the damage variables  $d_n$  and  $d_t$ . The damage variable  $d_n$  in normal direction is defined as

$$d_n = 1 - \frac{k_n}{k_{n,0}} \quad (7.1)$$

with  $k_n$  and  $k_{n,0}$  the reduced and initial normal stiffnesses, respectively. A similar definition holds for the damage variable  $d_t$  in tangential direction, except for using the reduced and initial shear stiffnesses  $k_t$  and  $k_{t,0}$ , respectively. Note that both damage variables vary from 0 (no damage) to 1 (full damage). For a lateral displacement of 0.5 mm, Figures 7.6a and 7.6b show in which joints the normal and shear stiffnesses were reduced. The size and color of the triangles indicate how severe the damage is. Note that at this early loading stage, the damage in normal direction ( $d_n$ ) is limited to the two horizontal cracks, whereas the damage in tangential direction ( $d_t$ ) is also visible in other parts of the wall. Also observe for the two horizontal cracks that the damage in tangential direction went ahead of the damage in normal direction. This implies that the bed joint first slipped and then opened up. Figures 7.6c and 7.6d display how the damage has progressed at 1.5 mm lateral displacement. Here we noticed that around the wall's center, the damage in normal direction was limited to the head joints, whereas damage in tangential direction is visible in both the head and bed joints. The reason is that a reduction in normal stiffness is always accompanied by a reduction in shear stiffness, whereas the opposite is not necessarily true. However, we verified that once some of the bed joints opened up, also the normal stiffness of those joints was reduced.

In the experiment also the development of the resulting vertical reaction force  $V$  was measured, providing yet another way to validate the numerical results. Figure 7.7a displays the evolution of the vertical reaction force  $V$  as a function of the lateral displacement  $u_x$ . Although the result with SLA shows the same trend as the experimental result (which is an increase of the vertical reaction force upon an increasing lateral displacement) the numerically obtained size is generally lower than what was measured experimentally. This could possibly be explained by the absence of the dilatancy effect in the numerical simulation. If that effect would have been taken into account, the arisen plastic normal displacements would be counteracted by elastic normal displacements since the wall is confined in normal direction. As a result, the compressive stresses would increase, leading to a larger vertical reaction force. However, the result in Figure 7.3 seems to contradict this explanation. Since the shear capacity increases when larger compressive stresses are present, we would expect the numerically obtained shear load to be smaller than the experimental one. Yet we found a good agreement between the experimental and numerical relations.

Also the development of the eccentricity of the vertical reaction force  $V$  with respect to the wall's center line was monitored during the experiment. The eccen-

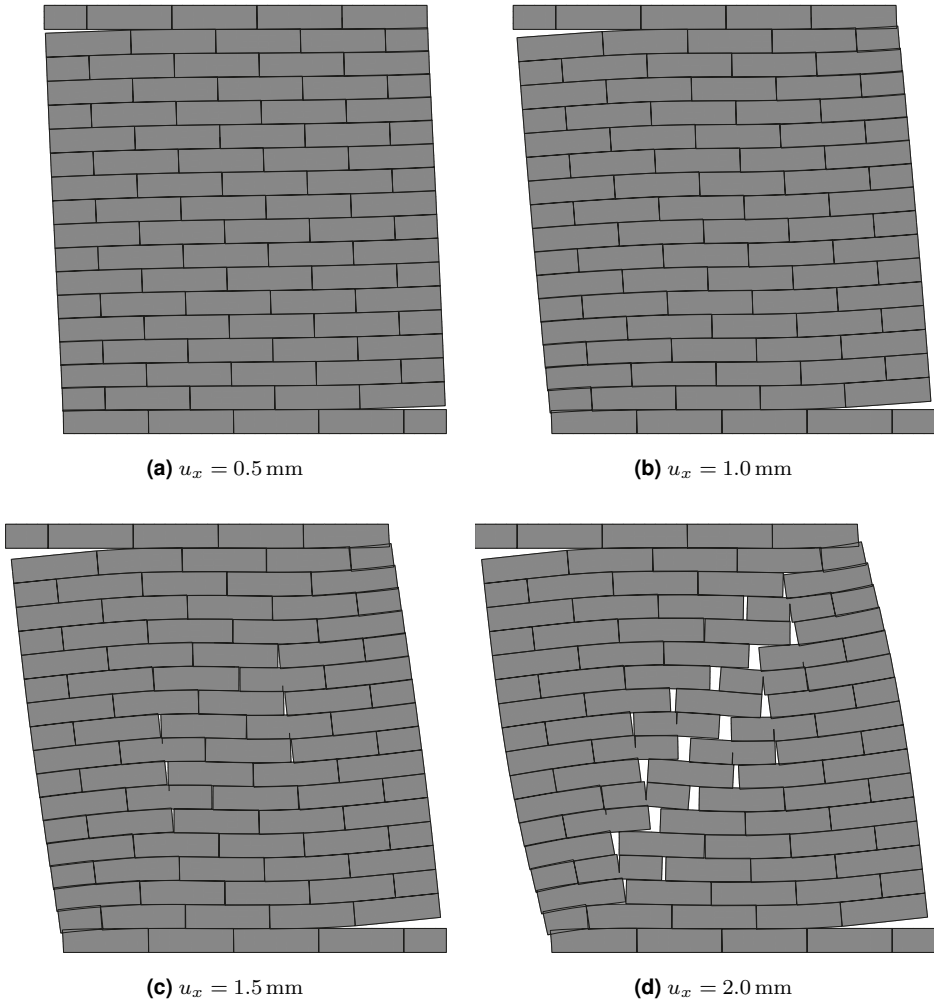


**Figure 7.5** Deformed meshes of the shear wall analysis at different lateral displacements  $u_x$ . Deformations have been magnified with a factor 100.

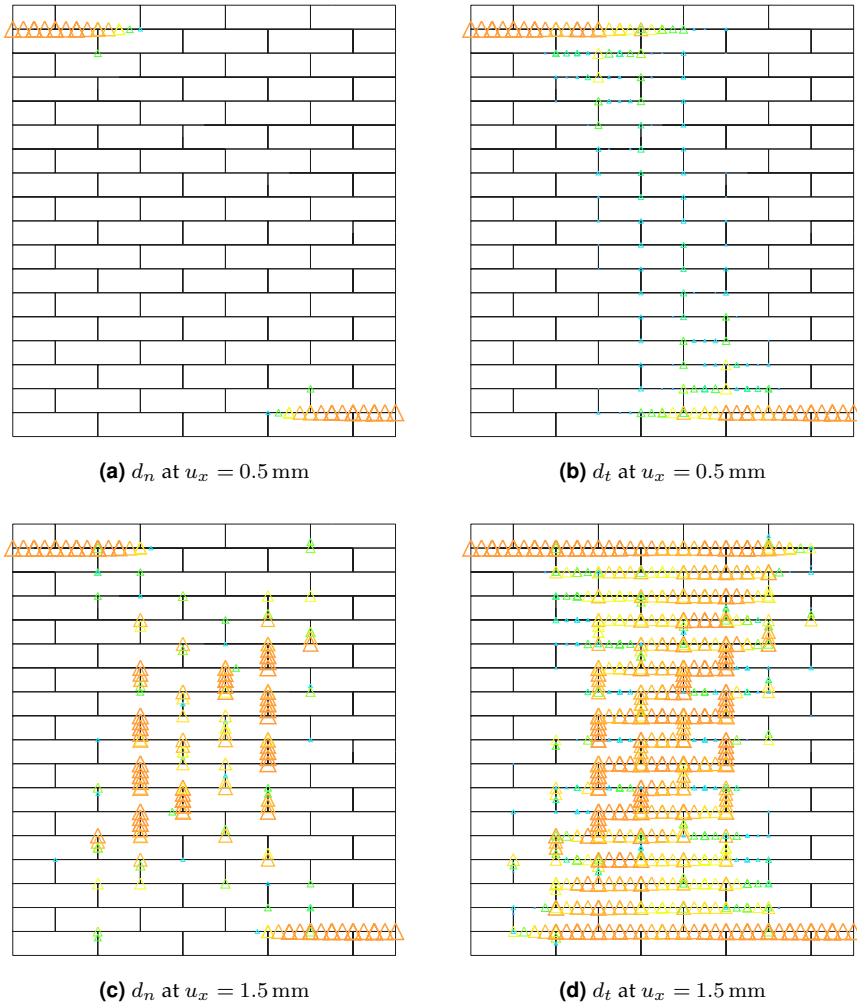


**Figure 7.6** Damage variables  $d_n$  and  $d_t$  in normal and tangential directions, respectively, for different lateral displacements  $u_x$ .

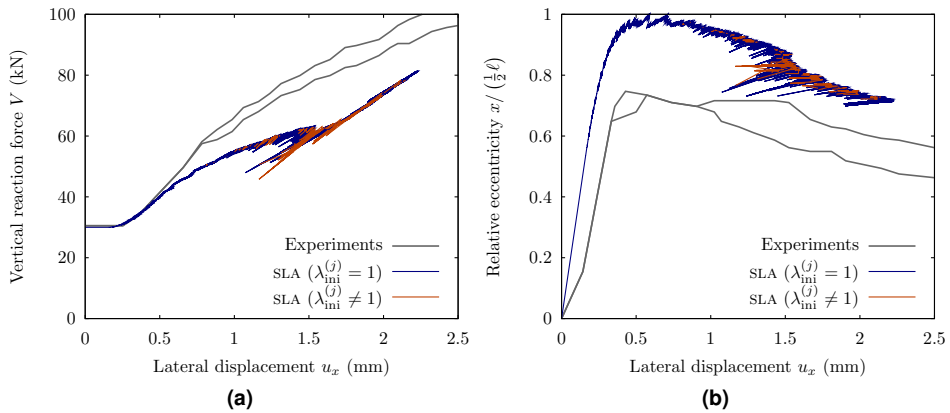


**Figure 7.7** Vertical reaction force and its eccentricity as function of the lateral displacement  $u_x$ .

tricity is expressed as the quotient  $x / (\frac{1}{2}\ell)$  with  $x$  the distance between the point of application of the vertical reaction force and the wall's center line, and  $\ell$  the width of the wall. Figure 7.7b compares the experimentally obtained relations with the numerical result. Again, we observe a similar trend, although the difference between the relations is larger than what we would expect based on the matching load–displacement curves in Figure 7.3.

In conclusion we can say that the uncoupled Coulomb friction model and the non-proportional loading strategy proved effective in simulating the shear wall's behavior. Despite the numerous possible failure mechanisms of the examined shear wall, SLA enabled us to reasonably reproduce the experimentally observed behavior. In particular the load–displacement diagram and crack pattern evolution showed good agreement with experimental data. We emphasize that the performed numerical analysis was stable and the number of analysis steps that involved scaling of initial load was limited (Figure 7.4). Nevertheless, the numerical analysis results had to be abandoned as soon as the compressive stresses in the joints exceeded the anticipated compressive strength, since no compressive failure criterion was included. In order to properly continue the simulation beyond this point, a compressive failure criterion needs to be added to the adopted composite failure criterion. It is not clear to what extent the inclusion of dilatancy effects would affect the numerical results. To examine that, the coupled model of Section 4.3 should be extended with a tension cut-off. This has not been devised yet.

## 7.2 Scaled masonry façade

In the introduction of this thesis we noted that for the numerical prediction of cracks in masonry buildings subjected to settlements induced by underground

**Table 7.3** Dimensions  $h_1, h_2, l_1, l_2$  and  $l_3$ , and nodal forces  $F_1$  to  $F_{10}$  applied to the façade [24].

Dimension (mm)	Nodal forces (N)	
$l_1 = 84$	$F_1 = 230$	$F_6 = 469$
$l_2 = 126$	$F_2 = 296$	$F_7 = 195$
$h_1 = 106$	$F_3 = 319$	$F_8 = 498$
$h_2 = 218$	$F_4 = 392$	$F_9 = 304$
$h_3 = 108$	$F_5 = 358$	$F_{10} = 467$

construction, a robust solution procedure is indispensable. In the present section we examine a scaled masonry façade that was experimentally tested by Giardina, Marini, Hendriks, Rots, Rizzardini, and Giuriani [23]. A numerical study of the scaled façade, including a simulation with SLA, was performed by Giardina et al. [24]. This section presents the numerical results of that study obtained with SLA.

Figure 7.8 shows the geometry of the  $1/10^{\text{th}}$  scaled masonry façade which is 1428 mm wide, 1186 mm deep and 50 mm thick. The openings in the façade represent the locations of windows and doors. Wooden lintels, which have been indicated with a dark gray fill color in the figure, support the masonry directly above the openings. The façade was built on top of a 10 mm thick rubber bedding which in turn rests on a 1700 mm long steel beam. The bedding represents the soil–structure interaction. At the right hand end, the beam is fully supported over a length of 115 mm, to simulate a fully clamped edge. At the left hand side and below the right hand door, roller supports have been placed. Since out-of-plane failure did not occur in the experiment and as the thickness of the façade is limited, we assumed a plane stress state. Therefore, in our computational model we used quadratic plane stress elements to model the masonry, lintels and steel beam adopting a  $2 \times 2$  Gauss integration scheme. For the bedding we used quadratic line interface elements with the default 4-point Newton-Cotes integration scheme [50].

The façade was loaded in a non-proportional fashion by three loads in two subsequent phases. In the first phase, which we will call the initial loading phase, we loaded the structure by its self-weight and a number of nodal forces. The nodal forces were meant to take into account the increase in gravitational load due to the downsizing of the model [23]. In the experiment, these additional forces were transferred to the façade through steel bars. At the locations of the steel bars, bricks were removed as shown in Figure 7.8. Table 7.3 gives the magnitude of the nodal forces and the mass densities  $\rho_m$ ,  $\rho_w$  and  $\rho_s^*$  of the masonry, wood and steel, respectively. The density of the steel was modified to account for a different shape of the beam cross-section that was used for the numerical analysis. We will explain this in detail later in this section. In the second loading phase, we superimposed a settlement by lowering the leftmost roller support resulting in a hogging shape of the steel beam.

For the masonry, which is heterogeneous by nature, we adopted a constitutive

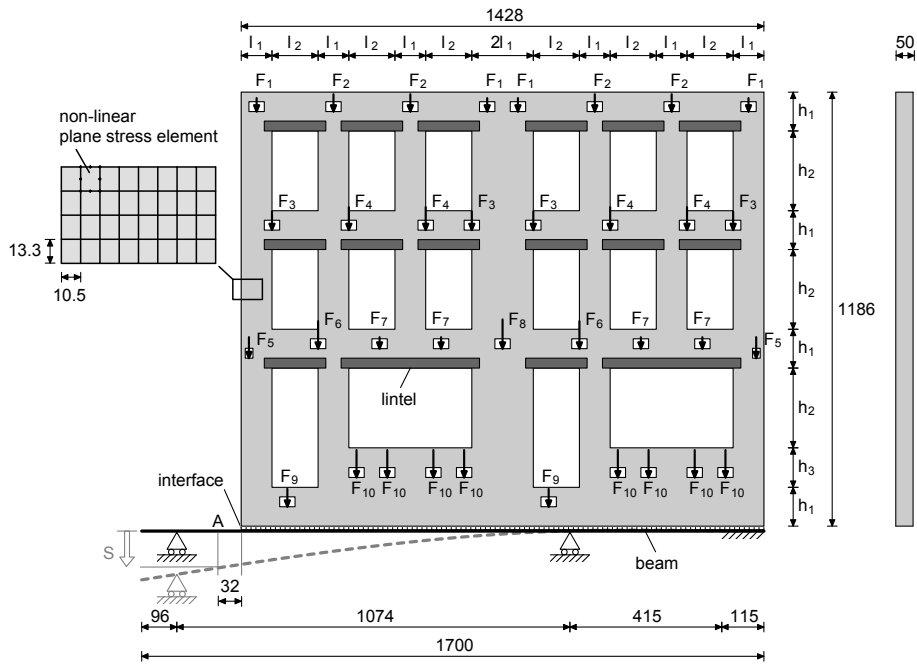


Figure 7.8 Model of the 1/10<sup>th</sup> scaled masonry façade [23]. All other dimensions are in mm.



**Table 7.4** Material parameters adopted for the numerical simulation of the masonry façade [24].

Component	Elasticity	Tension cut-off
Masonry	$E_m = 3$ GPa	$f_{t,m} = 0.1$ MPa
	$\nu_m = 0.2$	$G_f^I = 10$ J/m <sup>2</sup>
	$\rho_m = 1900$ kg/m <sup>3</sup>	
No-tension bedding	$k_n = 0.7$ N/mm <sup>3</sup>	$f_{t,b} = 1.0 \times 10^{-9}$ MPa
	$k_t = 1.0 \times 10^{-9}$ N/mm <sup>3</sup>	
Wood	$E_w = 10$ GPa	
	$\nu_w = 0.15$	
	$\rho_w = 500$ kg/m <sup>3</sup>	
Steel	$E_s^* = 37.92^\dagger$ GPa	
	$\nu_s = 0$	
	$\rho_s^* = 1354^\ddagger$ kg/m <sup>3</sup>	

<sup>†</sup> We adapted the Young's modulus of the steel ( $E_s = 210$  GPa) to account for the modified beam cross-section, as explained in the text.

<sup>‡</sup> We adapted the mass density of the steel ( $\rho_s = 7500$  kg/m<sup>3</sup>) to account for the modified beam cross-section, as explained in the text.

law in terms of average strain and stress, thereby smearing out the differences between the bricks and the mortar. The experimental façade was built using bricks that were 40 mm wide, 25 mm deep and 50 mm thick. The mortar layers had an average thickness of 2 mm. Table 7.4 contains the adopted values of the homogenized Young's modulus  $E_m$  and Poisson's ratio  $\nu_m$  of the masonry [24]. We modeled the inelastic behavior of the masonry using the smeared fixed crack approach with a variable shear retention relation according to Equation 2.16. Figure 7.9 shows the assumed linear tension softening relation and the corresponding saw-tooth law that was set up adopting 15 saw-teeth.

The no-tension bedding that supports the masonry façade was modeled with line interface elements. Since the adopted SLA implementation cannot handle a material that has zero tensile strength, we assigned it a very low dummy tensile strength. The saw-tooth law consisted of a single saw-tooth. That is, as soon as the normal traction attains the dummy tensile strength, the normal and shear stiffnesses are fully reduced. The elastic stiffnesses  $k_n$  and  $k_t$  as well as the dummy tensile strength are to be found in Table 7.4.

The wooden lintels as well as the steel beam were assigned linear-elastic properties only. For our numerical simulation, we converted the properties of the I-shaped cross-section of the beam used in the experiment to an equivalent solid rectangular one for our numerical simulation. Since the thickness of our plane stress model was dictated by the thickness of the masonry, we adopted the same thickness for the modified steel beam:  $t_b^* = 50$  mm. We determined the modified beam depth  $h_b^*$  and Young's modulus  $E_s^*$  of the steel from the requirements that the bending stiffness  $E_s^* I_b^*$  as well as the extensional stiffness  $E_s^* A_b^*$  of the modified beam cross-section should be identical to those of the original I-shaped

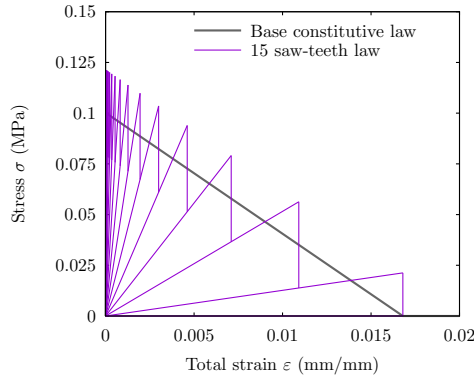


**Figure 7.9** Assumed linear tension softening relation of the masonry and the 15 saw-teeth approximation for the façade analysis.

cross-section:

$$E_s I_b = E_s^* I_b^* = \frac{1}{12} E_s^* t_b^* (h_b^*)^3 \quad (7.2a)$$

$$E_s A_b = E_s^* A_b^* = E_s^* t_b^* h_b^* \quad (7.2b)$$

with  $E_s$ ,  $I_b$  and  $A_b$  the Young's modulus, moment of inertia and cross-sectional area, respectively, of the I-shaped cross-section. For the modified beam, these quantities are denoted by starred versions. The original beam was 60 mm deep and had 50 mm wide flanges. The flanges as well as the web had a thickness of 5 mm. Assuming a Young's modulus  $E_s$  of 210 GPa, we were able to compute the bending stiffness  $E_s I_b$  and the extensional stiffness  $E_s A_b$ . Using the above requirements we determined the modified beam depth  $h_b^*$  and Young's modulus  $E_s^*$  to be 83 mm and 37.92 GPa, respectively. Since the cross-sectional area  $A_b^*$  of the modified beam differs from the original one, we also adapted the mass density  $\rho_s$  of the steel, in order to find a similar mass per meter beam length. Table 7.4 shows the adopted parameters of the modified steel beam and the wooden lintels.

The crack pattern in Figure 7.10a shows that we have found a considerable number of micro-cracks at the end of the initial loading phase, although the maximum crack width is still very small (less than  $5 \times 10^{-2}$  mm). In fact, 2478 linear analyses were required to fully apply the initial loads consisting of the dead weight plus the nodal forces that account for the increased gravity load due to the downsizing of the façade. That is, we needed to apply 2478 damage increments in order to obtain a load multiplier  $\lambda_{ini}$  of 1. Note that at this loading stage no settlements were imposed yet. The large number of steps required for the initial loading phase may be attributed to the fineness of the mesh and the number of saw-teeth per integration point. Figure 7.11 illustrates the development of the load multiplier applied to the initial loads throughout the simulation. The blue points to the left of the gray line demonstrate the gradual application of the initial loads in the first

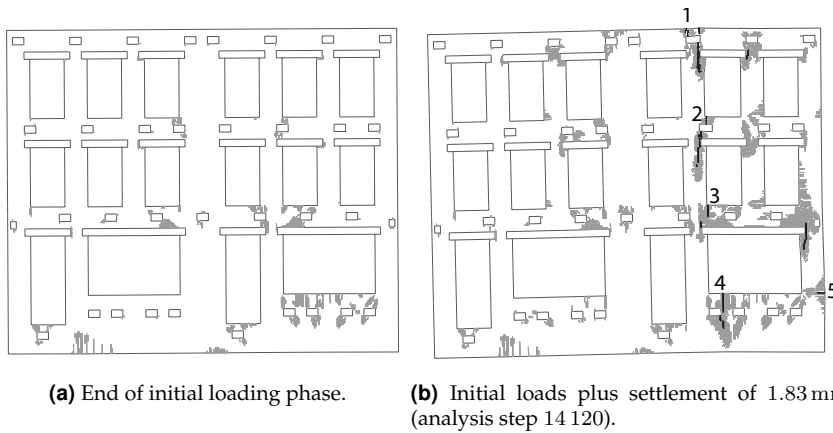


**Figure 7.10** Crack patterns obtained with the masonry façade analysis at two different load stages.

loading stage. Similar to what we have seen with other simulations, the loads do not increase monotonously but rather show a more snap-type development.

In the subsequent phase of the analysis, consisting of 22 522 analysis steps, we superimposed the settlements resulting in new cracks primarily located at the right hand side of the façade (Figure 7.10b). This is in line with the observations from the experiment [23]. The points to the right of the gray line in Figure 7.11 indicate the analysis steps which took into account combinations of initial loads and settlement. Note that for a considerable number of analysis steps we were unable to fully apply the initial loads. These analysis steps have been marked with a red dot. In all other analysis steps, the initial loads could be fully applied and they have been marked with a blue dot.

In the experiment, the vertical and horizontal displacement of dials B and C, respectively, have been monitored providing a way to validate the numerical results. Dial B was located 60 mm to the right of the upper left corner of the façade, whereas dial C was positioned 150 mm below that corner. The two displacements were monitored as a function of the vertical displacement of dial A, which is located along the top face of the steel beam at 30 mm to the left of the lower left corner of the façade. In the experiment, the displacements of dials A, B and C were monitored as soon as the settlement was applied. However, in our numerical simulation the corresponding nodes were already displaced due to the initial loads. Therefore, the displacements shown in the graphs have been corrected for this effect by subtracting the displacements of the dials at the end of the initial loading phase from the actual displacements. Figure 7.12a presents the evolution of the vertical displacement of dial B, whereas Figure 7.12b shows the development of the horizontal displacement of dial C. Note the reasonable agreement between the experimental and numerical results. Here, gray and light gray dots indicate

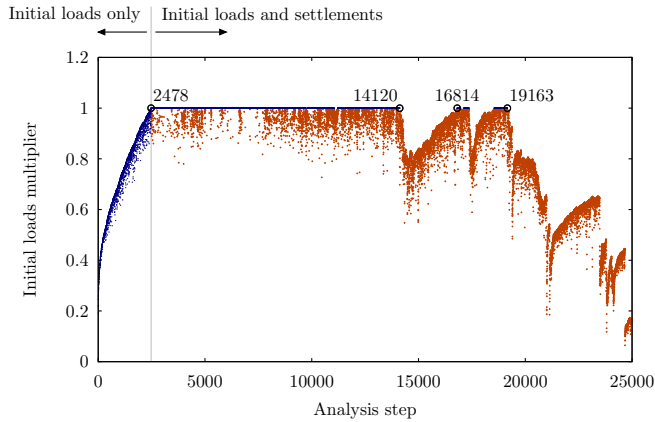
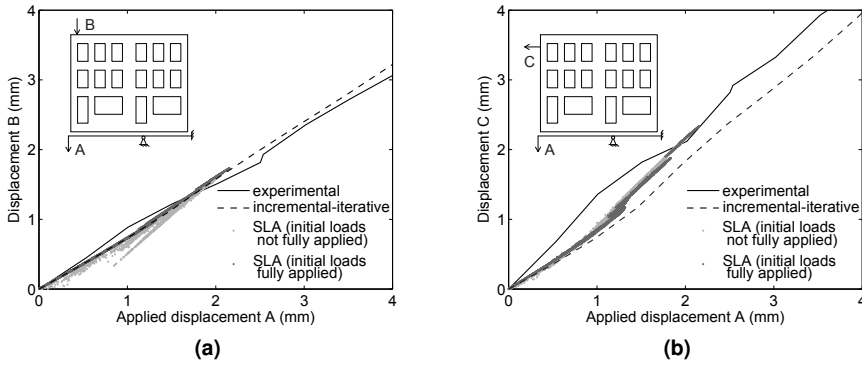


**Figure 7.11** Evolution of the load multiplier applied to the initial loads throughout the simulation with SLA. Note that for a considerable number of steps in the second loading phase, the initial loads could not be fully applied (indicated with red dots).

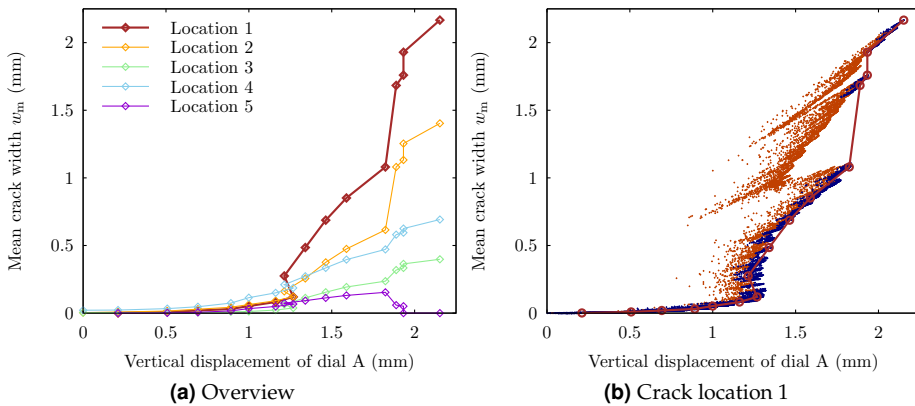
analysis steps in which the initial loads could be fully or only partially applied, respectively.

Figure 7.13a shows the crack width development at five active cracks labeled 1 through 5 in Figure 7.10b. The mean crack width  $w_m$  along the vertical axis was computed as the product of the mean crack strain (averaged over all cracked integration points of the element at the considered location) and the element crack band width  $h$ . The vertical displacement of dial A along the horizontal axis has the same meaning as in Figures 7.12a and 7.12b. For clarity, each line in Figure 7.13a has been constructed using only a few points from the actual response which consists of thousands of points. To demonstrate that the shown lines are a good representation of the obtained response, we have plotted all points corresponding to location 1 and the line from Figure 7.13a in one diagram (Figure 7.13b). The dots show once more the typical snap-type behavior associated with SLA. Again, a blue dot indicates an analysis step in which the initial loads were fully applied, whereas a red dot marks an analysis step in which this was not possible. The lines in Figure 7.13a reveal the typical behavior of unreinforced masonry buildings: initially the cracks grow fairly slow, but suddenly, some cracks open up rapidly.

Note that the crack at location 5 behaves differently compared to the cracks at the other locations. As soon as the other cracks open up rapidly, the crack at location 5 actually closes. This suggests that the upper right part of the façade breaks apart from the rest of the structure. The issue here is that the crack not just closes, but the load is effectively reversed from tension to compression. To demonstrate this effect, we have plotted in Figure 7.14 the evolution of the vertical stress  $\sigma_{yy}$ , the vertical total strain  $\varepsilon_{yy}$  and the damage variable  $d$  along a horizontal



**Figure 7.12** Evolution of the vertical and horizontal displacement of dials B and C, respectively, as a function of the vertical displacement of dial A.



**Figure 7.13** Crack width evolution at five different locations obtained with our numerical simulation of the masonry façade.

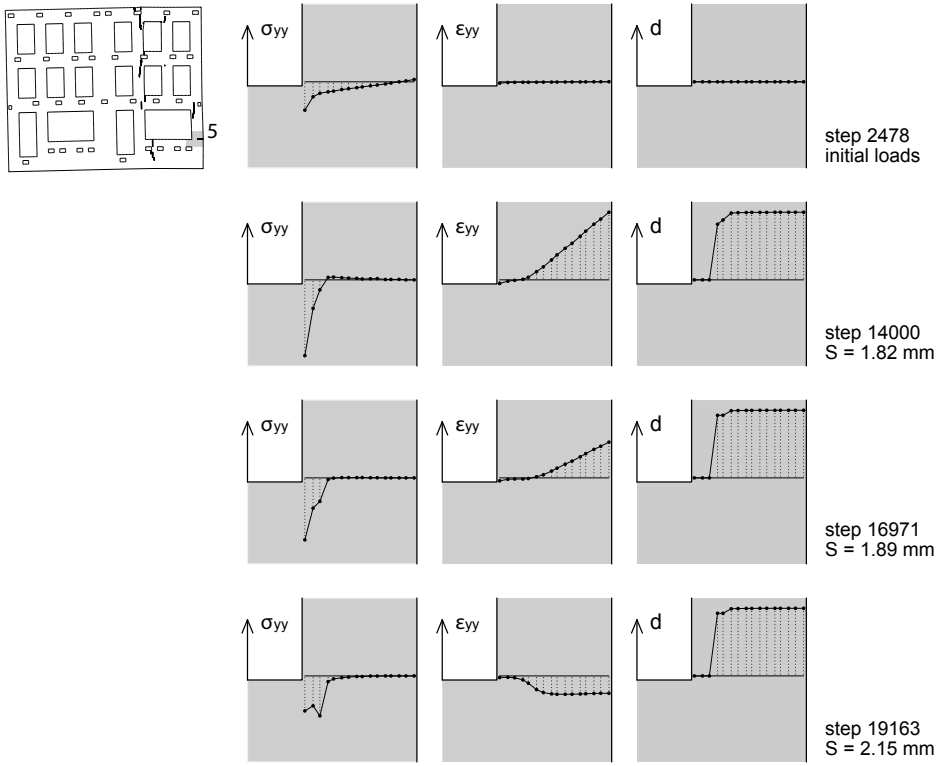
cross-section at location 5. The damage variable  $d$  was defined as

$$d = 1 - \frac{E_m}{E_{m;0}} \quad (7.3)$$

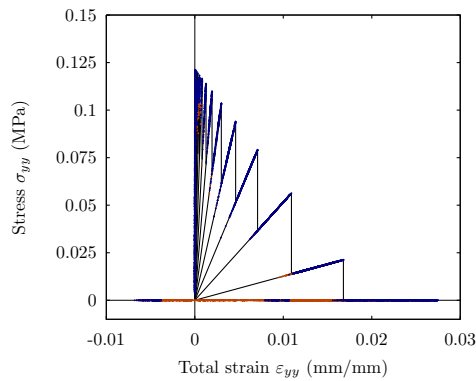
with  $E_m$  and  $E_{m;0}$  the reduced and initial Young's moduli of the masonry, respectively. The three plots in the top row of Figure 7.14 show  $\sigma_{yy}$ ,  $\varepsilon_{yy}$  and  $d$  at the end of the initial loading phase (analysis step 2478). Note that the material along the considered cross-section is still uncracked at this early loading stage. Just before the first major valley in Figure 7.11 is found (analysis step 14 120), the crack has progressed quite far, as shown by the second row of plots in Figure 7.14. This supports the conclusion that the crack at this location is to be attributed to the settlement load. However, after the first major valley in Figure 7.11 (at analysis step 16 814) the total strain  $\varepsilon_{yy}$  has decreased as demonstrated by the third row of plots, indicating crack closure. In fact, after 19 163 linear analyses we observe a negative total strain as shown by the last row of pictures, signifying that the loading is effectively reversed in the considered cross-section. However, the earlier arisen damage due to tensile failure affects the response in compression, for the material degradation in this area is still maintained. In other words, since the stiffness here has virtually vanished, there is hardly any resistance against the occurring deformation. The reason is that currently a proper crack closing algorithm has not been included in the SLA formulation. As a result, the initial loads that act at the part of the façade that broke apart from the rest of the structure can no longer be carried. Therefore, the load multiplier applied to the initial loads can no longer be maintained at a value of 1. This explains why we observe a descending trend in Figure 7.11 after step 19 163. A side effect is that the applied settlement also decreases. Recall that as soon as the initial loads can no longer be fully applied, we scale the last 'successful' combination of initial and reference loads.

Figure 7.15 supports the same conclusion, however presented in a different way. It shows the stress–strain history of the rightmost integration point along the considered cross-section at crack location 5. Blue dots indicate analysis steps in which the initial loads could be fully applied, whereas red dots mark analysis steps in which the initial loads were only partially applied. Note that due to the development of the crack virtually all stiffness has been lost at this integration point before the crack closes. However, upon load reversal the stiffness is not recovered as indicated by the dots which have a negative total strain  $\varepsilon_{yy}$ . In case a crack closing algorithm would be included a kink should be visible at the origin of the stress–strain relation.

In conclusion we can say that the simulation with SLA was numerically stable and the novel strategy for non-proportional loading was again successful. The presented results look promising with respect to analyses of large-scale masonry buildings, which are typically characterized by an even more brittle response that is difficult to trace using incremental-iterative techniques. Nevertheless, in order to properly follow crack closure and load reversal, the SLA formulation needs to be extended with a crack closing algorithm, e.g. following the lines devised by



**Figure 7.14** Evolution of stress  $\sigma_{yy}$ , total strain  $\epsilon_{yy}$  and damage variable  $d$  along a horizontal cross-section at location 5.



**Figure 7.15** Stress–strain history of the rightmost integration point along the considered cross-section for the masonry façade analysis.

Graça-e-Costa, Alfaiate, Dias-da-Costa, and Sluys [29] or Salam Al-Sabah and Laefer [62].

## 7.3 Reinforced glass beam and RC slab

This section presents the highlights of two more case studies that have been carried out in collaboration with other researchers and students. Firstly we will show some results of a study on the structural behavior of reinforced glass beams subjected to four-point bending. Subsequently, we will briefly present the results of a study on the structural behavior of a RC slab loaded by a concentrated force near one of the supports.

Several studies have been devoted to the numerical simulation of reinforced glass beams subjected to four-point bending that have been tested experimentally at Delft University of Technology [46, 47, 26]. Figure 7.16a shows a schematic representation of the experimental set-up. In this thesis, we will only present a few results of one particular beam type. The considered beam has a span of 1400 mm, it is 120 mm deep and 22 mm thick and the distance between the point loads is 400 mm. The applied mesh consisted of square elements having sides of 10 mm. Due to the brittle properties of glass, this element size resulted in a snap-back at constitutive level. Five saw-teeth were used to approximate the material law of glass, whereas for the steel ten saw-teeth were adopted. From the load–displacement diagram in Figure 7.16b we conclude that the numerical result obtained with SLA is in fairly good agreement with the experimental results, in particular the prediction of the ultimate load. The difference in initial stiffness is explained by the way the experiments have been conducted: in the first run the beams were loaded until the first glass fracture occurred. Then the beams were unloaded, and in the second run they were reloaded up to global failure. The experimental curves shown in the figure correspond to the second run. Figure 7.16c shows the stiffness distribution at 25 mm deflection which gives an impression of the expected crack pattern. Contrary to the V-shaped cracks observed in the experiment, the numerical simulation predicts T-shaped cracks. This could partially be explained by the adopted regular mesh consisting of square elements which may have a negative impact on the development of diagonal cracks. Also the number of occurring cracks in the numerical simulation is significantly larger than what was observed in the experiment. As the analysis assumed perfect bond between the glass and the reinforcement, the numerical results might be improved by accounting for a proper bond–slip relation. The overall conclusion is that SLA offers a promising perspective regarding the structural analysis of reinforced glass beams, especially considering the extremely brittle nature of glass.

Another application that illustrates the capabilities of SLA is the numerical simulation of a RC slab subjected to a concentrated load near one of the line supports. Figure 7.17a shows the experimental set-up of the slab (5.0 m long, 2.5 m wide and 0.30 m thick) representing a section of a continuous bridge. The examined slab



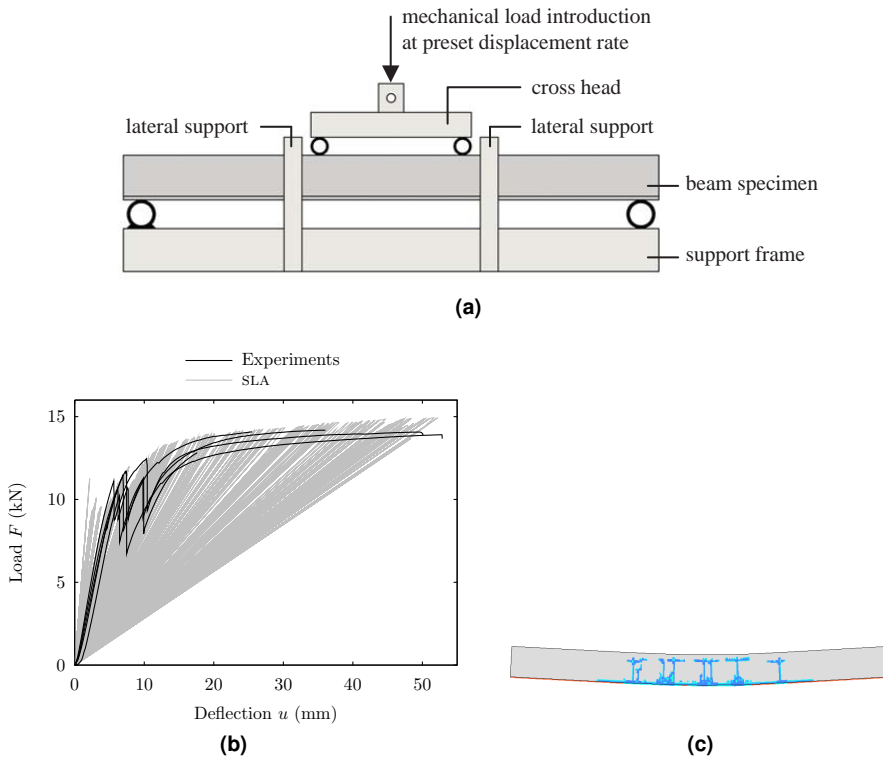


**Figure 7.16** (a) Experimental set-up of the four-point bending test. (b) Load–deflection curves and (c) crack pattern at 25 mm deflection. All figures obtained from Louter [47].

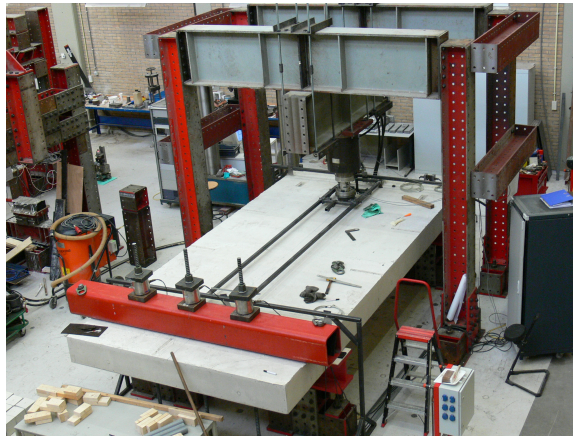
[41] was part of a research program that was carried out to determine the shear capacity of RC bridges. The slab was reinforced with bars running in longitudinal and transversal directions only. No stirrups were applied. For the numerical simulation, we have extended the SLA formulation towards three-dimensional stress states [72]. We adopted a fixed smeared crack approach and for simplicity's sake we assumed proportional loading. We modeled the slab with solid elements in order to allow for shear failure modes to occur. To limit the required computational effort, we adopted a coarse mesh and 12 saw-teeth to approximate the linearly assumed tension softening relation of the concrete. The numerical results are promising: Figure 7.17b shows that the obtained load–deflection curve matches the experimental one well, in terms of the curve envelope as well as the peak load. The deformed mesh at peak load in Figure 7.17c does not show clear punching shear failure nor wide beam shear failure, whereas for the experiment the latter was found [41]. Using an incremental-iterative scheme we found it difficult to obtain a properly converged solution which underlines the primary benefit of SLA.

## 7.4 Conclusions

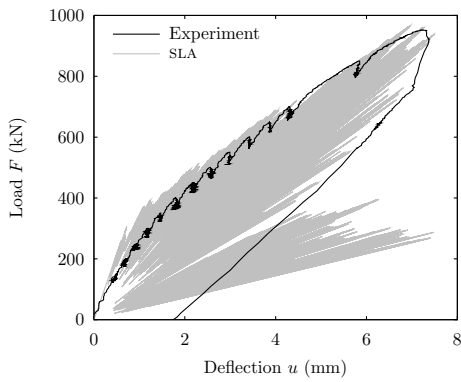
For the two extensively examined case studies, we demonstrated that the strategy for non-proportional loading proposed in Section 5.4 could be applied effectively. In particular the shear wall analysis showed that temporarily unloading the structure, i.e. by partially releasing the initial loads, allowed for a stable damage progression. It also revealed that the initial loads can be recovered after a number of analysis steps. These observations give us confidence that the suggested strategy also works for other cases.

The shear wall analysis also showed that SLA is capable of selecting the governing failure mechanism, even though the structure might fail in multiple ways. This can be explained from the fact that the reference loads are scaled with the lowest possible load multiplier leading to progressive damage. The inclusion of multiple nonlinear material laws is straightforward and does not complicate the numerical analysis. The results of the shear wall analysis also confirmed the effectiveness of the uncoupled Coulomb friction model.

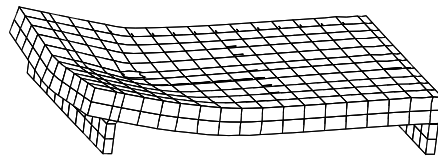
However, the investigated case studies also pointed out two future improvements of the SLA approach. We had to abandon the results of the shear wall analysis as soon as the compressive stresses in the joints attained the anticipated compressive strength. In order to continue the simulation with SLA beyond this point, we suggest to include a compressive failure criterion which can be handled in a similar way as the tensile failure criterion. The results of the masonry façade analysis revealed that non-proportional loading may lead to crack closure and subsequent load reversal. Without a proper crack closure algorithm this may cause the simulation to end prematurely. Thus, the inclusion of a crack closure algorithm is indispensable in case of extensive stress redistributions and subsequent unloading of cracks and reloading in reversed direction.



(a)



(b)



(c)

**Figure 7.17** (a) Experimental set-up of the RC slab test (picture by courtesy of E. Lantsoght). Numerical results: (b) load–deflection curve and (c) deformed mesh at peak load.

---

Finally, we briefly presented the highlights of two other case studies that involved SLA: a reinforced glass beam subjected to four-point bending and a RC slab loaded by a concentrated force near of the supports. Both application examples underlined the capability of SLA to simulate brittle failure in a robust manner.



## Chapter 8 Discussion and conclusions

In this work we have developed and validated three major extensions of the sequentially linear analysis (SLA) framework which improve the computational modeling of failure of quasi-brittle structures. In the first place, we have proposed an improved saw-tooth approach which ensures that the fracture energy is preserved with respect to the base tension softening law. Secondly, we have developed two distinct models to incorporate Coulomb friction in our numerical simulations using SLA. The final extension comprises a new strategy for non-proportional loading which provides an alternative way of taking the previous critical load into account when the current critical load multiplier is determined.

Section 8.1 briefly revisits the three major extensions of SLA proposed in the present work. Subsequently, Section 8.2 discusses the primary conclusions based on the numerical analyses that have been presented in the previous two chapters. Finally, in Section 8.3, we identify several issues that in our opinion need to be addressed by future research.

### 8.1 New developments

The following contributions to the existing SLA framework have been developed in this work:

1. An improved saw-tooth model based on the band width ripple concept by Rots et al. [61] has been proposed. Any tension softening saw-tooth law set up with the improved model meets two requirements. Firstly, the area enclosed by the saw-tooth law equals the area enclosed by the base tension softening curve, and secondly the ultimate crack width or crack strain of the saw-tooth law equals the one of the base tension softening curve. In addition, we have developed saw-tooth models for bond–slip relations and for stress–total strain laws which exhibit a linear snap-back at constitutive level, relevant for materials with extremely brittle properties and/or practical finite element models with relatively large elements.
2. We have developed two saw-tooth approximations to include a Coulomb friction model in numerical simulations with SLA. The first one is based on an uncoupled formulation and therefore it omits the dilatancy effect. Nonetheless, cohesion softening can be taken into account by this approximation. The

second approximation has its roots in plasticity theory and it does consider the dilatancy effect, resulting in a coupled formulation. This approximation does not include cohesion softening.

A major difference with conventional saw-tooth laws, which relate only one stress component to one deformation component, is that the saw-tooth laws for the Coulomb friction model cannot be set up in advance. The reason is that the Coulomb friction model relates two stress components to two deformation components in a way that is unknown in advance. Therefore, the instantaneous changes in the entries of the secant stiffness matrix as a result of the progressive damage are determined throughout the simulation using presumed displacement increments.

3. A new strategy for non-proportional loading has been introduced that is based on constrained optimization. Per integration point we formulate one or more constraints in terms of the load multiplier to enforce a stress state that does not violate the material law. In this way, we can identify per integration point a set of load multipliers that result in constitutively admissible stresses. Subsequently, we maximize the applied load by considering the load multiplier sets of all integration points simultaneously. However, at times conflicting load multiplier sets may be found which implies that temporarily no combination of the initial load case and some scalar multiple of the reference load case exists. In that case, we proportionally scale the most recent 'successful' combination of the initial and reference load cases. Consequently, the applied initial loading is temporarily changed. However, after a number of damage increments it may be recovered.

## 8.2 Conclusions

For the three developments presented in the previous section, we demonstrated by means of two case studies in an integral way that those developments may be employed effectively. The first case study concerned a shear wall analysis which combined the uncoupled formulation of the Coulomb friction model with the novel strategy for non-proportional loading. We showed that SLA was capable of detecting the experimentally observed failure mechanism, even though the model had the potential to fail in multiple ways. The inclusion of several material nonlinearities was straightforward and it did not complicate the numerical analysis. The second case study concerned the analysis of a scaled masonry façade which involved a smeared crack model and again the suggested approach for non-proportional loading. We have found that the obtained crack pattern was in agreement with experimental observations. However, the simulation had to be aborted prematurely since a proper crack closure algorithm is not yet included in the current SLA formulation, resulting in incorrect behavior of a crack where the load was reversed during the analysis. For both case studies, we have found the numerical analyses

with SLA to be robust. Also the developed non-proportional loading strategy performed well: at times we had to scale the last successful combination of the initial and reference load cases to continue the analysis, but after a number of cycles we were able to fully recover the initial loading.

In the remainder of this section, we will focus on our findings on a per development basis. Regarding the first development presented in Section 8.1, we showed that the improved band width ripple concept for setting up saw-tooth laws is virtually objective with respect to mesh refinement and/or damage increment refinement. In other words, the numerical analysis results are only slightly affected when meshes are refined and/or a larger number of saw-teeth is employed. More specifically, we have demonstrated for numerical analyses involving a smeared or discrete crack model that a mesh refinement results in a larger number of local jumps along the load–displacement curve. However, the size of these local jumps is hardly affected by a mesh refinement. On the other hand, the use of a more refined saw-tooth law does result in smaller local jumps. The latter type of refinement is particularly useful to better distinguish between structural snap-backs and snap-backs induced by the adopted saw-tooth law. We have also shown for smeared crack models that it is possible to employ saw-tooth laws with a snap-back at constitutive level. The results of the simulations involving such a saw-tooth law were in reasonable agreement with results of similar analyses that avoided the snap-back at constitutive level by employing a finer mesh. The analyses that combined the smeared crack concept with bond–slip behavior demonstrated that SLA does not require special techniques to capture structural snap-backs, which would be needed in case an incremental-iterative scheme was employed. Moreover, the analyses performed with SLA showed that the scaling procedure avoids bifurcations and no special measures were required to achieve strain localization.

With respect to the second development discussed in Section 8.1, we conclude that the two developed approximations of the Coulomb friction model may be effectively employed. Through a shear test we have shown that the uncoupled approximation is able to capture two important effects. In the first place, we demonstrated that the shear stress at the shear plane increases when a larger compressive stress is present, which is a key feature of any Coulomb friction law. With the same test, we also showed that cohesion softening can be taken into account and that after full cohesion softening the ultimate shear capacity is determined by dry friction only. We performed similar tests with the coupled approximation, which also showed a dependency of the ultimate shear stress on the applied normal stress. Moreover, we observed that with this model we were able to simulate the dilatancy effect. That is, plastic shear displacements were accompanied by plastic normal displacements, which resulted in additional compressive stresses in case these plastic normal displacements were restrained. In turn, the additional compressive stresses resulted in a larger shear capacity.

Regarding the third development, we showed that the novel strategy for non-proportional loading, which accounts for the load history, may be applied successfully. As mentioned earlier, at times no combination of the initial load case and



some scalar multiple of the reference load case exists without violating the material law at some integration point. In those cases, the initial loading is temporarily scaled as well. We have also found that after a number of damage increments the initial loading may be recovered. This kind of behavior could possibly be explained by our starting point of applying only one damage increment per analysis step. As argued by Eliáš et al. [19] and Eliáš [18] the application of a single damage increment may result in a stress redistribution that leads to immediate failure at other points. Thus multiple simultaneous damage increments may be required to re-establish equilibrium. With this in mind, the proposed strategy can be seen as a particular method to obtain a set of multiple damage increments after which static equilibrium is re-established.

### 8.3 Recommendations

Our first recommendation for future research is based on the analysis of the masonry shear wall in Section 7.1. We demonstrated that we were able to simulate the experimentally observed behavior effectively with SLA until the compressive stresses in the joints exceeded the compressive strength. Although the obtained results provided useful information, more insight could be gained if compressive failure would be considered. In order to continue the numerical analysis beyond the onset of crushing, a compressive failure criterion has to be added to the suggested tension–shear failure criterion. We expect that this can be done in a similar way as we did for tensile failure. In other words, for all integration points where crushing may occur, we need to consider additional constraints for the applied load multiplier corresponding to compressive failure. The subsequent maximization of the load multiplier does not require any modifications.

The case study of the scaled masonry façade provides the second recommendation for future research. We had to prematurely abort the numerical analysis due to the improper behavior of a closing crack that was reloaded in compression. The reason is that the current formulation of SLA does not include a proper crack closure algorithm. However, the inclusion of such an algorithm is particularly relevant for simulations that involve non-proportional loading, since cracks that have arisen due to the initial loading may be closed in a subsequent loading stage. A possible solution is to introduce a new type of event which corresponds to the transition from the tensile regime to the compressive regime and vice versa. In other words, we need to be able to adapt the stiffness at integration points where the load direction is reversed. This can be accomplished by first returning the stress–strain state to the origin, subsequently adapting the stiffness and only then continue loading in the other regime. In this way, a kink in the stress–strain relation at the origin can be accommodated. Consequently, contrary to what we have done so far, the local stiffness might increase again (e.g. when a crack closes and is reloaded in compression). Note that this approach requires a more elaborate memory: not only do we need to keep separate damage parameters for the tensile and compressive regimes,

but we also need to keep track of the previous stress at each integration point (tension or compression). A point of attention is that a continuously repeating pattern of opening and closing cracks might arise, which effectively brings the analysis to a halt.

Our final recommendation is related to the use of SLA and the extensions and improvements presented here in engineering practice. As explained during the review of SLA, per analysis step only one integration point is given a damage increment. Consequently, the number of analysis steps required to obtain a satisfactory result may grow large, depending on the total number of integration points that are damaged in the failure process and the number of saw-teeth per integration point. In engineering practice, the time available to carry out a simulation is in general limited, which makes SLA a less attractive alternative to the incremental-iterative scheme for performing nonlinear finite element analysis (NLFEA). On the other hand, since the SLA approach is inherently robust it might take less man hours to get the analysis up and running. One way to reduce the computer time required by SLA is to use (iterative) solvers that can reuse the previous solution. Keep in mind that per analysis step only a few entries of the system stiffness matrix are updated, which implies that the solution of the next linear analysis is probably closely related to the previous solution. Another way to reduce the required computer time is to allow for multiple damage increments in a single analysis step. The method developed by De Boer [7], which is available as the stiffness adaptation method [49] in the DIANA finite element package, is based on this concept. However, we would like to stress that this method is not damage-controlled and that the obtained results may be step size dependent.



# Appendix A Series development for Coulomb friction

This appendix examines under which conditions the secant approximation of the Coulomb friction model of Section 4.3 leads to a limited development of the normal relative displacement  $u_n$ . Since we have observed this behavior for the case of zero shear traction only, we will limit ourselves to this case.

Starting point of the discussion is a single line interface element which is subjected to a prescribed normal relative displacement in normal direction. In that case, we will obtain a non-zero normal traction and zero shear traction. The set of equations (4.22) shows the components of the secant stiffness matrix  $\mathbf{D}_{\text{sec}}^{(j+1)}$  for that particular case. It is repeated here for convenience

$$D_{11,\text{sec}}^{(j+1)} = \frac{k_{n,0}k_{t,0}(a_n - a_t \tan \psi) + t_{n,\text{crit}}^{(j)}(k_{t,0} + k_{n,0} \tan \phi \tan \psi)}{(u_{n,\text{crit}}^{(j)} + a_n)(k_{t,0} + k_{n,0} \tan \phi \tan \psi)} \quad (\text{A.1})$$

$$D_{12,\text{sec}}^{(j+1)} = 0 \quad (\text{A.2})$$

$$D_{21,\text{sec}}^{(j+1)} = \frac{k_{n,0}k_{t,0}u_{t,\text{crit}}^{(j)} \tan \phi (a_n - a_t \tan \psi) + t_{t,\text{crit}}^{(j)} a_t (k_{t,0} + k_{n,0} \tan \phi \tan \psi)}{(k_{n,0} \tan \phi \tan \psi + k_{t,0})(u_{n,\text{crit}}^{(j)} + a_n) a_t} \quad (\text{A.3})$$

$$D_{22,\text{sec}}^{(j+1)} = -\frac{k_{n,0}k_{t,0} \tan \phi (a_n - a_t \tan \psi)}{a_t (k_{n,0} \tan \phi \tan \psi + k_{t,0})} \quad (\text{A.4})$$

The traction vector  $\mathbf{t}^{(j+1)}$  of cycle  $j + 1$  is related to the corresponding relative displacement vector  $\mathbf{u}^{(j+1)}$  through

$$\begin{pmatrix} t_n^{(j+1)} \\ t_t^{(j+1)} \end{pmatrix} = \begin{bmatrix} D_{11,\text{sec}}^{(j+1)} & D_{12,\text{sec}}^{(j+1)} \\ D_{21,\text{sec}}^{(j+1)} & D_{22,\text{sec}}^{(j+1)} \end{bmatrix} \begin{pmatrix} u_n^{(j+1)} \\ u_t^{(j+1)} \end{pmatrix} \quad (\text{A.5})$$

with the components of the secant stiffness matrix from Equation (A.4). Since we impose zero shear displacement, i.e.  $u_t^{(j+1)} = 0$ , the normal traction  $t_n^{(j+1)}$  depends on the normal relative displacement only through the stiffness component  $D_{11,\text{sec}}^{(j+1)}$ . If we assume no cohesion softening (i.e. the failure contour does not change throughout the analysis) the normal traction  $t_n^{(j+1)}$  will remain constant at

$t_n$ . Now when we update the secant constitutive matrix as per Equation (A.4), we can directly compute the relative normal displacement  $u_n^{(j+1)}$

$$u_n^{(j+1)} = \frac{t_n}{D_{11,\text{sec}}^{j+1}} \quad (\text{A.6})$$

Now if we introduce a parameter  $r$

$$r = \frac{t_n(k_{t,0} + k_{n,0} \tan \phi \tan \psi)}{k_{n,0}k_{t,0}(a_n - a_t \tan \psi) + t_n(k_{t,0} + k_{n,0} \tan \phi \tan \psi)} \quad (\text{A.7})$$

we can rewrite Equation (A.6) as a recursive formula

$$u_n^{(j+1)} = r(u_n^{(j)} + a_n) \quad (\text{A.8})$$

Note that the expression for  $r$  only contains quantities that remain constant across cycles. We can expand the recursive formula above as follows

$$\begin{aligned} u_n^{(j+1)} &= r u_n^{(j)} + a_n r \\ &= r^2 u_n^{(j-1)} + a_n (r + r^2) \\ &= r^3 u_n^{(j-2)} + a_n (r + r^2 + r^3) \\ &= r^j u_n^{(1)} + a_n (r + r^2 + r^3 + \dots + r^j) \\ &= r^j u_n^{(1)} + a_n \sum_{k=1}^j r^k \end{aligned}$$

From elementary calculus we know that geometric series are of the form

$$a_n (1 + r + r^2 + \dots + r^k + \dots) = a_n \sum_{k=0}^{\infty} r^k \quad (\text{A.9})$$

If  $|r| < 1$  then it can be shown that the series converges to a finite value

$$a_n \sum_{k=0}^{\infty} r^k = \frac{a_n}{1 - r} \quad (\text{A.10})$$

This implies that the sum in the expanded recursive formula converges to

$$a_n \sum_{k=1}^j r^k = \frac{a_n r}{1 - r} \quad (\text{A.11})$$

if  $j$  approaches infinity and  $|r| < 1$ .

However, this would yield an undesired result, since it means that opening of the interface is limited. Therefore, we recommend to select  $a_n$  and  $a_t$  such that  $a_n/a_t \leq \tan \psi$  which results in  $|r| \geq 1$ .

## References

- [1] W. Anemaat and B. de Graaff. Tackling shear failure problems (in Dutch). *Cement*, 4:4–7, 2012.
- [2] Z. P. Bažant and L. Cedolin. Blunt crack band propagation in finite element analysis. *Journal of the Engineering Mechanics Division*, 105(2):297–315, 1979.
- [3] Z. P. Bažant and B. H. Oh. Crack band theory for fracture of concrete. *Materials and Structures*, 16:155–177, 1983.
- [4] B. Belletti, M. J. DeJong, A. V. van de Graaf, M. A. N. Hendriks, and J. G. Rots. “Sequentially linear analysis” for the response prediction by pushover analysis of URM buildings subjected to seismic loads. In *Proceedings of ANIDIS2009*, 2009.
- [5] W. J. Beranek and G. J. Hobbelman. 2D and 3D-modelling of concrete as an assemblage of spheres: revaluation of the failure criterion. In F. H. Wittmann, editor, *Fracture mechanics of concrete structures. Proc. FRAMCOS-2*, volume 2, pages 965–978. Aedificatio, 1995.
- [6] A. J. Bigaj. *Structural dependence of rotation capacity of plastic hinges in RC beams and slabs*. PhD thesis, Delft University of Technology, 1999.
- [7] A. de Boer. *Design strategy structural concrete in 3D focusing on uniform force results and sequential analysis*. PhD thesis, Delft University of Technology, 2010.
- [8] J. E. Bolander, Jr, G. S. Hong, and K. Yoshitake. Structural concrete analysis using rigid-body-spring networks. *Computer-Aided Civil and Infrastructure Engineering*, 15(2):120–133, 2000.
- [9] R. de Borst. *Non-linear analysis of frictional materials*. PhD thesis, Delft University of Technology, 1986.
- [10] M. Cervera, L. Pelà, R. Clemente, and P. Roca. A crack-tracking technique for localized damage in quasi-brittle materials. *Engineering Fracture Mechanics*, 77(13):2431–2450, 2010.
- [11] H. A. W. Cornelissen, D. A. Hordijk, and H. W. Reinhardt. Experimental determination of crack softening characteristics of normalweight and lightweight concrete. *Heron*, 31(2):45–56, 1986.

- [12] M. A. Crisfield. Accelerated solution techniques and concrete cracking. *Computer Methods in Applied Mechanics and Engineering*, 33(1–3):585–607, 1982.
- [13] M. A. Crisfield. *Nonlinear finite element analysis of solids and structures. Volume 1: Essentials*. Wiley, New York, 1991.
- [14] CUR. Structural masonry: an experimental/numerical basis for practical design rules (in Dutch). Technical Report 171, CUR, Gouda, The Netherlands, 1994.
- [15] M. J. DeJong, M. A. N. Hendriks, and J. G. Rots. Shear retention and mesh alignment during fracture using sequentially linear analysis. In *12th International Conference on Fracture, ICF'09*, Ottawa, Canada, 2009.
- [16] M. J. DeJong, M. A. N. Hendriks, and J. G. Rots. Sequentially linear analysis of fracture under non-proportional loading. *Engineering Fracture Mechanics*, 75(18):5042–5056, 2008.
- [17] K. Dörr. *Ein Beitrag zur Berechnung von Stahlbetonscheiben unter besonderer Berücksichtigung des Verbundverhaltens*. PhD thesis, University of Darmstadt, 1980.
- [18] J. Eliáš. Generalization of load-unload and force-release sequentially linear methods. *International Journal of Damage Mechanics*, 24(2):279–293, 2015.
- [19] J. Eliáš, P. Frantík, and M. Vořechovský. Improved sequentially linear solution procedure. *Engineering Fracture Mechanics*, 77(12):2263–2276, 2010.
- [20] S. W. H. Ensink. Simulation of steel–concrete bond–slip with sequentially linear analysis using interface elements. Master’s thesis, Delft University of Technology, 2010.
- [21] S. W. H. Ensink, A. V. van de Graaf, A. T. Slobbe, M. A. N. Hendriks, and J. G. Rots. Modeling of bond behaviour by means of sequentially linear analysis and concrete-to-steel interface elements. In *Proceedings of the Fourth Bond In Concrete Conference*, 2012.
- [22] G. Giardina, M. A. N. Hendriks, and J. G. Rots. Finite element prediction of expected damage for masonry façades loaded in shear. Technical report, CRUX Engineering BV, 2010.
- [23] G. Giardina, A. Marini, M. A. N. Hendriks, J. G. Rots, F. Rizzardini, and E. Giuriani. Experimental analysis of a masonry façade subject to tunnelling-induced settlement. *Engineering Structures*, 45:421–434, 2012.
- [24] G. Giardina, A. V. van de Graaf, M. A. N. Hendriks, J. G. Rots, and A. Marini. Numerical analysis of a masonry façade subject to tunnelling-induced settlements. *Engineering Structures*, 54:234–247, 2013.

- [25] F. B. J. Gijsbers and A. A. Hehemann. Some tensile tests on reinforced concrete. Technical Report BI-77-61, TNO-IBBC, Rijswijk, 1977.
- [26] A. V. van de Graaf. Sequentially linear analysis as an alternative to nonlinear analysis applied to a reinforced glass beam. In *Proceedings of 7th fib PhD symposium*, pages 63–71, Stuttgart, Germany, 2008.
- [27] A. V. van de Graaf, M. A. N. Hendriks, and J. G. Rots. A discrete cracking model for sequentially linear analysis. In N. Bićanić, R. de Borst, H. Mang, and G. Meschke, editors, *Computational Modelling of Concrete Structures*, pages 409–418, Rohrmoos/Schladming, Austria, 2010. CRC Press/Balkema. EURO-C 2010.
- [28] R. Graça-e-Costa, J. Alfaiate, D. Dias-da-Costa, and E. Julio. Numerical modelling of a high-strength prestressed concrete beam using a strong discontinuity approach. In R. F. H. Barros, C. Pina, and C. Ferreira, editors, *International conference on recent advances in nonlinear models—structural concrete applications—CoRAN 2011*, pages 453–469, Coimbra, Portugal, 2011.
- [29] R. Graça-e-Costa, J. Alfaiate, D. Dias-da-Costa, and L. J. Sluys. A non-iterative approach for the modelling of quasi-brittle materials. In *International Conference on Computational Modeling of Fracture and Failure of Materials and Structures (CFRAC)*, Barcelona, Spain, June 2011.
- [30] R. Graça-e-Costa, J. Alfaiate, D. Dias-da-Costa, P. Neto, and L. J. Sluys. Generalisation of non-iterative methods for the modelling of structures under non-proportional loading. *International Journal of Fracture*, 182:21–38, 2013.
- [31] A. K. de Groot, G. M. A. Kusters, and T. Monnier. Numerical modelling of bond–slip behaviour. *Heron*, 26(1B), 1981.
- [32] M. A. Gutiérrez. Energy release control for numerical simulations of failure in quasi-brittle solids. *Communications in Numerical Methods in Engineering*, 20(1):19–29, 2004.
- [33] S. Harrison. A biaxial failure criterion for masonry. Technical report, University of Cambridge, 2010.
- [34] M. A. N. Hendriks and J. G. Rots. Sequentially linear versus nonlinear analysis of RC structures. *Engineering Computations*, 30(6):792–801, 2013.
- [35] H. J. Herrmann, A. Hansen, and S. Roux. Fracture of disordered, elastic lattices in two dimensions. *Physical Review B*, 39(1):637–648, 1989.
- [36] A. Hillerborg. Numerical methods to simulate softening and fracture of concrete. In G. C. Sih and A. DiTommaso, editors, *Fracture mechanics of concrete: Structural application and numerical calculation*, volume 4 of *Engineering Application of Fracture Mechanics*, pages 141–170. Springer Netherlands, 1984.



- [37] D. A. Hordijk. *Local approach to fatigue of concrete*. PhD thesis, Delft University of Technology, 1991.
- [38] A. R. Ingraffea and V. Saouma. Numerical modeling of discrete crack propagation in reinforced and plain concrete. In G. C. Sih and A. DiTommaso, editors, *Fracture mechanics of concrete: Structural application and numerical calculation*, volume 4 of *Engineering Application of Fracture Mechanics*, pages 171–225. Springer Netherlands, 1984.
- [39] S. Invernizzi, D. Trovato, M. A. N. Hendriks, and A. V. van de Graaf. Sequentially linear modelling of local snap-back in extremely brittle structures. *Engineering Structures*, 33(5):1617–1625, 2011.
- [40] S. H. Kwon, Z. Zhao, and S. P. Shah. Effect of specimen size on fracture energy and softening curve of concrete: Part II. Inverse analysis and softening curve. *Cement and Concrete Research*, 38(8-9):1061–1069, 2008.
- [41] E. O. L. Lantsoght, C. van der Veen, and J. C. Walraven. Shear in one-way slabs under concentrated load close to support. *ACI Structural Journal*, 110(2): 275–284, 2013.
- [42] D. J. Lekkerkerker. Sequentially linear analysis of pre-stressed concrete beams. Master’s thesis, Delft University of Technology, 2011.
- [43] G. Lilliu. *3D analysis of fracture processes in concrete*. PhD thesis, Delft University of Technology, 2007.
- [44] P. B. Lourenço. Analysis of masonry structures with interface elements. Technical report, Delft University of Technology and TNO Building and Construction Research, June 1994. TU-DELFT report no. 03-21-22-0-01 and TNO-BOUW report no. 94-NM-R0762.
- [45] P. B. Lourenço. *Computational strategies for masonry structures*. PhD thesis, Delft University of Technology, 1996.
- [46] C. Louter, A. van de Graaf, and J. Rots. Modeling the structural response of reinforced glass beams using an SLA scheme. In F. Bos, P. C. Louter, and F. Veer, editors, *Challenging Glass 2 – Conference on Architectural and Structural Applications of Glass*, pages 427–438, Delft, The Netherlands, 2010.
- [47] P. C. Louter. *Fragile yet Ductile: Structural Aspects of Reinforced Glass Beams*. PhD thesis, Delft University of Technology, 2011.
- [48] K. Maekawa, A. Pimanmas, and H. Okamura. *Nonlinear mechanics of reinforced concrete*. CRC Press, 2003.
- [49] J. Manie. *DIANA User’s Manual – Application Modules*. TNO DIANA BV, 9.4.4 edition, December 2011.

- [50] J. Manie and W. P. Kikstra. *DIANA User's Manual – Element Library*. TNO DIANA BV, 9.3 edition, April 2008.
- [51] J. Manie and W. P. Kikstra. *DIANA User's Manual – Material Library*. TNO DIANA BV, 9.3 edition, April 2008.
- [52] D. Ngo and A. C. Scordelis. Finite element analysis of reinforced concrete beams. *Journal of the American Concrete Institute*, 64(3):152–163, 1967.
- [53] R. van der Pluijm. Shear behaviour of bed joints. In D. P. Abrams, editor, *Proceedings of the Sixth North American Masonry Conference*, pages 125–136, Philadelphia, 1993.
- [54] T. M. J. Raijmakers and A. T. Vermeltfoort. Deformation controlled tests in masonry shear walls. Technical report, TNO-Bouw, Delft, The Netherlands, 1992. Report B-92-1156 (in Dutch).
- [55] E. Riks. An incremental approach to the solution of snapping and buckling problems. *International Journal of Solids and Structures*, 15(7):529–551, 1979.
- [56] J. G. Rots. *Computational modeling of concrete fracture*. PhD thesis, Delft University of Technology, 1988.
- [57] J. G. Rots. Sequentially linear continuum model for concrete fracture. In R. de Borst, J. Mazars, G. Pijaudier-Cabot, and J. G. M. van Mier, editors, *Fourth International Conference on Fracture Mechanics of Concrete and Concrete Structures*, volume 2, pages 831–839. Balkema, A. A., 2001.
- [58] J. G. Rots and S. Invernizzi. Regularized sequentially linear saw-tooth softening model. *International Journal for Numerical and Analytical Methods in Geomechanics*, 28(7–8):821–856, 2004.
- [59] J. G. Rots, B. Belletti, and S. Invernizzi. On the shape of the saw-tooth softening curves for sequentially linear analysis. In G. Meschke, R. de Borst, H. Mang, and N. Bićanić, editors, *Computational Modelling of Concrete Structures*, pages 431–442. Taylor and Francis Group, London, 2006.
- [60] J. G. Rots, S. Invernizzi, B. Belletti, and M. A. N. Hendriks. Circumventing bifurcations in structural softening. In M. Hendriks and S. Billington, editors, *Computational Modeling on Concrete, Masonry and Fiber-reinforced Composites*, pages 49–52, Delft, The Netherlands, June 2009.
- [61] J. G. Rots, B. Belletti, and S. Invernizzi. Robust modeling of RC structures with an “event-by-event” strategy. *Engineering Fracture Mechanics*, 75(3–4):590–614, 2008.
- [62] A. Salam Al-Sabah and D. F. Laefer. Use of negative stiffness in failure analysis of concrete beams. *Engineering Structures*, 126:187–199, 2016.

- [63] R. Sarkhosh, J. A. den Uijl, B. C. R., and J. C. Walraven. Shear capacity of concrete beams without shear reinforcement under sustained loads. Technical report, Delft University of Technology, December 2010. Report 25.5.10-17.
- [64] R. Sarkhosh. Shear capacity of concrete beams under sustained loading. In H. S. Müller, M. Haist, and F. Acosta, editors, *Proceedings of 9th fib international PhD symposium in civil engineering*, 2012.
- [65] E. Schlangen and J. G. M. van Mier. Experimental and numerical analysis of micromechanics of fracture of cement-based composites. *Cement and Concrete Composites*, 14(2):105–118, 1992.
- [66] B. Shieh-Beygi and S. Pietruszczak. Numerical analysis of structural masonry: mesoscale approach. *Computers and Structures*, 86(21–22):1958–1973, 2008.
- [67] A. T. Slobbe. Sequentially linear analysis of shear critical reinforced concrete beams. Master’s thesis, Delft University of Technology, 2010.
- [68] A. T. Slobbe, M. A. N. Hendriks, and J. G. Rots. Sequentially linear analysis of shear critical reinforced concrete beams without shear reinforcement. *Finite Elements in Analysis and Design*, 50:108–124, 2012.
- [69] A. T. Slobbe, M. A. N. Hendriks, and J. G. Rots. Smoothing the propagation of smeared cracks. *Engineering Fracture Mechanics*, 132:147–168, 2014.
- [70] A. Slobbe. *Propagation and band width of smeared cracks*. PhD thesis, Delft University of Technology, 2015.
- [71] A. T. Vermeltfoort and T. M. J. Raijmakers. Deformation controlled tests in masonry shear walls, part 2. Technical report, Eindhoven University of Technology, Eindhoven, the Netherlands, 1993. Report TUE/BKO/93.08 (in Dutch).
- [72] L. O. Voormeeren. Extension and verification of sequentially linear analysis to solid elements. Master’s thesis, Delft University of Technology, 2011.
- [73] J. Walraven. *Shear and punching shear in RC and FRC elements*, chapter 8, pages 129–138. Number 57 in fib bulletin. fib, 2010.
- [74] Z. Zhao, S. H. Kwon, and S. P. Shah. Effect of specimen size on fracture energy and softening curve of concrete: Part I. Experiments and fracture energy. *Cement and Concrete Research*, 38(8-9):1049–1060, 2008.

# Acknowledgements

First of all, I would like to thank my promotors, Jan Rots and Max Hendriks, for introducing me to the academic world and for giving me the opportunity to contribute to their research programme. It has been a true privilege and pleasure to work with them. Without their valuable comments and the good discussions we have had I would not nearly have achieved the result that I present here. And although it has taken me considerable time and effort to complete the thesis, they have never stopped supporting me. I am grateful for their motivating words in difficult times and for the freedom and confidence they have given me.

The financial support by Delft Cluster and the Centre for Underground Construction (COB) is gratefully acknowledged (a part of this work has been carried out for COB committee F532). I would also like to thank DIANA FEA BV (formerly TNO DIANA BV) for providing a copy of the source code of DIANA 9.2 to write a pilot implementation of the sequentially linear analysis (SLA) approach. In that way, I was able to re-use the infrastructure already available in the NONLIN application module.

I am indebted to Giorgia Giardina, Arthur Slobbe and Rita Esposito, who have shared this PhD adventure with me. Not just for working together, but also for the great times we have had during Italian dinners and over drinks at Kobus Kuch's. Furthermore, I would like to thank Lars Voormeeren, Sebastiaan Ensink and Dick Lekkerkerker for their contribution to the development of SLA.

And last but not least, I would like to express my deepest gratitude to my family and friends, in particular my girlfriend Hellen, for her loving support and patience, and my beautiful young daughter Lynn, for showing me what really matters in life.

Anne van de Graaf,  
December 2016



# Curriculum Vitae

June 28, 1981	Born in Spijkenisse, The Netherlands, as Anne Vincent van de Graaf
Sep. 1994 – June 2000	Atheneum, Angelus Merula, Spijkenisse
Sep. 2000 – Sep. 2004	Bachelor of Science in Civil Engineering, Delft University of Technology
Sep. 2003 – Dec. 2006	Master of Science in Civil Engineering, Delft University of Technology
Jan. 2007 – Nov. 2007	Structural engineer at Witteveen+Bos
Dec. 2007 – Sep. 2012	PhD candidate in the Structural Mechanics group at the Faculty of Civil Engineering and Geosciences, Delft University of Technology
Oct. 2012 – present	Software development engineer at DIANA FEA BV (formerly TNO DIANA BV)



## List of publications

- A. V. van de Graaf, M. A. N. Hendriks, and J. G. Rots. Coulomb friction with non-proportional loading for sequentially linear analysis. To be submitted for publication in *Engineering Structures*.
- A. V. van de Graaf, M. A. N. Hendriks, and J. G. Rots. A discrete cracking model for sequentially linear analysis. In Nenad Bićanić, R. de Borst, Herbert Mang, and Günther Meschke, editors, *Computational Modelling of Concrete Structures*, pages 409–418, Rohrmoos/Schladming, Austria, 2010. CRC Press/Balkema. EURO-C 2010.
- A. V. van de Graaf, M. A. N. Hendriks, and J. G. Rots. Sequentially linear analysis for modelling tunnelling-induced surface structure damage. In Günther Meschke, Gernot Beer, Josef Eberhardsteiner, Dietrich Hartmann, and Markus Thewes, editors, *2nd International Conference on computational methods in tunnelling, EURO:TUN 2009*, pages 977–980, Freiburg, Germany, 2009. Aedificatio Publishers.
- A. V. van de Graaf, M. A. N. Hendriks, and J. G. Rots. Sequentially linear analysis of masonry structures under non-proportional loading. In M. A. N. Hendriks and S. L. Billington, editors, *Computational Modeling Workshop on Concrete, Masonry and Fiber-reinforced Composites*, pages 23–26, Delft, The Netherlands, 2009.
- A. V. van de Graaf. Sequentially linear analysis as an alternative to nonlinear analysis applied to a reinforced glass beam. In *Proceedings of 7th fib PhD symposium*, pages 63–71, Stuttgart, Germany, 2008.